Magneto-Optical Trapping of Strontium for use as a Mobile Frequency Reference

by

Björn Ole Kock

A thesis submitted to
The University of Birmingham
for the degree of
DOCTOR OF PHILOSOPHY

Ultracold Atoms Group
School of Physics and Astronomy
College of Engineering and Physical Sciences
The University of Birmingham

April 2013

UNIVERSITY OF BIRMINGHAM

Abstract

College of Engineering and Physical Sciences
School of Physics and Astronomy

Doctor of Philosophy

by Björn Ole Kock

Atomic Caesium clocks have made an astonishing development in the past few decades, with them gaining an order of magnitude in precision every decade. A new generation of atomic optical clocks is now emerging, which is moving to the forefront of timekeeping. By going from microwave to optical frequencies these clocks are now reaching fractional uncertainty levels in the 10^{-18} range [1], opening a whole new range of exciting applications.

This thesis presents the design and implementation of an experiment for laser cooling of strontium atoms, focusing on the mobility of the setup, opening a range of new applications as a mobile clock. The experimental apparatus applies a range of new techniques for strontium, such as the use of a two dimensional magneto-optical trap for pre cooling atoms, allowing for a compact and transportable system. A mobile laser system for laser cooling strontium atoms was realised. This includes a frequency doubling system for the main cooling transition. The constructed monolithic frequency doubling cavity has generated 300 mW of blue light and proven to be a stable setup suitable for a mobile system. The 3D-MOT was able to capture $4 \cdot 10^5$ atoms with a long lifetime of 5.5 s, with further improvements for a significant increase in atom number currently being implemented.

Acknowledgements

It's been a great four years here in Birmingham in the Ultracold Atoms group. It was hard work, but been sweetened by the great group we are.

At first I want to thank Prof. Kai Bongs for bringing me to Birmingham. Kai was a great support during my PhD with the countless discussion with his great ideas and always finding time in his busy schedule. When he had the time to come to the lab, I was consistently impressed by how he always found the one knob to turn to get the experiment going again. Most importantly I want to acknowledge my lab partner Steve, who has been a great help in the lab, a constant source of up to date information on University politics and endured my taste of music in the lab. I also want to thank Yeshpal for being a good support in numerous discussions. As well as Wei who has been a great help on the final stretch and I hope I'm leaving you a system to further do great research.

A big thanks goes to the rest of the office: Nadine, Mathis, Mike, Mat, Marisa and our latest addition Charlotte. Who have made my time here that much more enjoyable. Nadine, we've been working together now for ages. It's been and will be an amazing time in and out of the office with you. The next PhD should definitely be in the Mediterranean with lots of sun. Mathis, can you believe that we started studying Physics together almost ten years ago. It's been a great time in the office and as a housemate. Mike, since you are gone the pranks have almost halted. We've had a lot of fun. May your pranks continue in Brazil. Mat, the one constant when it comes to social gatherings. Marisa, the most happy person I know, but yet always all business. May the Jitsu virus I infected you with spread. A special thanks goes to Jochen for his vast expertise in electronics and him always being the one to ask, when it comes to the tricky questions of why things don't work how they should. And also a great thanks everyone else in the Quantum Matter group.

I also want to thank my summer students Harry, who keeps coming back, and Jon, who we seem to not have scared away, since you're now doing a PhD in the group. I also want to acknowledge our fourth year students, Harry, still keeps coming back, Johnny, Josh and Graham. Of course you all came in the last year. I've enjoyed working with you. I also wish to acknowledge Alexander Franzen for supplying the useful optics graphics library. For the great work they provided I wish to thank the workshop team and especially Steve Brooks.

My final and most important thanks goes to my mum and dad, who have been a great support since, well since my beginning.

Contents

List of Figures

List of Tables

Introduction

Atomic Caesium clocks have made an astonishing development in past decades, with them gaining an order of magnitude every decade and having now reached a fractional uncertainty of 10^{-16} [3]. A new generation of atomic optical clocks is now emerging, which are now moving to the forefront of timekeeping. By going from microwave to optical frequencies these clocks are now reaching fractional uncertainty levels in the 10^{-18} range [1, 4]. In this thesis I will present the design and ongoing realization of the first transportable optical clock with neutral strontium atoms using a two dimensional magneto-optical trap. The transportability of an atomic clock opens a range of many new exciting applications. With the use of the gravitational red-shift atomic clocks can be used to measure the absolute gravitational potential, allowing for the synchronisation of national height systems. This setup can also be seen as a step towards an optical atomic clock in space. Using the advantages of the stable space environment, an atomic optical clock in space could be used as a master clock to distribute a stable timing signal to clocks on earth and in space. Furthermore the generation of Global Navigation Satellite Systems (GNSS) would benefit from the decreased uncertainty. Strontium is an ideal candidate for an atomic optical clock, as it offers an easily accessible very narrow optical transition, which is only weakly influenced by external fields. Its level structure offers an easily accessible broad transition for efficient laser cooling and trapping and a narrow transition for reaching low temperatures. The low complexity of the required lasers is especially desirable for a portable setup. The only major concern is the relatively large sensitivity to black body radiation, which is currently being mapped to be compensated [5]. In order to move to a mobile experiment I will present the solutions I have developed to trap strontium atoms. One of the main focuses of this experiment are the laser systems I have developed and tested to meet the requirements of a mobile setup to allow for efficient cooling and trapping of strontium. For this I have constructed and characterised a robust frequency doubling cavity giving up to 300 mW of the required blue cooling light. I will show the successful first trapping of strontium in a two dimensional magneto-optical trap (MOT) as a source for providing pre-cooled atoms for trapping in a three dimensional MOT.

This thesis is divided into six further chapters, which are organized as following:

Chapter 1 gives a historical perspective on the development of atomic clocks and gives an overview of atomic optical clocks and their potential future applications.

Chapter 2 will introduce the concept of laser cooling and magneto-optical trapping of neutral atoms and show the simulations carried out to find the optimum parameters for the 2D-MOT and give an estimation of the expected flux of atoms.

Chapter 3 presents the mobile laser systems constructed for this experiment, highlighting the construction and characterization of a robust frequency doubling cavity. Additionally an overview of investigated alternative blue sources suitable for a mobile experiment will be presented.

Chapter 4 is dedicated to the experimental setup, detailing the construction of the vacuum apparatus and all its components as well as showing the design and programming of the experimental control system.

Chapter 5 will present the results achieved in successfully trapping neutral strontium atoms in a 3D-MOT, which is loaded with pre-cooled atoms from a 2D-MOT.

Chapter 6 will give an outlook of the development of this experiment in the near future.

Chapter 1

Introduction to Atomic Clocks

The accurate measurement of time has always played a fundamental role in mankind's life. This chapter will give an introduction into the historical development of timekeeping and give an overview of the development and current state of atomic clocks. Also the potential applications of the next generation of atomic clocks will be highlighted.

1.1 Historical Perspective

In mankind's life the measurement of time has played an important role for many centuries. Societies agricultural endeavours, one of the main sources of food, require the knowledge of the time of the year, as crops need to be planted in accordance with the seasons. The time provided by nature is the rotation of earth and celestial bodies which were used for timekeeping for many decades. This allowed for the synchronization of activities on the timescale of months and days. However these natural timescales can not be used to further divide time into smaller units, which were being demanded by progressing more complex societies. Such things like the coordination of transport and navigation required widely available timing below the scale nature provided. For this, devices with periodic events occurring more frequently were required, which subsequently led to the development of man made clocks.

The first man made clocks were simple devices like water or sand clocks which allowed one to further divide the day. Over time the complexity of these clocks increased leading to designs like the verge-escapement, the first mechanical clock to control its rate by advancing a gear train at regular intervals. In the 14th century accuracies of 15 minutes per day were achievable. The invention of the pendulum clock by Huygens played an important role in the improvement of timing precision. The first versions of this device only lost a minute in one day, with the best pendulum clocks reaching accuracies of less than one second per 100 days by the end of the 19th century.

The development of small mechanical clocks, as they are still used nowadays, was mainly driven by navigational needs for ships in the 18th century. Pendulum clocks were not suitable for the sea, especially in rough weather, but accurate timekeeping was crucial for navigation to determine longitude by means of celestial navigation. A different approach was required and the invention of the marine chronometer by John Harrison in 1761 was able to satisfy the required accuracy of 1 second per day. Nowadays most mechanical clocks still use the same principles of this revolutionary technology.

The rapid increase in accuracy of clocks, as we are still seeing it nowadays, began in the 20th century with the development of quartz oscillators. Electro-mechanical resonances in these crystals had a significantly smaller oscillation period, allowing for timing on much shorter timescales. Well designed quartz oscillators only show a change in period corresponding to a loss of one second in up to 30 years.

The development of man made clocks has seen great improvements from the first water clocks over the pendulum clocks to the quartz oscillators. But yet one fundamental limit remaining with all these clocks is that they do not offer an absolute time reference. They themselves need to be synchronised periodically with an absolute reference.

1.2 Atomic Clocks

The development of quantum mechanics has led to a new understanding of atomic structure, enabling the use of atomic transitions to build more accurate and stable clocks than mechanical clocks can ever be. The structure of the atom allows for transitions between energy levels by the emission and absorption of electromagnetic radiation. The atomic energy levels precisely determine the frequency of the emitted light.

The frequency emitted by an atom on a specific transition will be exactly the same for every atom of this species, when observed in the same environment, allowing an absolute measurement of time. The difference in timing of two clocks now only depends on their ability to read out the atomic transition and take into account environmental effects, such as gravity.

The first demonstration of an atomic transition as a frequency reference was the use of the inversion transition in ammonia in 1949 [6] with the first demonstration of a caesium atomic clock soon to follow at the UK National Physical Laboratory (NPL) [7]. The achieved accuracies have lead to a redefinition of the second within the International System of Units (SI) as "the duration of 9192,631,770 periods of the radiation corresponding to the transition between the two hyperfine levels of the ground state of the caesium-133 atom" [8]. Up to today this definition still holds.

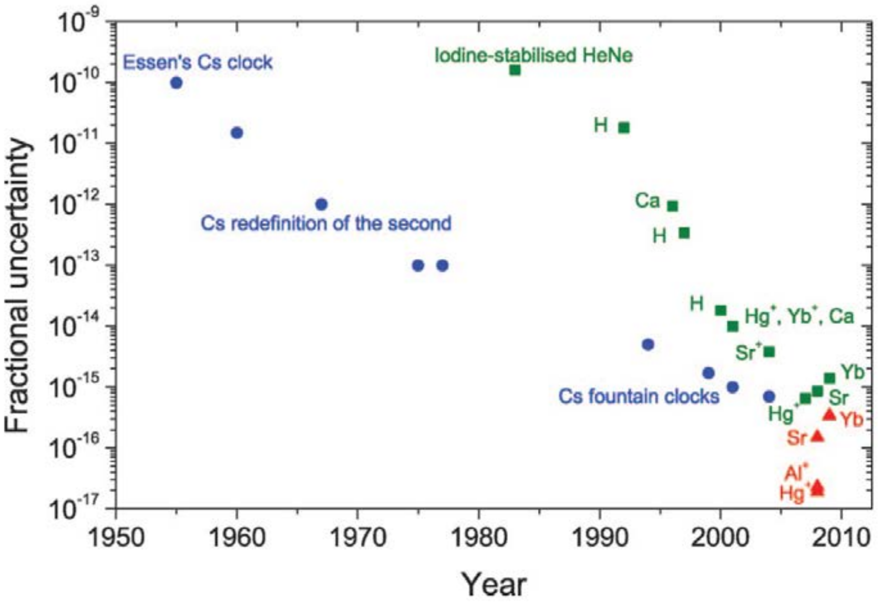

FIGURE 1.1: Development of atomic clocks since 1955. In blue the development of Cs clocks. In green the development of optical clocks. In red most recent developments of optical clocks with estimated uncertainties. Figure reproduced from [9].

Caesium clocks have made an astonishing development in the last half century. Roughly an order of magnitude in uncertainty was won per decade, where the uncertainty of a clock is defined as the drift of the clock from an ideal clock. The best caesium fountain clocks are now reaching uncertainties in the lower 10^{-16} level, meaning a fractional uncertainty, as is illustrated in figure 1.1.

1.2.1 Atomic Optical Clocks

Although the development of the caesium atomic clocks has been astonishing in the last decades, they are now reaching limitations, where the required effort for a much further increase in uncertainty would stand in no contrast to the gain. Currently the main contributors for the uncertainty of caesium clocks are collisional shifts and the microwave power dependence [10]. The next possible step would be to further increase the frequency by going to optical transitions. Such optical clocks have been around since 1980, but to acquire an electronically usable signal, complicated frequency chains were required.

Such a chain would convert the optical frequency of several hundred terahertz to an electronically accessible microwave signal in several complicated frequency conversion steps [11, 12]. But these chains were too complex and unreliable for the clock to truly benefit from the increase in frequency.

The development of the octave spanning frequency comb enabled the direct readout of the optical frequencies. This invention revolutionized the development of optical clocks by greatly reducing their complexity. A frequency comb consists of a mode locked laser delivering ultra short ($\sim 10^{-15}$s) pulses which are separated in time by $\tau = 1/f_{rep}$, defined by the pulse repetition rate f_{rep}. In the frequency domain the output consists of evenly spaced discrete frequencies peaks, which look like a comb, separated by f_{rep}. With the use of a non-linear fibre, these peaks are spread to the entire visible light domain, allowing the exact determination of the frequency of each comb mode by self referencing. The optical frequency of an interrogation laser is converted to the microwave domain by beating it with a nearby comb mode of known frequency. Optical frequency combs can be seen as an optical ”clockwork” with current measurement inaccuracies in the $\sim 10^{-19}$ range [13]. The importance of the frequency comb was valued by the Nobel Prize being awarded to its inventors in 2005.

An atomic optical clock consists of two main parts: One is the interrogation or clock laser and the other one the atomic reference as is shown in figure 1.2. The clock laser will probe the atomic reference and is held on resonance by the control electronics. To prevent drifts of the clock laser in between measurements of the atomic transition it needs to have very low drifts on timescales of a second. To achieve this it is locked to an ultra high finesse cavity, which is thermally very well stabilized to achieve the required stability. For a high accuracy and stability of the clock external effects on the atomic transition, such as Doppler broadening or collisional shifts, have to be minimized.

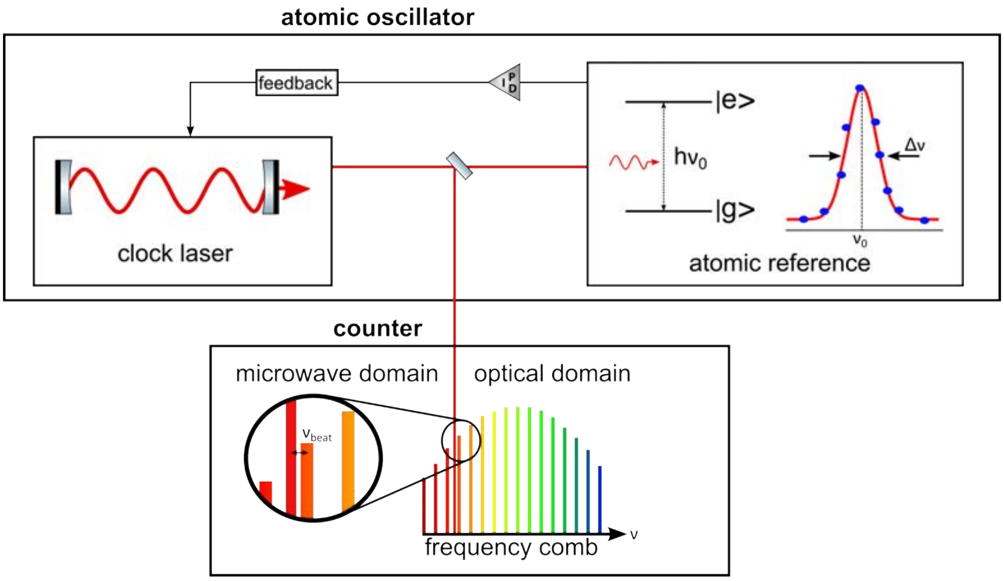

FIGURE 1.2: Schematic overview of the setup of an atomic optical clock. Top half: The cavity pre-stabilised clock laser is stabilised to the atomic reference transition by an electronic feedback loop, inheriting it's accuracy. The atomic reference transition is a very narrow linewidth transition to allow for a very precise measurement. Bottom half: The frequency of the clock laser is converted to an electronically countable microwave frequency by beating it with a frequency comb.

The clock laser itself requires a high degree of stability to fully benefit from the narrow linewidth of the atomic transition [14, 15].

With the advances in laser cooling and laser technologies and with the combination of frequency combs optical clocks have passed the caesium clocks' stability in recent years and are now moving to the forefront of the frequency standards field (see figure 1.1). It is now only a matter of time until the redefinition of the SI second by an optical standard.

1.2.2 Principle of a Neutral Atomic Optical Lattice Clock

Two types of optical clocks are currently in a head to head race. One approach uses ions as a reference, drawing on the advantages of tight confinement in ion traps, which eliminates Doppler effects, and having long readout times. But such clocks are currently limited by the probing of a single ion, as it is very difficult to capture several ions without them disturbing each other. The other promising approach to such an optical standard uses neutral atoms tightly confined in an optical lattice. This gives optical lattice clocks the advantages of the low Doppler effects of ion clocks combined with high atom numbers, but potentially at the cost of larger influence from the environment [16].

To understand the advantages of confining the atoms in an optical lattice let us look at the Doppler broadened linewidth of a sample of ultra cold strontium atoms. Using laser cooling temperatures in the μK range can be achieved with strontium atoms (see further discussion on laser cooling in section 2.2). Even at these ultra cold temperatures the Doppler broadened linewidth is still on the order of tens of kHz, far too much to achieve the required accuracy. Further cooling could decrease the Doppler broadening, but reaching temperatures in the nK range becomes increasingly complicated and at a large loss of atoms. Even a very cold 1 nK atomic sample would have a Doppler broadened linewidth at the kHz level, due to the weak square root dependence of the Doppler width on the temperature. Even the recoil transfer when absorbing a photon from the clock laser beam leads to a significant shift of ν_r=4.4 kHz.

To overcome these problems the atoms can be confined in a tight harmonic potential [17, 18]. The atoms are trapped in an optical lattice simulating a harmonic potential formed by a standing wave light pattern from a far off resonance laser. For a potential depth of the lattice much larger than the thermal energy of the atoms k_BT most of the atoms will populate the lowest vibrational ground state.

In the case of tight confinement the energy scales of the optical lattice are larger than the photon recoil and the atom is in the Lamb-Dicke regime [19]. In this state the atom cannot take up the photon recoil momentum of the clock laser, since the minimum energy scale is given by vibrational states of the lattice. Instead the momentum of the photon is taken up by the lattice potential. This allows for Doppler free spectroscopy of the atoms.

For bringing the atoms into the Lamb-Dicke Regime any far detuned lattice laser from the resonances in strontium would be suitable. But due to the AC-Stark effect the energy levels in the atom get shifted. This would lead to a frequency change of the clock transition due to an uneven shift for most wavelengths. To overcome this problem the lattice laser needs to be at the “magical wavelength”[17]. At this wavelength the shift from the ground and excited state are equal. The “magic wavelength” for strontium is at an easily accessible 813.428 nm [2]. Yet trapping atoms in a lattice at the “magic wavelength” does not prevent broadening effects from collisions. Since several atoms are trapped in a single lattice site collisions between these will cause a broadening of the measured clock transition. These effects have been exhaustively studied in [20–24].

Strontium is the most promising candidate for an optical lattice clock. The level structure of strontium (for a detailed discussion of the level structure see section 2.1) allows it to reach very low temperatures of a few μK by laser cooling with mainly diode lasers and has a convenient wavelength of 813 nm to trap it in an optical lattice. It offers a very narrow transition (<10 mHz), which is insensitive to most external fields.

1.2.3 Current Status of Neutral Atomic Clocks

Neutral atom clocks in an optical lattice have come a long way since the initial proposal by Katori [25], with the first realisation in 2003 [26]. Already by 2006 several absolute frequency measurements of fermionic strontium were reported by groups from the JILA [27], SYRTE [28] and Tokyo [29], leading to an accepted value for the frequency of the atomic transition in fermionic strontium of 429 288 004 229 873.7 Hz, with a fractional uncertainty of $1 \cdot 10^{-15}$. It was acknowledged as a secondary representation for the definition of the SI second [30]. In recent times the PTB joined the group of measured strontium frequencies [31]. With updated measurements from the other groups [32–34] a good agreement between these measurements was reached and the recommended frequency value for the secondary representation of the second is now defined by ^{87}Sr, as shown in figure 1.3. The main limitation of these measurements is not from the lattice clock, but by the caesium fountain clocks used as a reference.

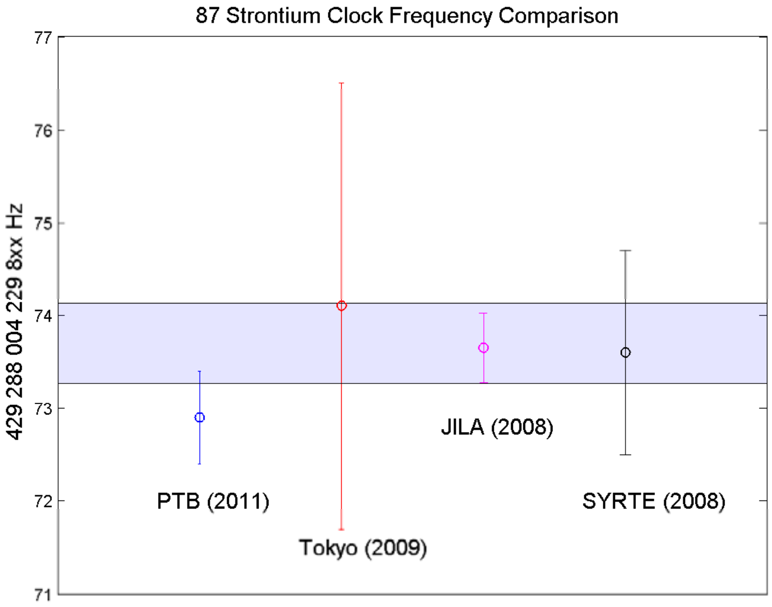

FIGURE 1.3: ^{87}Sr Clock frequency comparison of the latest absolute frequency measurements from SYRTE [32], JILA [33], Tokyo [34] and PTB [31]. Light blue bar shows recommended value from CIPM [30] from initial measurements in 2006

Not only strontium, also other elements such as Yb and Ca are showing promising developments towards the realisation of a lattice clock. Table 1.1 gives an overview of the state as of mid 2011 of such clocks.

But also the field of ion clocks is not sleeping and recently an Al+ logic clock has reached a record uncertainty in the 10^{-18} level [1, 4].

Current research efforts are focussing on the black body radiation (BBR) shift, which

Table 1.1: Overview of current state of neutral atomic clocks. The fractional uncertainty is measured by comparison with other atomic clocks.

Species	**Transition**	**Fractional Uncertainty**	**Systematic Uncertainty**
^{87}Sr	^{1}S$_0$-^{3}P$_0$	$1.4 \cdot 10^{-16}$ [33]	$8.6 \cdot 10^{-16}$ [33]
^{171}Yb	^{1}S$_0$-^{3}P$_0$	$3.4 \cdot 10^{-16}$ [35]	$1.4 \cdot 10^{-15}$ [35]
^{174}Yb	^{1}S$_0$-^{3}P$_0$	$1.5 \cdot 10^{-15}$ [36]	$1.8 \cdot 10^{-15}$ [36]
^{88}Sr	^{1}S$_0$-^{3}P$_0$	$2.9 \cdot 10^{-15}$ [37]	$3.0 \cdot 10^{-15}$ [37]
^{40}Ca	^{1}S$_0$-^{3}P$_1$	$6.6 \cdot 10^{-15}$ [38]	$7.5 \cdot 10^{-15}$ [38]

is currently dominating the uncertainty budgets of lattice clocks. The BBR shift arises from an unequal perturbation of the ground and excited clock state, caused by the thermal radiation of the environment, such as the vacuum chamber and the heated strontium source. At room temperature ($t \approx 300\ K$) the fractional shift caused by BBR is at the 10^{-15} level with an uncertainty of $1 \cdot 10^{-16}$ [31, 33], being comparable to the best reported uncertainties shown in table 1.1. Recently the first systematic measurements have lowered the uncertainty associated with the correction of the BBR shift, which translates to a $5 \cdot 10^{-18}$ relative frequency uncertainty at room temperature [5].

1.3 Applications of the Next Generation Atomic Clocks

Atomic clocks play an important role in a range of applications ranging from everyday life to a variety of scientific fields.

The most well known application of atomic clocks in our everyday life are Global Navigation Satellite Systems (GNSS). Currently four global systems are operational or being setup: The American GPS, the European Gallileo, the Russian GLONASS and the Chinese BDS. Each of the typically 20-30 satellites per system have an atomic clock on board, which transmit timing signals to receivers on earth or in space. These systems have and will further revolutionize navigation of e.g. airplanes, ships and cars. When averaging the position data for stationary objects even accuracies of 1 mm can be achieved

[39]. This allows one to accurately follow the motion of for example tectonic plates or the individual movement of regional formations.

Besides using the timing information of GNSS systems for position determination, the accurate timing signal itself offers a range of applications. Providing a global time signal in the 1 ns region it can be used to synchronize large-scale electricity grids, large computer networks for stock trading or mobile phone networks.

Another important field where the stability of atomic clocks can be used is radio astronomy for Very Long Baseline Interferometry (VLBI). VLBI uses multiple radio telescopes to greatly improve the angular resolution. Crucial for the operation is precise synchronisation of the telescopes to a level only atomic clocks offer [2].

Precision Spectroscopy is a field deeply linked with the development of atomic clocks. This field is driving, or more appropriately is driven by, the advances in atomic clocks. New spectroscopy techniques and technologies are continuously being developed to improve clock performance. One of the major motivations for the development of laser cooling was for example the improvement of the accuracy of atomic clocks [40].

1.4 Portable Atomic Clocks

Most optical clocks are stationary experiments filling entire labs. They offer an unprecedented accuracy, but are limited to a stationary location. To fully characterize an optical clock and determine its accuracy, a second at least equally accurate timing signal is required. Most bigger laboratories tend to have several clocks operational for comparison and characterization. A new field now emerging is the use of optical fibre links to distribute the time signal [41]. This will allow the transfer of stabilised laser light over hundreds of kilometres using standard telecommunication fibres, which can be used for comparison of clocks over long distances. But these systems currently require very expensive dark fibres and special repeater stations every 100 km, currently limiting the use to special test setups operated by large clock laboratories.

A different approach is a portable clock, which can be operated at various different sites, allowing for comparison of a wide variety of clocks. The first steps towards the construction of building a portable clock will be presented in this thesis. Having a portable clock would allow for the evaluation of different systematic effects and to verify the reproducibility of different optical frequency references, as would be required for the redefinition of the SI second.

1.4.1 Space Applications

With the rapid improvement of optical clocks in recent years and the best of them nearly reaching accuracies of one part in 10^{-18}, many effects previously neglected, have to be taken into account. The operation of these clocks will strongly depend on their elevation as described in section 1.4.2. With the redefinition of the SI second to an optical standard being discussed, optical clocks worldwide would serve as a reference. This requires the knowledge of the height of the clock to one cm or better, if the improvements gained by an optical standard are to be used. To be more precise, not the height distance of the mean sea level is required but the distance from the earth's geoid, which is defined as a hypothetical surface of constant gravitational potential.

To have an international time scale, as currently in operation with around 50 Caesium clocks contributing [43], benefiting from the increased accuracy, it would not be sufficient to carefully map the geoid to the required precision since the geoid is not at rest. It is

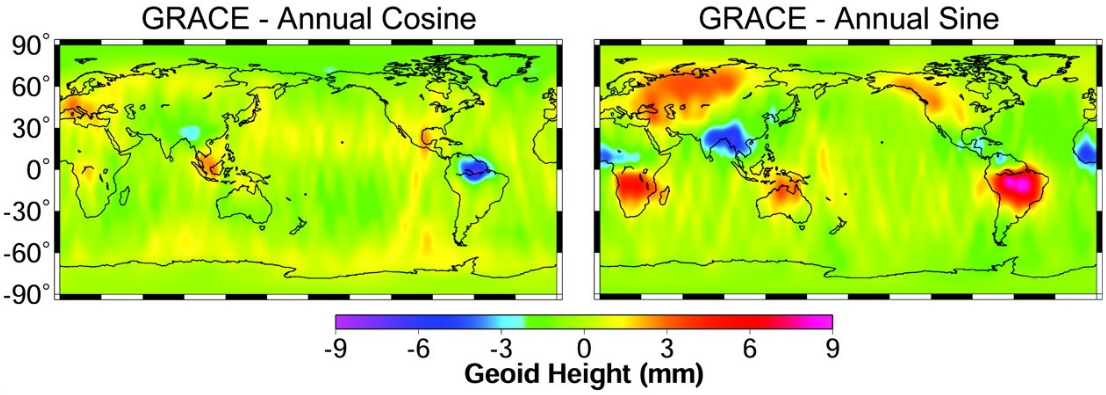

FIGURE 1.4: Measurement of the geoid by the satellite GRACE [42]. The cosine showing the annual absolute change of the geoid for summer and winter. The sine showing the change for spring and autumn.

being influenced by a host of processes, such as solid earth tides which can introduce fluctuations of up to 20 cm. Other effects include oceanic tides, effects of atmospheric pressure on ocean levels, and longer term effects such as glacial melting [44]. Annual effects at a global scale were measured by the GRACE mission [42]. Figure 1.4 is showing the measured data showing geoid movements of up to two cm on an annual basis. One could say earth is too noisy for the next generation of optical clocks [45].

To avoid such problems, future optical clocks could be set in space. Space offers a much more stable environment, where the effect of earth's gravitational field can be reduced by choosing higher orbits [46–49]. The operation of optical clocks in space has however numerous challenges to be overcome [50], with simple considerations including mass and power budgets as well as autonomous operation. The setup introduced in this thesis can be seen as a step towards optical clocks in space, with parts like the 2D-MOT and the use of permanent magnets reducing the size, weight and required power of an optical clock. Despite the additional required effort, operation in space offers a range of potential applications [51]:

Optical master clock in space An optical clock in space could be used as a master clock to distribute time and frequency to other clocks on earth and in space. Such a clock, or an array of such clocks, would allow for the comparison of optical clocks on earth to create the international atomic time scale [51].

GNSS The use of optical clocks on board GNSS satellites could improve the uncertainty budget. Although atmospheric effects play an important role for earth positioning, satellite ranging would greatly benefit from the increased stability.

Tests of fundamental physics The environment in space offers a number of advantages for tests of fundamental physics, such as variable gravity potentials, large distances, high velocity and low acceleration regimes [52]. The comparison of an optical clock in a elliptical orbit to a reference clock would allow an unprecedented test of the gravitational red shift. This would allow the further verification of Einstein's Theory of Relativity or might show the existence of quantum effects in gravity, providing support for emerging theories aimed at unifying the fundamental theories of gravity and the standard model [53].

1.4.2 Relativistic Geodesy

With optical clocks reaching a level of accuracy in the one part in 10^{-18} region [1, 4] a whole new range of external effects has to be taken into account. One of the now clearly visible effects as discussed in the previous section is the frequency shift due to gravitation. Clocks with an accuracy in the lower 10^{-17} level will be able to see a frequency change if moved by height of 10 cm (see calculations below). For a precise comparison of such clocks the difference of the gravitational potential at the clock sites has to be known to an equivalent spatial determination of a few cm [54]. On the other hand, using this effect, it is possible to determine the gravitational potential to such an accuracy. For such a measurement the comparison to a reference clock is necessary. The microwave link of the Atomic Clock Ensemble in Space (ACES), could offer the required stability in the 10^{-17} range with an averaging time of one day [55, 56].

With a portable setup, measurements of the gravitational potential at various places on Earth would be feasible. The advantages of using an optical clock are its ability to measure the absolute value of the gravitational potential and the achievable spatial resolution, mainly only being limited by the position determination. So far the most exact measurement of the earth's gravitational potential has been done by the satellite GRACE [57]. It is able to measure with a resolution of 1 cm, but due to its altitude of 450 km the spatial resolution is limited to 150 km.

A main motivation for an on-site measurement is the internationally standardised height system. Current height systems are based on country-specific geodetic points, like the Mean Sea Level on the coast of a country. The difference between these height systems is usually between a few centimetres up to a few decimetres [58]. With a portable atomic optical clock it would be possible to combine the different height systems to a common geoid.

The change in frequency in different gravitational potential is caused by the gravitational redshift, which was predicted by Einstein's theory of relativity. For two identical clocks operating at the locations r_1 and r_2 the ratios of their frequencies will depend on the Earth's geopotential U at the location of each clock. If we assume a stationary observer the frequency ratio can be written as [59]:

$$\frac{f(r_1)}{f(r_2)} \approx 1 - \frac{U(r_2) - U(r_1)}{c^2} \tag{1.1}$$

with c being the speed of light. A more detailed theoretical discussion can be found in [60]. With $\Delta U = U(r_2) - U(r_1)$ and $\Delta f = f(r_2) - f(r_1)$ we can rewrite the fractional uncertainty from eq 1.1 in a more practical form:

$$\frac{\Delta f}{f(r_2)} = \frac{\Delta U}{c^2} \tag{1.2}$$

If we assume a frequency uncertainty of $\Delta f/f \approx 10^{-17}$ of the two clocks the corresponding minimum detectable height change can be calculated. This frequency uncertainty corresponds to a change in the gravitational potential of $\Delta U = c^2 \cdot 10^{-17}$. The corresponding shift in gravitational potential can be calculated by an assumed height difference between the two clocks of Δh, which leads to:

$$\Delta U = \frac{GM_E}{R_E} - \frac{GM_E}{R_E + \Delta h} \approx \frac{GM_E \Delta h}{R_E^2} \tag{1.3}$$

where G is Newton's gravitational constant, $R_E \approx$6371 km is earth's mean radius and $M_E \approx$5.97$\cdot 10^{24}$ kg is earth's mean mass. With these values we can obtain sensitivity in geoid height of $\Delta h \approx$10 cm. A first validation at this level has already been performed by a stationary clock operating in the low 10^{-17} level. It was raised by 33 cm with a difference in the beat signal with a reference clock being visible [61].

Chapter 2

Laser Cooling and Trapping of Strontium

The development of laser cooling has led to a whole new range of exciting research fields in physics [62]. The trapping and cooling of atoms in a magneto optical trap (MOT) has allowed researchers to study atoms at long interaction times and very low temperatures. It has also laid the path to reach ultra cold quantum degenerate gas regimes creating Bose-Einstein condensates (BEC) [63] and degenerate Fermi gases (DFG) [64]. Most importantly it has lead to tremendous improvements in spectroscopy and enabled major advances in its development. These advances were only made possible by the use of laser cooling. The research community using laser cooled atoms is still continuously growing and is applying the advantages to many new exciting fields [62, 65].

Historically alkali atoms, mainly rubidium, have been the choice for laser cooling. Their single valence electron offers a simple structure and cooling transitions are at diode laser-friendly wavelengths. It is no surprise that the first BEC [63] was achieved with Rubidium and Potassium was used in the first DFG [66].

Isotope	Nuclear Spin	Atomic Mass in u	Relative Abundance
^{88}Sr	0	87.905 6121(12)	82.6 %
^{87}Sr	9/2	86.908 8771(12)	7 %
^{86}Sr	0	85.909 2602(12)	9.9 %
^{84}Sr	0	83.913 425(3)	0.56 %

TABLE 2.1: Natural stable strontium isotopes [67], with u≈$1.66 \cdot 10^{-27}$ kg

Alkaline earth atoms have, until recently, been pursued by only a few labs, mainly due to the more challenging wavelengths required for laser cooling and trapping. But the same two electron level structure causing the greater laser requirements, also offer various experimental possibilities.

This chapter will give an overview of the strontium atom and its characteristics. The concepts of laser cooling and magneto-optical trapping of atoms will be introduced, as well as a two dimensional magneto-optical trap (MOT) which is used to pre cool the atoms. A simulated estimation of the expected flux of the 2D-MOT will be given.

2.1 The Strontium Atom

Strontium is part of the alkaline earth atoms with two valence electrons in the outer shell. For these atoms the energy levels can be grouped into two separate classes, one with parallel total electronic spin S=1 (triplet state) and one with anti-parallel total electronic spin S=0 (singlet state). Electric dipole transitions between these state are forbidden due to the selection rule ΔS=0, but actually spin-orbit interaction provides a finite lifetime allowing dipole transitions to take place. These ”intercombination lines” are very narrow in frequency making them very interesting for metrology applications.

Strontium has four natural isotopes. The isotopes are listed in table 2.1 along with their nuclear spin, relative atomic mass and abundance. The work on this experiment is mainly focussed on the most abundant isotope ^{88}Sr. The bosonic isotopes of strontium have zero nuclear spin, thus states with J=0 have no hyperfine levels and are therefore not sensitive to stray magnetic fields. The insensitivity to magnetic fields adds to the attractiveness of strontium as a candidate for an optical clock.

For an atom to be suitable as a reference for an atomic optical clock, it needs to have some key features. (i) The most important one is a very narrow transition in the optical range. (ii) To efficiently cool and trap the atoms a strong cooling transition with a short cycling time is required. (iii) Also a narrow transition is favourable to easily reach ultra cold temperatures to trap the atoms in an optical lattice (see section 1.2.2). The most promising and most studied atoms are alkaline earth atoms such as Mg [68], Ca [69] , Sr [31] and a few others like Yb [70] and Hg [71]. The double valence electrons give rise to the previously discussed intercombination lines. The main advantage of strontium is that most of the required wavelengths are in the visible or near infrared range, with all of them being directly accessible by diode lasers. This greatly reduces the complexity of the setup, which is favourable for a mobile experiment.

The atomic structure in strontium allows for two main cooling transitions (see figure 2.1). One at 461 nm is a broad transition with a linewidth of $\gamma/2\pi$=32 MHz allowing for efficient cooling. The other one at 689 nm is a narrow transition with a linewidth of $\gamma/2\pi$=7 kHz enabling Doppler limited cooling to reach low μK temperatures (see section 2.2) [72]. The relevant transition lines in strontium are shown in figure 2.1 following the Russel-Saunders notation [73] of $^{2S+1}L_J$, where S is the total spin of the electrons (for strontium S is either 0 or 1), L is the angular momentum of the electrons and J is the total angular momentum of the state. In the following an overview of the relevant transitions in strontium for our experiment will be given.

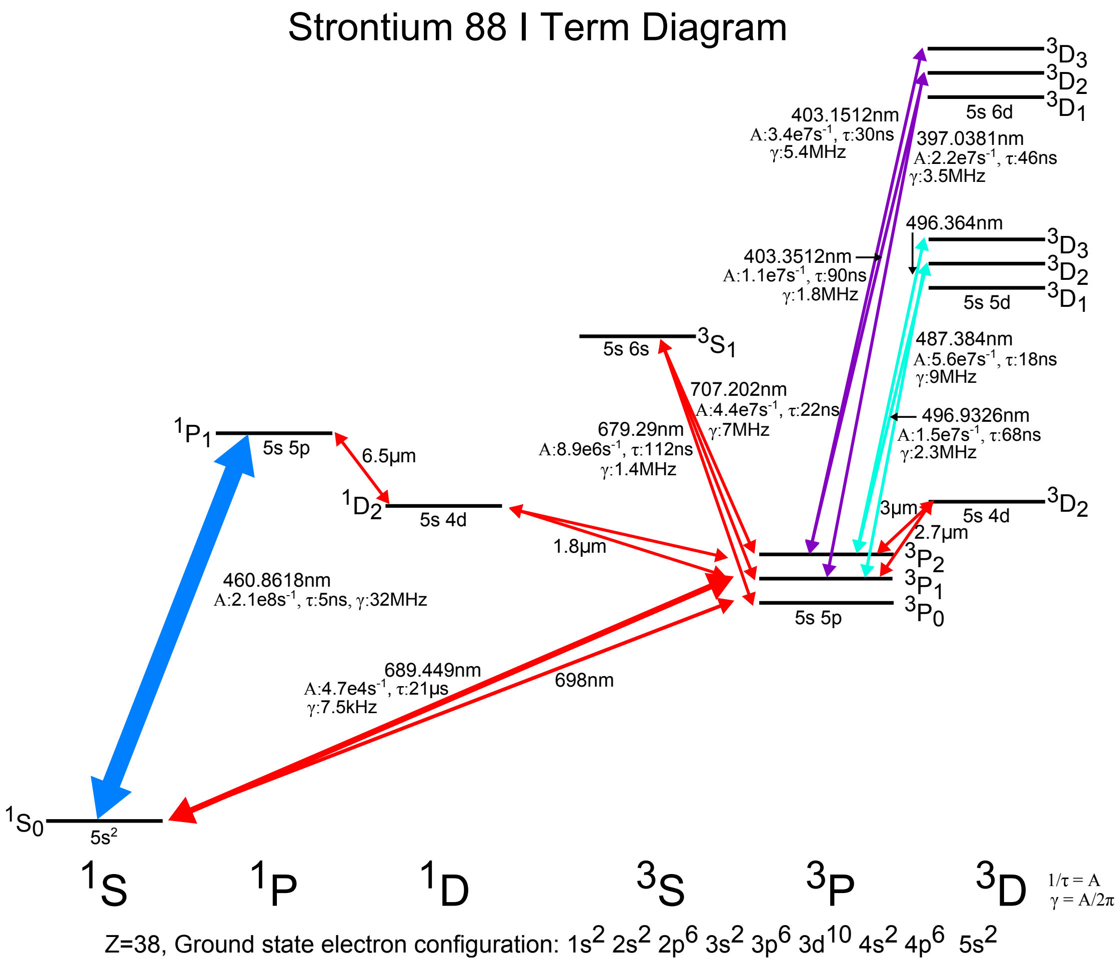

FIGURE 2.1: Termdiagram for ^{88}Sr. Data from [74]

Relevant atomic transitions in strontium [74]:

Cooling transition 461 nm: The cooling transition from $^1S_0$ to $^1P_1$ has a broad natural linewidth of 32 MHz at a wavelength of λ_{vac} =460.8618 nm and a frequency of $\nu = 6.505042 \cdot 10^{14}$ Hz. With a branching ratio of $2 \cdot 10^{-5}$ the electron will not decay directly back into the ground state, but into the $5s4d\ ^1D_2$ state. From here it will decay into the $5s5p\ ^3P_2$ or the $5s5p\ ^3P_1$ state with a probability of 33% and 66% respectively.

2nd stage cooling transition 689 nm: With a linewidth of only 7.5 kHz the $^1S_0$ to $^3P_1$ transition will be used for the second stage cooling, allowing for low Doppler limited temperatures. It has a wavelength of λ_{vac}=689.4483 nm and a frequency of $\nu = 4.348296 \cdot 10^{14}$ Hz.

Repumpers: Atoms which have decayed into the $5s5p\ ^3P_1$ state, which has a lifetime of $\tau = 21\ \mu$s, can directly decay into the ground state. But atoms which decayed into the metastable $5s5p\ ^3P_2$ state cannot directly decay into the ground state. A repumping laser is required to pump the atoms to the $5s5p\ ^3P_1$ state from which they can decay to the ground state. Currently three types of repumping schemes are used on strontium experiments:

$5s5p\ ^3P_2 - 5s5d\ ^3D_2$: This repumping setup only requires one laser at the wavelength of λ_{vac}=496.9326 nm to pump electrons from the $5s5p\ ^3P_2$ state into the $5s5d\ ^3D_2$ state. From this state they can decay back into the $5s5p\ ^3P_1$ state and then to the ground state. Currently there are no laser diodes available at this wavelength, hence a frequency doubling setup is required.

$5s5p\ ^3P_2 - 5s6s\ ^3S_1$ and $^3P_0 - 5s6s^3S_1$: This repumping setup requires two lasers, one at 707 nm and one at 679 nm. The electrons are pumped to the $5s6s\ ^3S_1$ state by a laser at λ_{vac}=707.202 nm. From here they can decay to any of the $5s5p\ ^3P$ states. If they decay to the $5s5p\ ^3P_2$ state they are again pumped to the $5s6s\ ^3S_1$ state. If they decay to the $5s5p\ ^3P_1$ state they can decay to the ground state. And if they decay to the $5s5p\ ^3P_0$ state a second repumping laser at λ_{vac}=679.289 nm is required to pump them again to the $5s6s\ ^3S_1$ state. Since laser diodes are available for both wavelengths this scheme was chosen for our experiment.

$5s5p\ ^3P_2 - 5s4d\ ^3D_2$: This repumping setup only requires one laser at the wavelength of λ_{vac}=3.0 μm to pump electrons from the $5s5p\ ^3P_2$ state into the

$5s4d\ ^3D_2$ state [75]. From this state they can decay back into the $5s5p\ ^3P_1$ state and then to the ground state.

Clock transition: The $^1S_0 -^3 P_0$ transition has a natural linewidth of one mHz in fermionic ^{87}Sr and a measured frequency of 429,228,004,229,874.0(1.1) Hz [2]. In bosonic strontium this transition is not accessible without the aid of external fields. With a field of 1 mT a small fraction of the nearby $^3P_1$ can be mixed into the $^3P_0$ state, allowing single photon excitations of the clock transitions [76].

2.2 Laser Cooling and Trapping

The concept behind laser cooling is that light, like matter, has both momentum and energy. By transferring the momentum in a directed way, the velocity of the atom can be decreased. When a photon is absorbed by an atom, conservation of momentum dictates that the momentum of the photon $\vec{p}_{ph} = \hbar\vec{k}$ is absorbed by the atom, where $|\vec{k}| = 2\pi/\lambda$ is the light wave vector and λ is the wavelength of the light. Considering a velocity vector $\vec{v}$ of the atom and a light k-vector $\vec{k}$, then the atomic momentum is changed from $\vec{p}_{atom} = m\vec{v}$ to $\vec{p}_{atom} = m\vec{v} + \hbar\vec{k}$. The photon is reemitted while the atom relaxes from the excited state to the ground state via a spontaneous decay process. The photon is emitted in a random direction. Averaging over many emissions, the momentum transfer of the emitted photon averages to zero and the atom only experiences a momentum change from the absorbed photons. As the atoms are in motion while cooling, the frequency of the laser will be shifted by the Doppler shift $\Delta\omega_D = \vec{k} \cdot \vec{v}$.

We now consider the simplified case of the atoms moving only in one dimension and with two counter propagating beams. The beams are red detuned with respect to the atomic transition. For an atom travelling in the opposite direction as the beam propagates, it will see a "blue" shift in the frequency, i.e. the photons appear at a higher frequency due to the Doppler effect. The atom is now more likely to absorb a photon from the beam opposing its direction than the other one, resulting in a cooling force. For the case of low light intensity the forces of the two counter propagating beams can simply be added up [62] $\vec{F}_{OM} = \vec{F}_+ + \vec{F}_-$, with $\vec{F}_+$ being the force from one laser beam and $\vec{F}_-$ the force from the counter propagating laser beam which include power broadening of the line at higher intensities:

$$\vec{F}_\pm = \frac{\hbar\ \vec{k}\ s_0\ \gamma/2}{1 + s_0 + (2(\delta \mp |\Delta\omega_D|)/\gamma)^2} \tag{2.1}$$

with γ being the line width of the atomic transition. $s_0 = I/I_s$ is the ratio of laser intensity to the saturation intensity and δ is the detuning of the laser. Note the change of signs in the denominator. When the atom absorbs a photon from one beam it cannot absorb a photon the the other beam until the absorbed photon is emitted. For the case of higher intensities this will cause a slight over estimation of the force for each beam on the atom.

For $\delta < 0$ this force looks like a frictional force and therefore viscously damps the atomic motion. Due to the similarity with a viscous fluid this damping is called "optical molasses" [77].

The atoms would be slowed down to zero velocity and zero temperature if there were no other influence on the atomic motion, a clearly unphysical result. Due to the discrete size of the momentum steps from the photon absorption and the random decay process the atoms are also heated. During each decay process the kinetic energy of the atom changes at least on average by the recoil energy E_r=$\hbar\omega_r$. For each scattering event the light field loses an average energy of $2\hbar\omega_r$, one $\hbar\omega_r$ for the absorption and one $\hbar\omega_r$ for the emission. This loss occurs at a rate of $2\gamma_p$ (two beams), where γ_p is the scattering rate of one beam. The energy becomes kinetic energy since the atoms recoil from each event. The atom is therefore heated due to the random direction of the recoils. At a steady state the rates of the heating and cooling are in equilibrium. The temperature of the atoms in this state can be found by equating the cooling rate, $\vec{F} \cdot \vec{v}$, to the heating rate, $4\hbar\omega_r\gamma_p$, and is shown to be [62]:

$$T_D = \frac{\hbar\gamma}{2k_B} \tag{2.2}$$

T_D is called the Doppler temperature and represents the lowest achievable laser cooling of a simplified two level atom. Atoms having degenerate sub-levels can be further cooled by techniques such as Sisyphus cooling [78, 79]. The lowest achievable temperature of laser cooling is set by the recoil energy acquired from spontaneous emission, with the exception of very special schemes allowing for the cooling of atoms below this limit, like for example velocity selective coherent population trapping (VSCPT) [62, 80]. The atom will at least have the momentum from the last emitted photon and thus is limited to the recoil temperature:

$$T_r = \frac{\hbar^2 k^2}{k_B m} \tag{2.3}$$

where m is the mass of the atom.

Doppler cooling is a useful technique for cooling atoms, but it is not suitable for trapping, since it has no spatially dependant force. To achieve trapping of atoms, a combination of both optical and magnetic fields can be used. The magnetic field adds a spatially dependent component to the force. For a simple $J_g = 0 \rightarrow J_e = 1$ transition the

Zeeman components are shifted by the magnetic field and therefore with position. The arrangement of such a magneto-optical trap (MOT) is illustrated in figure 2.2 for the simplified case in one dimension.

In the excited state $m_j = +1$ is shifted up for B>0 and $m_j = -1$ is shifted down. At position x' in figure 2.2 the $\Delta m_j = -1$ transition is shifted closer to resonance and the $\Delta m_j = +1$ transition is shifted further away. In combination with the selection rule for circular polarized light of $\sigma^{\pm} \rightarrow \Delta m_j = \pm 1$ this results in more absorption of the σ_- beam, thus a net force towards the centre of the trap. On the other side of the trap the roles are reversed and the atoms are also driven towards the centre. Since the laser light is tuned below resonance, compression and cooling are achieved simultaneously.

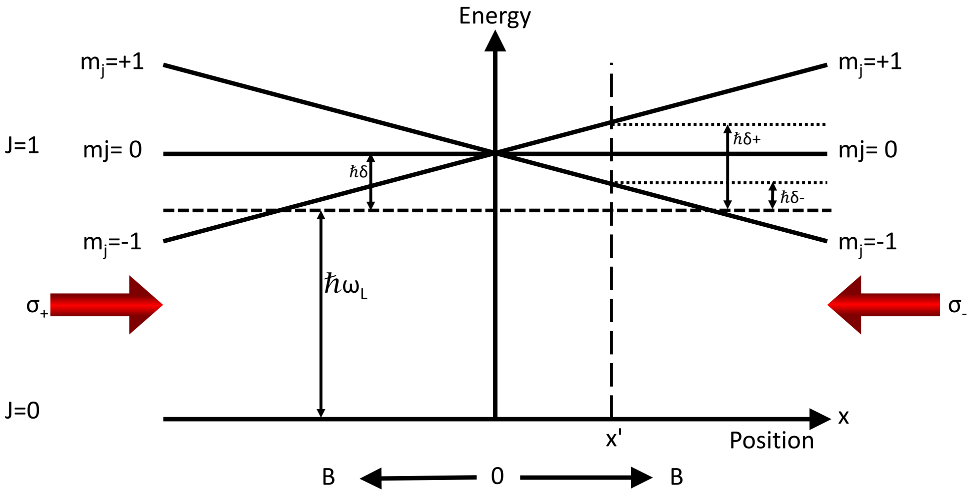

FIGURE 2.2: Diagram of the Zeeman-levels in a MOT configuration. At the position x' the light from the left is σ^+ and from the right σ^- polarized. The magnetic field linearly increases from the centre. The Zeeman shift by the magnetic field of the $m_j = -1$ state permits preferential absorption of the σ^- polarized light field to push the atoms to the centre. Due to the red detuning of the laser higher velocities become resonant further away from the centre. On the left hand side the direction of the magnetic field changes and the roles of the light fields are reversed.

To quantify the cooling force of a MOT, equation 2.1 needs to be modified to incorporate the Zeeman detuning of the magnetic field $\delta_{Zeemann} = (g_e m_e - g_g m_g)\mu_B B/\hbar$ (with g and e referring to the ground and excited state, g$_{g,e}$ being the Landé g-factor, μ_B the

Bohr magneton and $m_{g,e}$ being the magnetic quantum number) as well as the Doppler shift $\vec{k} \cdot \vec{v}$:

$$\delta \rightarrow \delta_{\pm} = \delta \mp \vec{k} \cdot \vec{v} \pm (g_e m_e - g_g m_g) B/\hbar \tag{2.4}$$

The resulting force per axis is, as was the case for Doppler cooling, the sum of the force from each laser beam:

$$\vec{F}_{MOT} = \vec{F}_{+} + \vec{F}_{-} \tag{2.5}$$

In the case of the Doppler and Zeeman shifts being small compared to the detuning δ, terms of the order $(kv/\gamma)^4$ and higher can be neglected and the denominator of the expanded equation 2.5 can be expanded to:

$$\vec{F}_{MOT} = -\beta \vec{v} - \kappa \vec{r} \tag{2.6}$$

with the damping coefficient β and the spring constant κ defined as, and dB being the gradient of the magnetic field B:

$$\beta = \frac{8\hbar k^2 \delta s_0}{\gamma(1 + s_0 + (2\delta/\gamma)^2)^2} \tag{2.7}$$

$$\kappa = \frac{(g_e m_e - g_g m_g) dB}{\hbar k} \beta \tag{2.8}$$

The force described in equation 2.6 leads to a damped harmonic motion of the atoms in the MOT, with the damping rate given by $\Gamma_{MOT} = \beta/m$ and the oscillation frequency $\omega_{MOT} = \sqrt{\kappa/m}$ [62]. When the motion of the atoms is sufficiently reduced quantum effects will begin to dominate and the harmonic oscillator approximation does not hold any more.

Strontium has two transitions easily accessible for laser cooling. The $^1S_0$ to $^1P_1$ transition has a natural linewidth of 32 MHz and it is used to precool the atoms in a two dimensional MOT (see section 2.2.1) and trap them in a MOT. The broad linewidth has the advantage of having a high cooling force to efficiently pre cool and trap the atoms. This advantage comes at the cost of a relatively high Doppler temperature of T_D=770μK, with temperatures of typically a few mK being achieved [81, 82]. The second laser cooling line is on the intercombination transition from $^1S_0$ to $^3P_1$ which is used as a second stage cooling. This transition has a natural linewidth of only 7.6 kHz, limiting the cooling force. The atoms in the first stage or "blue" MOT will be loaded into the second stage or "red" MOT for additional cooling. Due to the narrow transition it has the peculiar property of the Doppler temperature T_D=180 nK being lower than the recoil temperature T_r=460 nK, thus the lowest achievable temperature is the recoil temperature. Temperatures in the lower μK range are typically achieved in the red MOT [72, 81, 83–85].

Transition	λ	T_D	T_r	I_{sat}
$^1S_0$ - $^1P_1$	461 nm	770 μK	1.03 μK	43 mW/cm^2
$^1S_0$ - $^3P_1$	689 nm	180 nK	460 nK	3 μW/cm^2

Table 2.2: Relevant parameters for the two main laser cooling transitions of strontium [2]

2.2.1 2D MOT

Due to the low vapour pressure of strontium the atom source needs to be heated to a high temperature to have a sufficient flux of atoms. This means that the atoms velocity Maxwell-Boltzmann distribution only has a small amount of atoms in the velocity class a MOT could capture. To increase the number of captured atoms in the MOT, they are pre cooled.

In this experiment the first two dimensional MOT (2D MOT) will be used to pre cool the strontium atoms, rather than a Zeeman slower typically used with strontium [9, 86, 87]. The use of a 2D-MOT offers two main advantages over a Zeeman slower. The heated atom source, in our case a dispenser, can be installed in such a way that it has no direct line of sight with the trapped atoms for the clock operation, reducing the amount of black body radiation the atoms experience during the probing of the clock transition. Black body radiation is currently one of the main errors contributing to the error budget of strontium clocks [88]. Removing the black body radiation of the strontium oven or dispenser would improve the accuracy of the clock. The second main advantage of a 2D-MOT is the achievable pressure difference between the 2D-MOT chamber and 3D-MOT chamber. They are connected via a differential pumping stage, which creates a pressure difference of more than two orders of magnitude between these two chambers. The pressure in the 2D-MOT chamber can be optimized for the maximum flux of atoms, while the pressure in the 3D-MOT chamber can be kept low to prevent collision with the background gas.

Other advantages of the 2D-MOT, especially with respect for the requirement of portability and potential use in space, include the size of the setup. It can easily be scaled to smaller sizes and with the use of permanent magnets (see section 4.1.5) can be operated at no energy consumption.

This section will show the simulations carried out to estimate the expected flux of atoms from the 2D-MOT passing through the differential pumping stage. The effects of the laser power, detuning and the magnetic gradient will be analysed. Typical simulations assume the loading of the 2D-MOT from a thermal atomic vapour [86]. Due to the low vapour pressure of strontium, the loading of the 2D-MOT will mainly be from the beam of atoms emitted from the atomic source. To simulate the flux of the 2D-MOT the simulation presented here will mainly focus on the capture of the atoms directly emitted from the atomic source instead of thermal vapour. This work is based on similar, less complex work done during my diploma thesis [89].

Using equation 2.5 the force on a strontium atom in a MOT can be calculated, out of which the acceleration can be calculated using Newton's second law.

Using this acceleration it is possible to simulate the velocity evolution of a strontium atom passing through the MOT region. I am assuming here that the force on the atoms by the laser is continuous. Looking at the timescale of the lifetime of the main cooling transition of τ=5 ns, there is a large number of spontaneous emission cycles during the capture time, which has shown to be on the order of a few ms in my simulation. The velocity of the atom after a time t for the simplified case of a one dimensional MOT can now be calculated:

$$v(x,t) = v_0 + \int a(v,x)dt \tag{2.9}$$

Equation 2.9 is numerically approximated with a recursive formula:

$$v_n = v_{n-1} + a(v_{n-1}, x_{n-1}) \cdot \Delta t \tag{2.10}$$

with time steps of Δ t = 2 μs giving an optimum balance between computing efficiency and required resolution. The laser beams are assumed to have an equal intensity distribution for this simulation and atoms are assumed to interact with the laser beams over the range of the beam diameter. Figure 2.3 shows the simulated path of an atom in the one dimensional case. The laser beams are set to be 1 cm in diameter, the intensity is varied between I=1.25 mW/cm^2 to I=100 mW/cm^2 and the magnetic gradient and detuning are at dB=0.5 T/m and δ=-57.5 MHz, respectively.

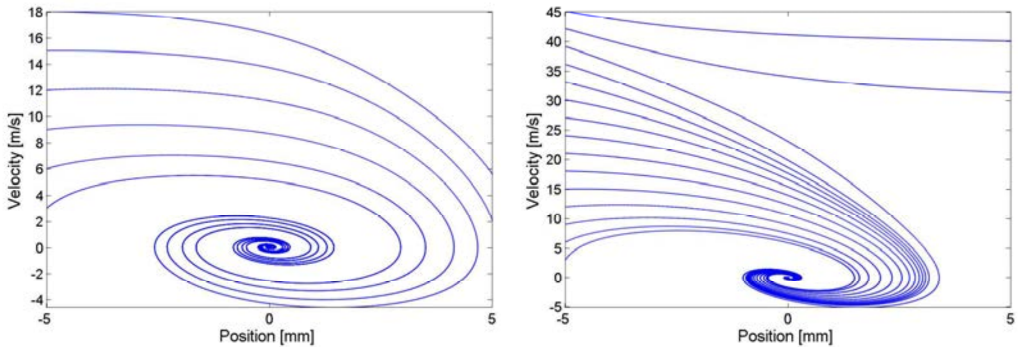

(a) I=1.25 mW/cm^2; (b) I=5 mW/cm^2;

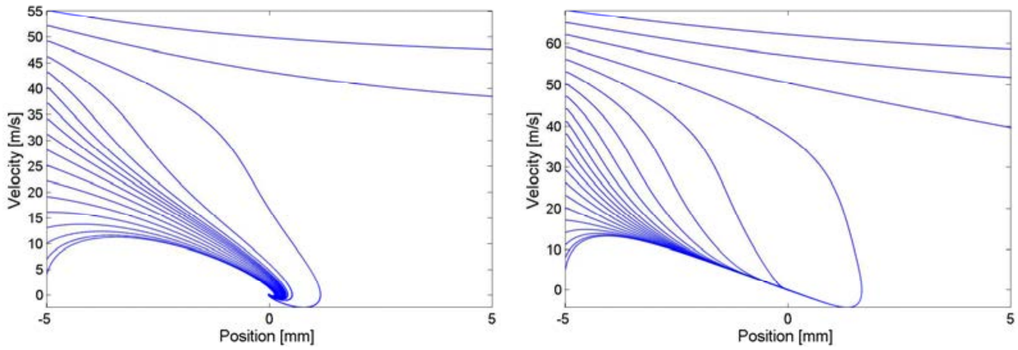

(c) I=25 mW/cm^2; (d) I=100 mW/cm^2;

FIGURE 2.3: Simulated particle trajectories for a 1D-MOT. MOT parameters for calculation at dB=0.5 T/m; δ=-50 MHz and beam width=1 cm. Laser beam intensities were varied: (a) I=1.25 mW/cm^2, (b) I=5 mW/cm^2, (c) I=25 mW/cm^2 and (d) I=100 mW/cm^2

An effect which might need to be considered is the heating of the atoms due to the spontaneous emission of the photons. Especially at low velocities, when the absorption of both laser beams is nearly equal, the emitted photons have a larger influence on the trajectory of the atom. To include this effect an emission term was included in the simulation. For every time step the number of absorbed photons is calculated and the same number of photons is emitted in a random direction. The momentum of the emissions is summed and the resulting acceleration is calculated. For the 1D case the photons are randomly emitted either in the positive or negative direction. For the 2D case the photons are emitted at a random angle. Figure 2.4 shows ten plots of the trajectory of an atom for the 1D case. All the trajectories follow the exactly the same path within the resolution of this graph, showing that the emission of the photons has a negligible effect on the trajectory of the atom. For the 2D case the emission of the photons is equally not noticeable. Also the time steps were varied to below 1 μs to where only 2-3 photons are absorbed per time step. Even here no effect of the emission was visible.

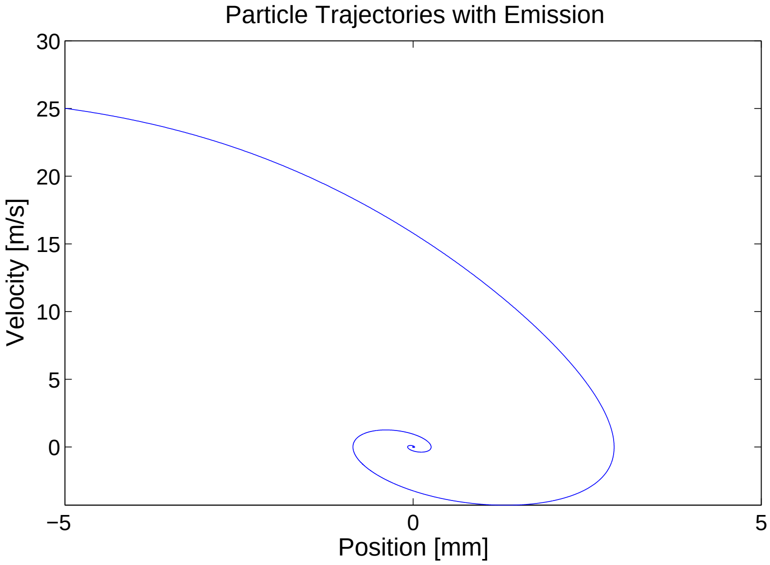

FIGURE 2.4: Particle trajectories for a 1D-MOT with the random emission process included in the simulation. Ten trajectories were plotted with no broadening of the trajectories visible. MOT parameters for calculation at dB=0.5 T/m; δ=-50 MHz, I=5 mW/cm^2 and beam width=1 cm.

I am considering two potential layouts of the 2D-MOT setup for this simulation. In one layout the dispenser is directed at a foil from which the atoms are emitted. In the other setup the dispenser is in the plane of the 2D-MOT beams emitting at an angle of 45° of the beams. A drawing of the setups can be seen in figure 2.5 showing the location of the dispensers and the foil, the direction in which atoms are emitted and the laser cooling beams. For the 45° dispenser an additional slit would be required to stop the strontium atoms coating the viewports. The foil is used instead of the dispenser pointing directly at the 2D-MOT capture region due to an expected influence of the nozzle effect. Due to the small aperture through which the atoms leave the dispenser fast atoms are likely to collide with slower atoms. From this the number of slow atoms leaving the dispenser would be reduced lowering the number of atoms we can trap in the 2D-MOT.

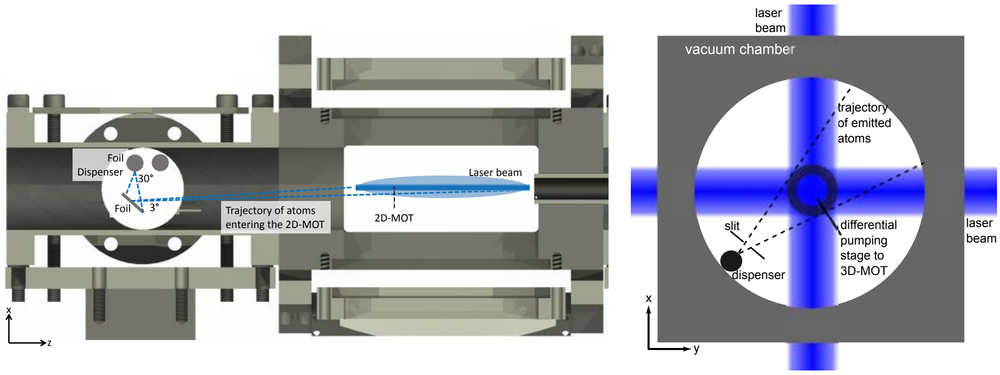

(a) Dispenser configuration for foil dispenser

(b) Dispenser configuration for 45° dispenser

FIGURE 2.5: Slice of the vacuum chamber showing the two setups of the dispenser for the 2D-MOT simulations. (a) View along the horizontal cooling beam (b) View towards the 3D-MOT

The previously introduced 1D model was extended to incorporate the specifics for each dispenser configuration. For the 45° dispenser the atoms enter the capture region at an angle of 45° relative to the MOT beams. The velocity component along each beam axis is treated separately. The atom is considered to be captured when both x- and y-velocity components are below 0.5 m/s. Since two pairs of laser beams are interacting simultaneously with the atom, this simulation will over estimate the force on the atom. When the atom has absorbed a photon from one beam it won't be able to absorb another photon until it has emitted a photon and reached the ground state again. For low intensities the atoms will mostly be in the ground state and this effect is negligible. For higher intensities, especially when getting closer to the saturation intensity of I=42 mW/cm^2, this effect will become more dominant, thus over estimating the force on the atoms and over estimating the capture velocity.

For the foil dispenser the atoms have a large velocity component in the z-direction, which is not directly affected by the laser cooling beams. This means that the interaction time with the laser beams is limited to the time it takes the atoms to pass through the capture region of the 2D-MOT. To account for this the number of simulation steps was set to match the time the atom is affected by the 2D-MOT, which is dependant on the z-velocity and the time of a simulation step. An atom is considered captured if the x-velocity is low enough when it leaves the 2D-MOT, that it is within a 2 mm radius of the centre of the differential pumping stage at the 3D-MOT exit. The differential pumping stage (see section 4.1.2) is a 18 cm long and 6 mm wide tube connecting the 2D-MOT chamber to the 3D-MOT chamber causing a two order of magnitude better pressure in the 3D-MOT chamber.

Figure 2.6 shows a surface plot of the maximum velocity v_c the 2D-MOT can capture for a beam intensity of I=5 mW/cm^2 and a varied detuning and magnetic field gradient from -5 MHz to -100 MHz and 0.1 T/m to 0.9 T/m, respectively. The maximum capture velocity plots for intensities between I=1.25 mW/cm^2 to I=80 mW/cm^2 can be found in appendix A. The plot for an intensity of I=5 mW/cm^2 is shown here since this is most likely the intensity which will be available at the final stage of the experiment. For small negative detunings v_c increases almost linearly with increasing detuning and reaches a maximum between δ=40 MHz and δ=60 MHz, depending on the magnetic gradient. The maximum v_c=59 m/s is reached at dB=0.5 T/m and δ=-60 MHz$\approx$-2γ. At a further increase in detuning, the atoms can only be cooled by the tail of the Lorentz profile, which is not sufficient to cool them to rest. This can be seen by the sharp drop of v_c after the maximum.

Figure 2.7 shows the same surface plot for the foil dispenser. Here a different shape is visible, especially the sharp drop after the maximum is less dominant. This is due to

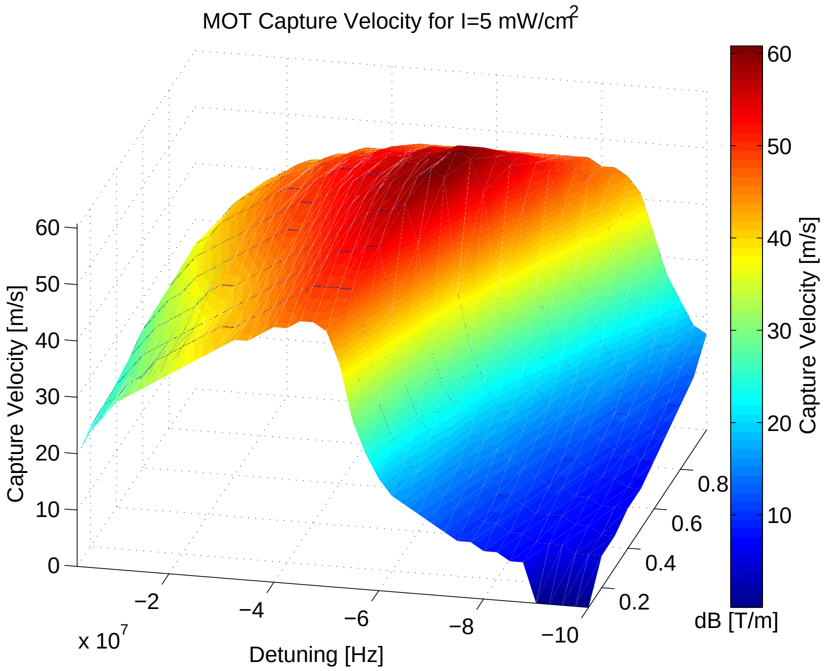

FIGURE 2.6: Maximum capture velocity surface plot of the 45° dispenser for various detunings and magnetic gradient settings for I=5 mW/cm^2 and beam width=8x1 cm.

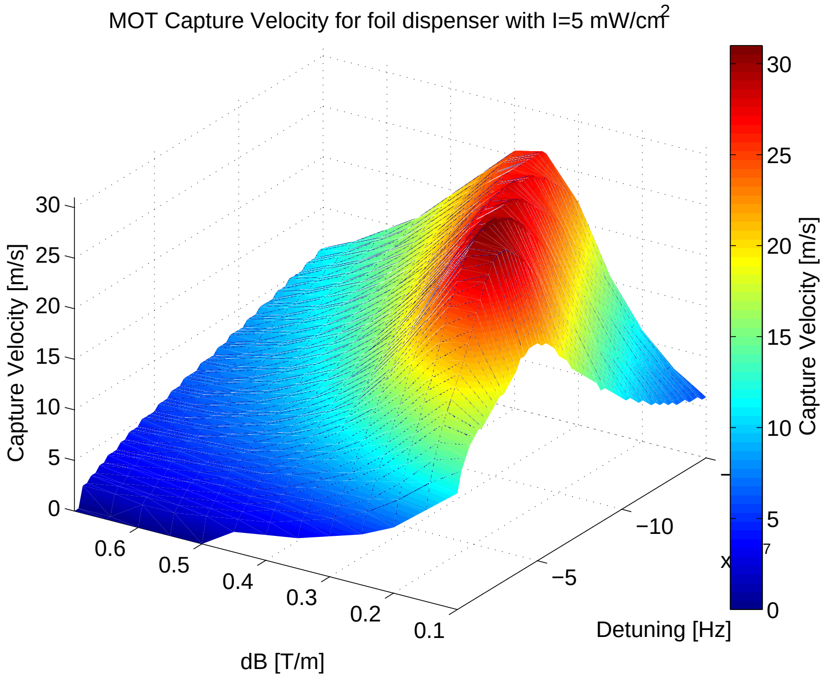

FIGURE 2.7: Maximum capture velocity surface plot of the foil dispenser for various detunings and magnetic gradient settings for I=5 mW/cm^2 and beam width=8x1 cm.

the need for a fast deceleration due to the time constraint to fulfil the requirement of being captured.

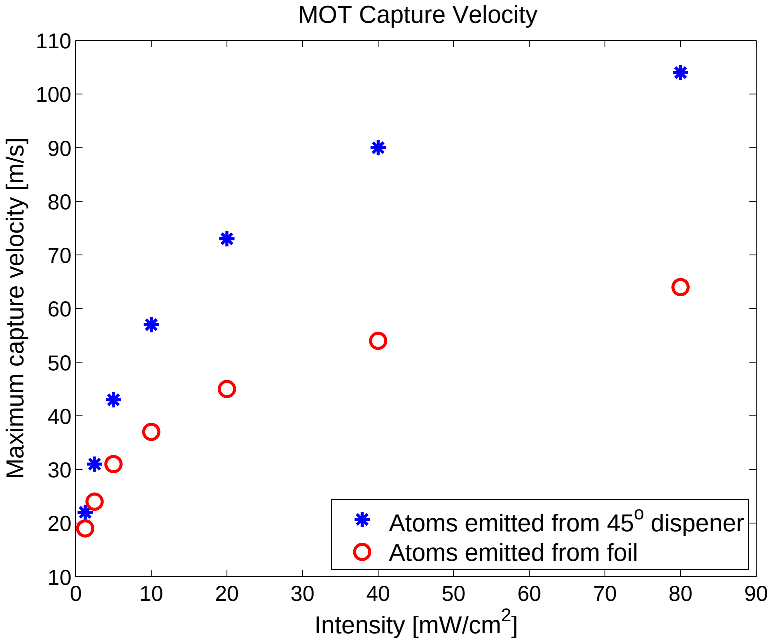

FIGURE 2.8: Simulated maximum capture velocity for beam intensities from I=1.25 mW/cm^2 to I=80 mW/cm^2 with optimized detuning and magnetic gradient for each intensity.

The maximum capture velocity v_c for intensities between I=1.25 mW/cm^2 to I=80 mW/cm^2 is plotted in figure 2.8.

Knowing the capture velocity, it is possible to determine the percentage of atoms emitted from the dispenser the 2D-MOT can capture. For this the velocity distribution of the emitted atoms needs to be known. As shown in section 4.1.3 the Maxwell-Boltzmann distribution is a good approximation of the atoms velocity distribution:

$$p(v) = 4\pi \left(\frac{m}{2\pi k_B T} \right)^{3/2} v^2 exp \left(- \frac{mv^2}{2k_B T} \right) \tag{2.11}$$

With an approximated temperature of T$_{Disp,12.5A}$=678±40 K and T$_{Disp,13.5A}$=703±15 K for the dispenser and T_{Foil}= 700±80 K for the foil (see section 4.1.3 for how the temperatures were approximated) the percentage of capturable atoms is calculated by integrating equation 2.11 to v_c. The percentage of capturable atoms for the two dispenser setups is plotted in figure 2.9. Due to the high temperatures only a small fraction of atoms can be captured by the 2D-MOT. Only at intensities higher than I=40 mW/cm^2 more than 1% for the 45° dispenser can be captured. For the foil dispenser only around 0.2% of the atoms can be captured at this intensity.

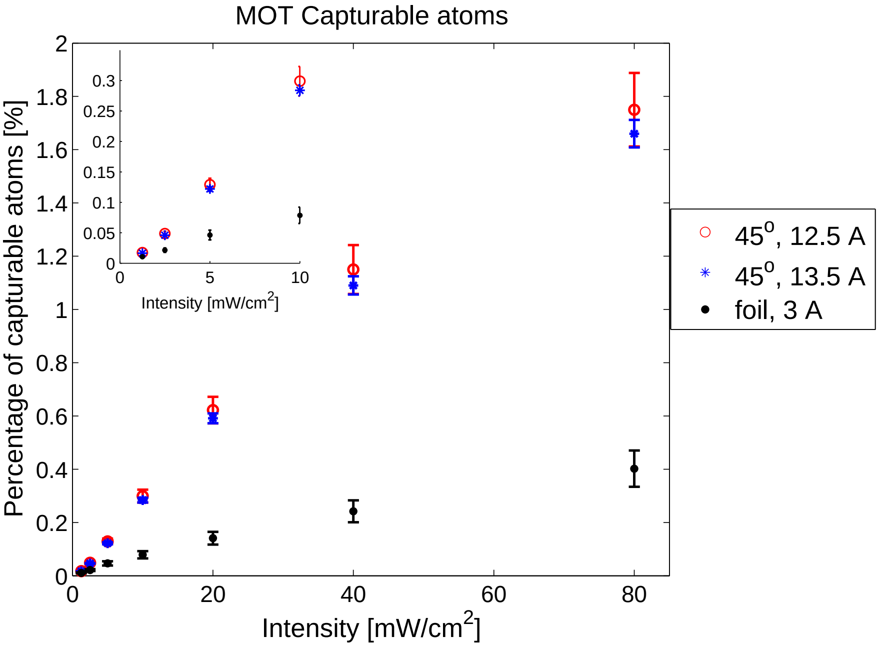

FIGURE 2.9: Percentage of capturable atoms for different temperatures with atom velocity following the Maxwell-Boltzmann distribution for beam intensities from I=1.25 mW/cm^2 to I=80 mW/cm^2. The inset is showing a zoom for intensities up to I=10 mW/cm^2. The error is due to the uncertainty in the temperature determination.

Knowing the number of atoms emitted per second from the dispenser it is possible to determine number of atoms captured per second from the 2D-MOT. In section 4.1.3 the number of emitted atoms was estimated to $(7.6+2.3-4)\cdot 10^{12}$ atoms/s and $(2.7+0.8-1.4)\cdot 10^{13}$ atoms/s for a current of 12.5 A and 13.5 A respectively. Out of these atoms 2.5% and 0.2% for the 45° and foil dispenser respectively will pass through the capture region of the 2D-MOT. Combining these numbers I can give an estimate of the number of atoms captured per second in the 2D-MOT. Assuming a 100% transfer rate of captured atoms in the 2D-MOT to the 3D-MOT the flux of the 2D-MOT can be calculated. Figure 2.10 shows the estimated flux of the 2D-MOT for the two configurations and dispenser currents of 12.5 A and 13.5 A.

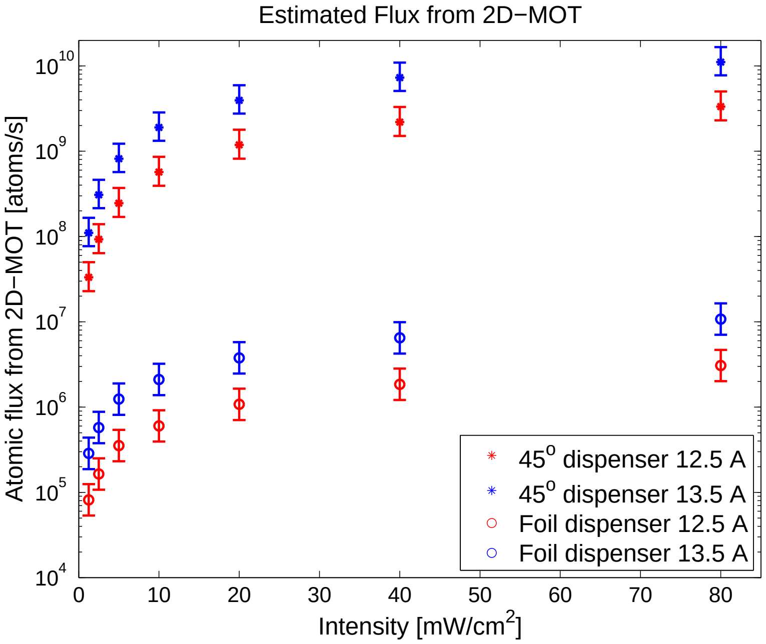

FIGURE 2.10: Estimated flux of the 2D-MOT with dispenser and foil perpendicular to 2D-MOT axis for beam intensities from I=1.25 mW/cm^2 to I=40 mW/cm^2

For the expected laser intensity of I=5 mW/cm^2 the flux of the 2D-MOT is estimated to $2.4 \pm 1 \cdot 10^8$ atoms/s and $8.2 \pm 2.5 \cdot 10^8$ atoms/s for a current of 12.5 A and 13.5 A respectively for the 45° dispenser. For the foil dispenser a flux of $3.5 \pm 1.2 \cdot 10^5$ and $1.2 \pm 0.4 \cdot 10^6$ respectively is estimated. With an increase of the laser intensity to I=40 mW/cm^2, close to the saturation intensity, and a dispenser current of 13.5 A the flux is estimated to increase to $7.3 \pm 2 \cdot 10^9$ atoms/s and $6.5 \pm 2.2 \cdot 10^6$ atoms/s for the 45° and foil dispenser respectively. Compared to a typical reported flux between $8 \cdot 10^8$ and $4 \cdot 10^{10}$ atoms/s [9, 86, 87] for experiments using Zeeman-slowers, a 2D-MOT configuration can deliver a similar order of magnitude of atomic flux with enough laser intensity. But the simulation shows that a high laser power is vital to achieve a high flux of atoms.

Our current setup (as described in chapter 4), which was planned and manufactured at the very beginning of my thesis, has the foil dispenser installed. The far simpler simulations carried out then, partly during my diploma thesis [89], did not show the potential three order of magnitude increase for the other 45° dispenser configuration. Due to the expected significant increase in flux from a 45° dispenser setup, plans are currently made to install such a dispenser in our current setup.

Chapter 3

Mobile Laser Systems

A novelty of the experiment is the mobility of the setup. Normal setups in quantum optics field are on large, stable optical tables and it would takes months to move the setup to a new location. In this experiment we are using a modular design. All the optics are tailor made and have been designed for maximum robustness, allowing the setup to be transported to different locations.

Most of the lasers and optics are in functional modules which are connected via fibres. This allows for individual modules to be replaced. These can be replacements for broken modules, if a spare one was built or upgraded modules. For example if a 461 nm laser source with more power is available, it can easily replace the existing frequency doubling module.

For the pre cooling and trapping in the 2D- and 3D-MOT a total of eight modules were built. This chapter will give an overview of these modules, highlighting the special needs for a transportable system and analyse the operational characteristics of these modules. An overview of the assembled modules can be seen in figure 3.1.

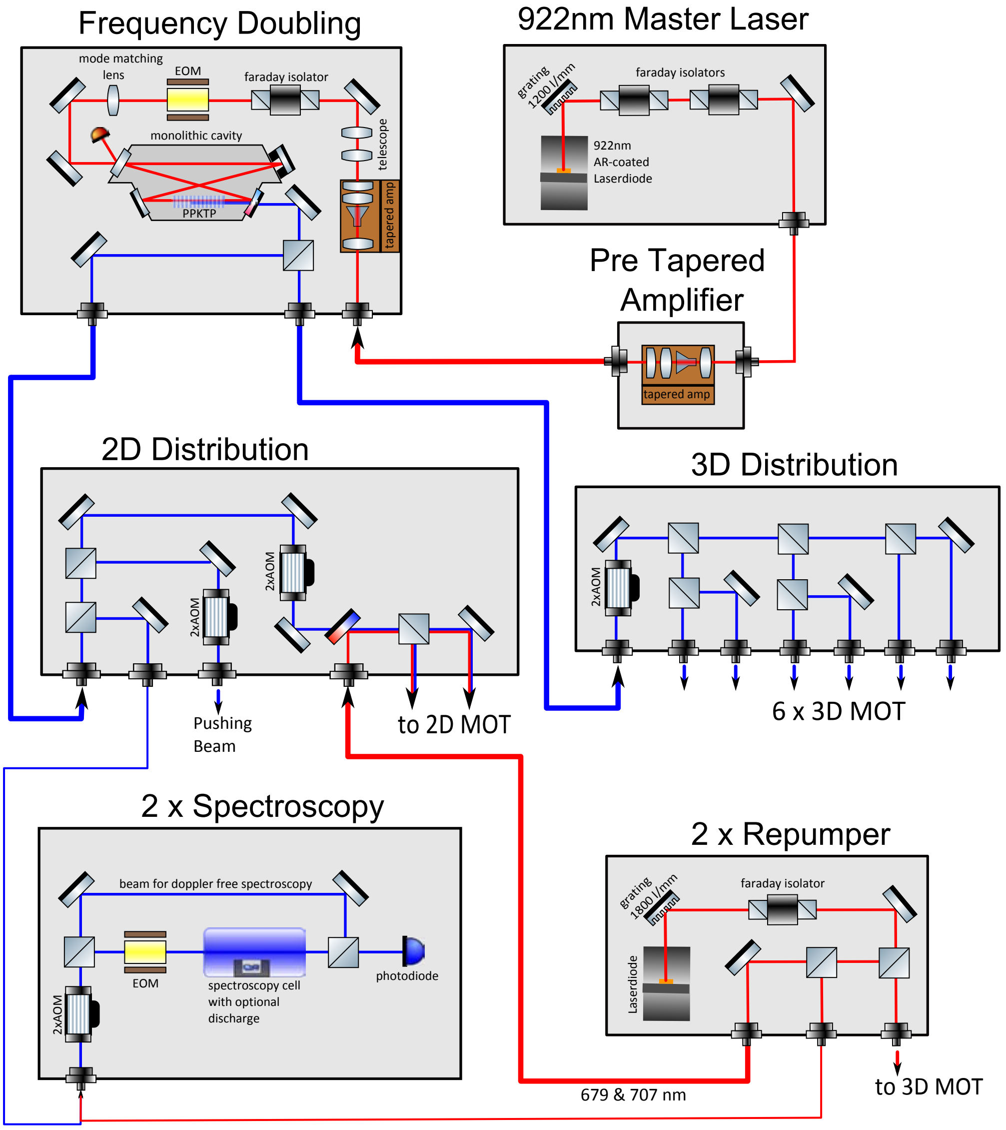

Figure 3.1: Simplified schematic overview of the major laser modules used in this experiment. Waveplates before polarizing beam splitters and fibres as well as some mirrors are omitted for a better overview. The double pass setup of the AOMs is simplified. The thickness of the fibres outside the modules is an indication of the power transported in them.

922 nm Master Laser Module: This module delivers stabilized laser light at a wavelength of 922 nm. The laser light is generated by an ECDL (Extended Cavity Diode Laser) in a Littrow [90] configuration (See section 3.3.3).

Pre Tapered Amplifier Module: In this module the 922 nm laser light is amplified to have enough seeding power for the tapered amplifier (Section 3.3.4)

Tapered Amplifier and Frequency Doubling Module: In this module the 922 nm laser light is amplified up to 1.5 W and frequency doubled to 461 nm with a maximum power of 300 mW. It is then split into two outputs (See section 3.3.5).

2D Module: In this module the light of the blue cooling laser is frequency adjusted to the correct resonance. The light for the "Pushing Beam" and detection is split from the cooling light and is also frequency adjusted. The cooling light can be overlayed with the two repumpers and can be split to up to four outputs (See section 3.5).

3D Module: In this module the blue cooling light is frequency adjusted and can be overlayed with the two repumpers and the red cooling light, which is not yet implemented. This light is then split onto six outputs (See section 3.5).

Repumping Laser 707 nm and 679 nm Module: These modules deliver stabilized laser light at a wavelength of 707 nm and 679 nm for repumping the strontium atoms. The laser light is generated by an ECDL (Extended Cavity Diode Laser) in a Littrow [90] configuration (See section 3.4).

Spectroscopy Module for Blue Laser: This module has a spectroscopy cell for stabilizing the cooling lasers on the atomic transitions (See section 3.3.6).

Spectroscopy Module for 707 nm and 679 nm Repumping Lasers: This module has a spectroscopy cell for stabilizing the repumping lasers on the atomic transitions. Due to the repumping states not being reached by the ground state, a gas discharge is included (See section 3.4.1).

3.1 Optical components

For this experiment a new range of optical component mounts is being used, having improved stability and a smaller size than commercially available equipment. We are utilizing the experience gained from other experiments of our group, which have been designed for example for the drop tower at ZARM, Bremen, Germany [91]. A selection of optical components used in this experiment are shown in figure 3.2. The main characteristic of our system is the modular design. All laser systems are built in functional modules. This allows for an easy transport, since these robust modules can be stacked. Most modules consist of a 20 mm thick aluminium baseplate in which the optical components are screwed. The optical components themselves are designed in a rigid way, for example the mirror mounts have locking screws to fix the beam alignment.

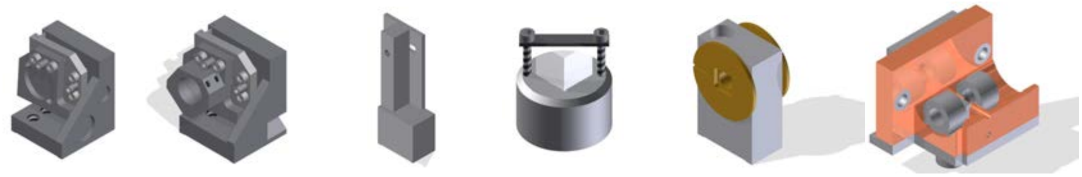

Adjustable Mirror Mount

Adjustable Grating Mount

Beam Blocker

Polarizing Beam Splitter Mount

Waveplate Mount

Tapered Amplifier Mount

FIGURE 3.2: Schematic overview of a selection of optical components used in this experiment

3.1.1 Acousto-Optic Modulator

To provide the detuned frequencies for various parts of the experiment from one laser acousto-optic modulators (AOMs) are used. By phonon-photon interaction AOMs can detune the frequencies of lasers ranging from tens of MHz to GHz. The AOMs used in this experiment[1] have a centre frequency of 80 MHz and a bandwidth of ±20 MHz. Figure 3.3 is showing the typical detuning of the 461 nm laser for the spectroscopy,

---

[1] Crystal Technologies 3080-125, centre frequency 80 MHz, active aperture 2 μm, wavelength 442-850 nm

3D-MOT, 2D-MOT and a pushing or detection beam. The frequencies in the individual modules are red detuned from the main blue laser frequency. In the example the AOM in the spectroscopy module is set at 76 MHz and double passed, which will be described in detail further below, detuning the laser by -152 MHz. The AOM in the 3D module is set at 86 MHz and double passed, resulting in a red detuning of the laser beams of -20 MHz, with respect to the atomic transition. With the bandwidth of ±20 MHz a maximum detuning difference of 80 MHz can be achieved.

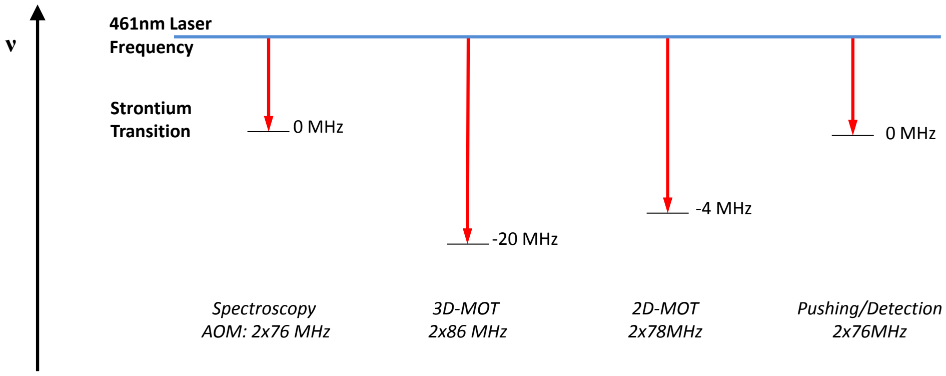

FIGURE 3.3: Exemplary overview of detuning frequencies for various parts of the blue laser. The AOMs are running in a double pass configuration at the shown frequencies. The laser is running at 2x76 MHz blue detuned from the atomic transition. For the 3D-MOT the laser is 2x86 MHz red detuned to achieve a detuning of 20 MHz and for the 2D-MOT the laser is 4 MHz red detuned.

To have a wider tuning range and maintain good fibre coupling efficiency while detuning a double-pass setup for the AOMs was chosen. This comes at the cost of less efficiency. In a single-pass efficiencies of up to 90% can be achieved.

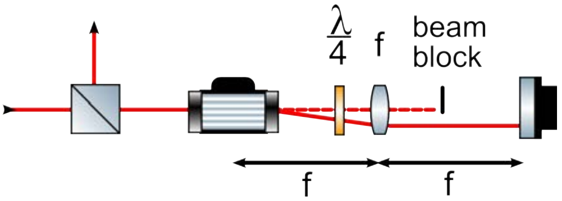

FIGURE 3.4: Schematic overview of double pass setup for AOMs. The beam enters through a PBS, gets diffracted in the AOM, the ±1st order is "collimated" by the lens and focussed onto the mirror. Due to the lens the beam will take exactly same path back.

The double pass AOM is setup in the cats eye configuration, allowing for almost no beam shift while changing the detuning. For this setup a lens is placed at its focal length behind the AOM and a mirror is placed at the same distance behind the lens (see figure 3.4). Due to the lens being at the focal length the ±1st order beam will be parallel to the 0th order and a change in detuning will only result in a shift of the beam. Because the lens will focus the beam, the reflecting mirror is placed at the focal length of the lens. The reflected light will now be recollimated on the return path. A change in detuning frequency will cause a change in the angle of the ±1st order beam, which would cause a shift of the beam in a single pass AOM setup. Because the lens is placed at the focal length after the AOM, the reflected light on the mirror is shifted but will always be reflected to the same position in the AOM. The $\frac{\lambda}{4}$ wave plate turns the linear polarisation of the beam by $\frac{\pi}{2}$ to separate the detuned beam from the incoming beam at the polarizing beam splitter (PBS). Typical efficiencies of 60-65%, measured before and after the PBS, are achieved in our setup.

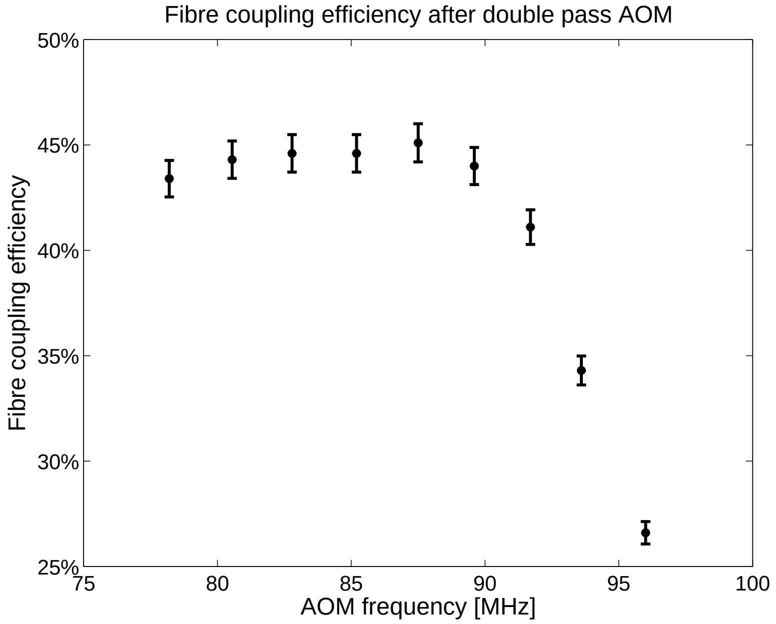

FIGURE 3.5: Coupling efficiency into a fibre after a double pass AOM. AOM centre frequency at 80 MHz. The system is optimized for 87.5 MHz and the fibre is about 50 cm after the AOM. Efficiency is defined as the power after fibre divided by the power before fibre. Error is from the uncertainty of the power meter.

In figure 3.5 the coupling into a fibre in the 3D module is plotted against the detuning. The AOM is tuned to a frequency of 87.5 MHz and the fibre coupling was optimized at this frequency. The fibre is at a distance of 0.5m after the AOM. Over a 15 MHz range the coupling efficiency is nearly constant allowing the required flexibility in changing the frequency without loosing coupling efficiency. The drop in efficiency after 92 MHz can be accounted for by the AOM reaching the limit of its bandwidth combined with a not compensated shift of the laser beam.

3.2 Blue Laser Systems evaluation

Strontium offers many advantages for an optical clock. The accessibility of most transitions by diode lasers reduces the complexity of an optical clock setup. Yet the main cooling transitions at 461 nm was only accessible by frequency doubling from diode lasers until recently. During my studies I have constructed and investigated four laser systems on their suitability for a mobile optical clock. A frequency doubling system using a cavity was built with improved cavity design for a mobile system. Another system with a fully fibre integrated waveguide was built. Furthermore two commercial systems, one also with a fibre coupled waveguide and another one with a newly developed laser diode, were tested on their suitability for a mobile setup.

3.2.1 Fully Fibre Integrated Waveguide Frequency Doubling

For the requirements of a mobile system I have designed and built a frequency doubling system using a waveguide in a PPKTP crystal with attached fibres at both ends. The setup allows for a very robust, stable and compact system, which does not require any realignment.

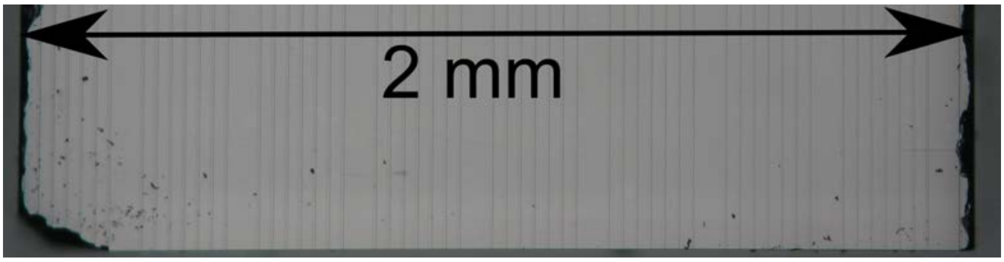

FIGURE 3.6: View of the PPKTP waveguide crystal showing the waveguides near an edge

Due to the quadratic dependence on intensity of frequency doubling in crystals such as KTP(see section 3.3.1), high fundamental intensities are required to achieve good conversion efficiencies. An effective way to achieve such constant high intensities is the use of waveguides. Stress centres are burned into crystal using a pulsed femto-second laser. The stress causes a change in the refractive index, allowing the light to be guided along the waveguide. The fundamental and frequency doubled light is guided in a 4 μm wide channel. As can be seen in figure 3.6 our PPKTP crystal has 8x7 waveguides written in it, allowing us to choose the one with the best efficiency.

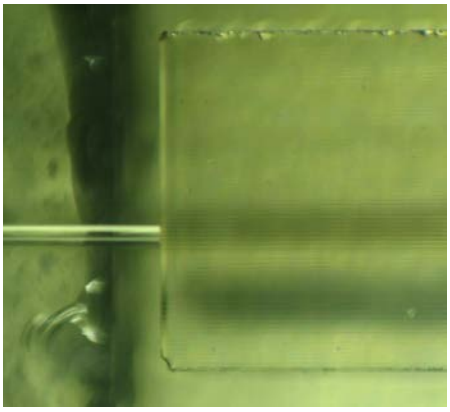

FIGURE 3.7: The PPKTP waveguide crystal with the attached input fibre

The crystal has fibres attached to the input and output, which do not require any realignment after the initial glueing. The high intensities of the light in the transition between fibre and waveguide made it necessary to develop a special glueing technique, which firmly attaches the fibres without creeping between fibre and crystal. A poly methyl methacrylate (PMMA) based glue was used. In the glueing process the glue was heated, making it viscous enough to creep around the contact point, but not viscous enough to creep between fibre and crystal. For efficient coupling between fibres and waveguide the mode field diameters are matched. Further information on the glueing process, the testing of different glues, fibre mode matching and the attachment of the input fibre can be found in my diploma thesis [89].

The main limitation of this system is the power intensity in the waveguide. Any defect in the crystal, such as F-Centres, cause an absorption of the light leading to the destruction of the waveguide if the power is too high.

A blue power of up to 15 mW was achieved with this setup, giving enough power for auxiliary tasks such as spectroscopy. But this is not enough to operate the 2D-MOT, with its high power requirements (see section 2.2.1). Further advancements in the process of writing the waveguides or different types of crystal might allow for higher powers in the future. Combining potential future higher output powers with the use of several waveguides operated in parallel might allow for a system with sufficient power in the future.

3.2.2 Commercial Fibre Coupled Waveguide Frequency Doubling

This commercial waveguide system from NTT has a waveguide crystal for frequency doubling. The input coupling to the waveguide from a polarization maintaining fibre is integrated into the housing. The output of the waveguide is in free space and needs to be coupled into a fibre if required. The housing also has a temperature control included.

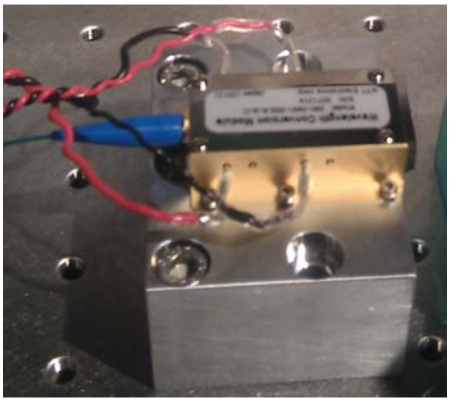

FIGURE 3.8: Commercial fibre coupled frequency doubler from NTT

This system is a compact and robust design, allowing up to 50 mW of blue light generation (manufacturer specification). During the initial testing it showed that this relatively new system still requires additional work for component stability. A drop in the output power by 2/3 was observed.

This system shows promising potential as it can deliver sufficient power to operate parts of the experiment, like the 3D-MOT, and is also very compact. But the power is not sufficient to optimally operate the 2D-MOT. Again having multiple systems in parallel might allow for a system with sufficient power.

3.2.3 Commercial Extended Cavity Diode Laser

Only recently laser diodes have become available at our required wavelength of 461 nm. This laser is the first known commercially available extended cavity diode laser for our required wavelength. It currently offers a power of up to 40 mW. Having laser diodes directly available greatly reduces the complexity and size of the laser setup.

The laser was tested as part of a fourth year project to design an alternative spectroscopy setup (see section 3.3.6). With the large mode-hop free tuning range of 25 GHz no working time was lost readjusting the laser. The laser also showed a very low drift, with the spectroscopy signal only occasionally being lost after a night.

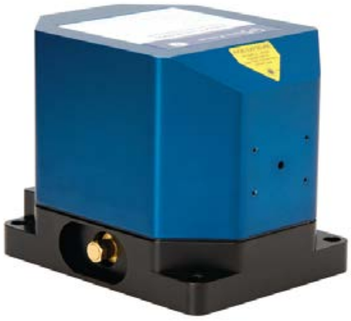

FIGURE 3.9: Newport tunable diode laser for 461 nm

To determine the linewidth the laser was beat with the cavity frequency doubling laser (section 3.2.4) by overlaying the two beams on a photo diode and measuring the width of the beat frequency on a spectrum analyser.

If the lasers have a similar linewidth the measured half width half maximum (HWHM) of the beat signal will be the linewidth of one laser. If one laser has a significantly larger linewidth that linewidth is resolved. Since both lasers are in an ECDL setup in Littrow configuration a similar linewidth is expected for both lasers. Both lasers were locked to the strontium transition, where the cavity doubled laser was offset 40 MHz from the transition by two AOMs. Additional frequency shifts between the lasers were due to an offset caused by the spectroscopy (see section 3.3.6). The beat measurement is shown in figure 3.10 with the centre frequency being at 56.6 MHz. The measurement was taken with a resolution of 200 kHz and being averaged over 500 measurement cycles. The peak at 10 MHz can be attributed to the modulation frequency of the Newport laser for the spectroscopy. The peak at 86 MHz is the doubled modulation frequency of the cavity doubled laser. The peak at 38 MHz is of unknown origin. The large central peak ranging from about 40 MHz to 80 MHz is the actual beat frequency of the two lasers. The central peak has a FWHM of less than 400 kHz. This is in good agreement with the quoted 200 kHz linewidth for the Newport laser, which suggests that the cavity doubled laser has a similar linewidth. But the central peak is only resolved by a single measurement point. If a Lorentzian is fitted to the data, as is shown in figure 3.10, a FWHM of 4.2 MHz is measured. Suggesting a linewidth of up to 4 MHz. This is considerably larger than the typical linewidth of an ECDL laser of <1 MHz [92]. Further investigations would be required to determine the actual linewidth of the laser. Due to the limited loan time of the laser, no additional beat measurements were taken to verify the accuracy of the data.

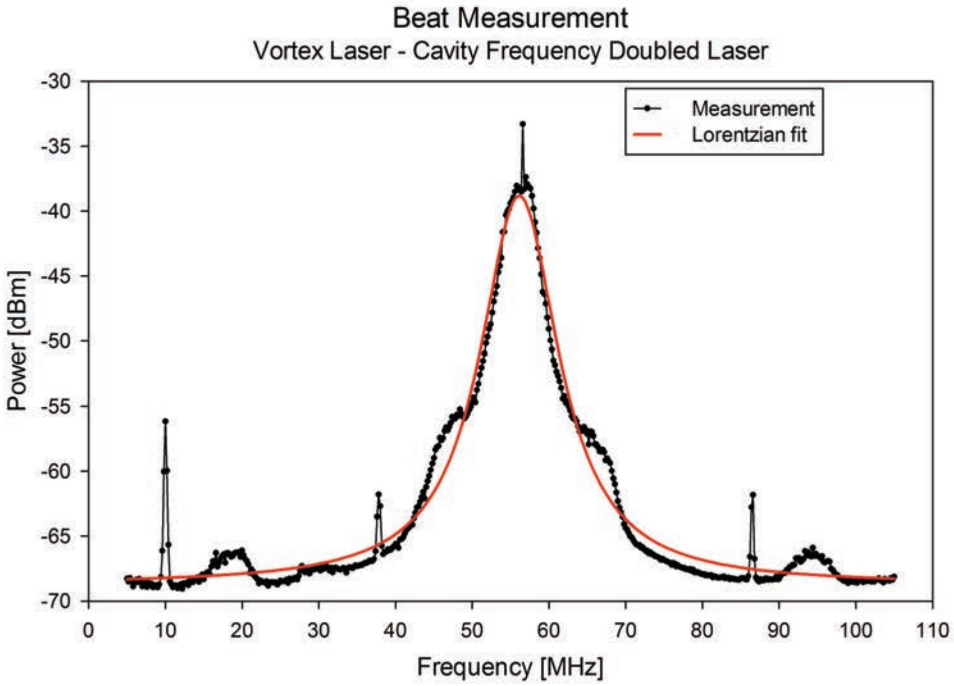

FIGURE 3.10: Beat measurement of the locked Newport and cavity frequency doubled laser. The peak at 10 MHz can be attributed to the modulation frequency of the Newport laser for the spectroscopy. The peak at 86 MHz is the doubled modulation frequency of the cavity doubled laser. The peak at 38 MHz is of unknown origin. The central peak has a FWHM of <400 kHz and the fitted Lorentzian has a FWHM of 4.2 MHz.

3.2.4 Monolithic Cavity Frequency Doubling

For the blue laser light generation I have designed and built a frequency doubling laser system which can produce up to 300 mW of blue light. This system uses a cavity to increase the intensity of the fundamental light for efficient conversion. A detailed description and evaluation of the system is given in section 3.3.

This system uses a monolithic cavity design to enable a more stable cavity and easier transportability. Most of the current cavity frequency doubling systems use mirrors to form the cavity. This allows for a quick and easy setup, but due to the many moveable parts, requires constant (typically weekly) readjustment. Our system has proven to be stable and even after months only a slight decay of the blue power is visible. With the robust design of the modules and cavity proving to be very stable this system is well suited to be transported.

3.2.5 Summary

Out of the four tested laser systems, currently only the cavity frequency doubled laser offers enough blue power to operate a strontium atomic optical clock with a 2D-MOT. Although other systems, especially the fully fibre integrated waveguide, would be more suitable for a mobile system, they currently cannot offer a sufficient amount of power. The biggest improvements are expected in the development of the laser diodes. The first diodes available two years ago had a power of 5 mW and have now reached 40 mW.

3.3 461 nm Laser

Laser cooling strontium requires laser light at a wavelength of 460.8 nm. Usually Ti-Sapphire lasers are frequency doubled in stationary experiments [93, 94], as these offer powers in the region of a few watts and have proven very reliable, but they are not easily transportable and expensive systems. Alternatively a MOPA (Master Oscillator Power Amplifier) system can be used. These systems can be built to be very robust and compact.

In section 3.3.1 the theoretical background for frequency doubling in a non linear crystal will be introduced. Section 3.3.2 will show the design and stability calculations for the cavity. And in section 3.3.5 the design of the final frequency doubling module will be shown. The operational characteristics will be discussed in section 3.3.5 and finally the spectroscopy on strontium for locking the laser will be shown in section 3.3.6.

3.3.1 Frequency Doubling Theory

Frequency doubling in a crystal is a non-linear phenomenon. It is non-linear in a sense that the response of the system behaves in a non-linear manner to the strength of the inducing light field. For example second-harmonic generation occurs as a result of the atomic response that scales quadratically with the applied optical field. Consequently, the intensity of the generated light has a square dependence on the intensity of the applied optical field.

In order to describe non-linear effects let us consider electromagnetic radiation passing through matter. The electric field will lead to a periodical polarization of the electrons in the material. At small intensities the polarization will be small and behave like a harmonic oscillator.

At low intensities or in linear optics the dipole moment per unit volume, the polarization $P(t)$, depends linearly on the electric field strength $E(t)$ [95]:

$$P(t) = \epsilon_0 \chi^{(1)} \cdot E(t) \tag{3.1}$$

Where $\chi^{(1)}$ is known as the linear susceptibility and ϵ_0 is the permittivity of free space. For larger field intensities or in non-linear optics, the optical response can be described by generalizing equation 3.1. The polarization can be expressed as a power series in the field strength:

$$P(t) = \epsilon_0 (\chi^{(1)} \cdot E(t) + \chi^{(2)} \cdot E^2(t) + \chi^{(3)} \cdot E^3(t) + \ldots) \tag{3.2}$$

Where $\chi^{(2)}$ and $\chi^{(3)}$ are known as second- and third-order non-linear optical susceptibilities, respectively.

The non-linear effects can be visualized by looking at the polarization of an atom. At small intensities the amplitude will be small and the potential of the retaining force can be approximated by a parabola. The retaining force is the derivative of its potential. At small amplitudes the force will grow linearly. For bigger amplitudes the potential cannot be approximated by a parabola any more, thus the retaining force will have non-linear components.

The propagation of light through non-linear media can be described by the wave equation. This can be deduced from Maxwell's equations:

$$\nabla \cdot \mathbf{D} = \rho \qquad (3.3) \qquad\qquad \nabla \times \mathbf{E} = -\frac{\partial \mathbf{B}}{\partial t} \qquad (3.5)$$

$$\nabla \cdot \mathbf{B} = 0 \qquad (3.4) \qquad\qquad \nabla \times \mathbf{H} = \frac{\partial \mathbf{D}}{\partial t} + \mathbf{J} \qquad (3.6)$$

Our primary focus is for solutions of the equation in regions of space containing no free charges:

$$\rho = 0$$

and also no currents:

$$\mathbf{J} = 0$$

We are also assuming non magnetic material:

$$\mathbf{H} = \frac{1}{\mu_0}\mathbf{B}$$

However we do need a non-linearity in the medium, in the sense that the fields **D** and **E** are related:

$$\mathbf{D} = \epsilon_0\mathbf{E} + \mathbf{P}$$

Now we can derive the optical wave equation in the usual manner. We take the curl of equation 3.5, interchange the order of the space and time derivative and use the simplifications resulting in:

$$\nabla^2\mathbf{E} - \mu_0\frac{\partial^2\mathbf{D}}{\partial t^2} = 0 \tag{3.7}$$

For simplification we can decompose the electrical displacement field into its linear and non-linear part:

$$\mathbf{D} = \epsilon_0\mathbf{E} + \mathbf{P} = \epsilon_0\mathbf{E} + \mathbf{P}^{(1)} + \mathbf{P}^{NL} = \mathbf{D}^{(1)} + \mathbf{P}^{NL}$$

where $\mathbf{D}^{(1)}$ and $\mathbf{P}^{NL}$ are the linear and non-linear part, respectively. In terms of these quantities the wave equation (eq 3.7) can be written as:

$$\nabla^2\mathbf{E} - \mu_0\frac{\partial^2\mathbf{D}^{(1)}}{\partial t^2} = \mu_0\frac{\partial^2\mathbf{P}^{NL}}{\partial t^2} \tag{3.8}$$

If we consider the case of a lossless, dispersionless medium, we can express the relation between $\mathbf{D}^{(1)}$ and $\mathbf{E}$ in terms of a real, frequency independent dielectric tensor $\boldsymbol{\epsilon}_r$:

$$\mathbf{D}^{(1)} = \epsilon_0 \boldsymbol{\epsilon}_r^{(1)} \mathbf{E} \tag{3.9}$$

In the case of an isotropic medium this relation reduces to:

$$\mathbf{D}^{(1)} = \epsilon_0 \epsilon_r^{(1)} \mathbf{E} \tag{3.10}$$

where $\epsilon_r^{(1)}$ is a scalar quantity and the dimensionless, relative permittivity. For the case of an isotropic, dispersionless material, the wave equation 3.8 becomes:

$$\nabla^2 \mathbf{E} - \frac{\epsilon_r^{(1)}}{c^2} \frac{\partial^2 \mathbf{D}^{(1)}}{\partial t^2} = \frac{1}{\epsilon_0 c^2} \frac{\partial^2 \mathbf{P}^{NL}}{\partial t^2} \tag{3.11}$$

using $c = \sqrt{\mu_0 \epsilon_0}$.

Equation 3.11 has the form of an inhomogeneous wave equation. The time dependent non-linear polarization term on the right hand side of the equation can be seen as a source for new components of the electromagnetic field. Without this term solutions to equation 3.11 would be plane waves in a medium with an index of refraction n.

In non-linear media a wide range of effects can be observed. Important examples are: frequency doubling (second harmonic), frequency tripling, sum- and difference-frequency generation, self focussing, etc.

The effect important to us is the second harmonic generation. To understand this effect we will look at the electrical field of the pump laser:

$$E(t) = E \cdot e^{i\omega t} + E^* \cdot e^{-i\omega t} \tag{3.12}$$

For a crystal with non negligible second-order non-linear optical susceptibilities $\chi^{(2)}$, the term relevant for second harmonic generation, the second order polarisation can be written as (using equation 3.2 & 3.12):

$$P^{(2)}(t) = \chi^{(2)} \cdot E^2(t)$$

$$P^{(2)}(t) = 2\chi^{(2)} E E^* + (\chi^{(2)} E^2 e^{-i2\omega t} + \chi^{(2)} E^2 e^{i2\omega t}) \tag{3.13}$$

As can be seen in equation 3.13 the second order polarization depends on a constant term and a term at the second harmonic frequency. Inserted into the wave equation 3.11, it can be seen that the second term in equation 3.13 generates an electro optical wave at the second harmonic frequency.

The fundamental and the second harmonic wave will have a certain phase relation in the crystal:

$$\Delta k = k_2 - 2k_1 \tag{3.14}$$

where k1 and k2 are the wavevectors of the fundamental and second-harmonic wave, respectively. For the generated wave to be able to extract energy most efficiently from the incident wave the phases of the two need to match, meaning $\Delta k = 0$. When this condition is fulfilled the generated wave maintains a fixed phase relation with respect to the non linear polarization and the amplitude of the second harmonic frequency grows linearly with the crystal length, and consequently the intensity grows quadratically.

For the wavevectors of both waves to match the refractive indices have to be the same:

$$n_{\omega} = n_{2\omega} \tag{3.15}$$

Since the condition 3.15 is usually not fulfilled in isotropic media, birefringent media are usually used to achieve this phase matching. This uses the property of them having different refractive indices for different crystal axis. In combination with the fact that the second harmonic wave is emitted orthogonally to the fundamental wave phase matching can be achieved.

There are three common possibilities to achieve phase matching:

- **critical phase matching:** In this case the crystal axis is chosen in such a way, that the refractive indices for both beams are the same.
- **non critical phase matching:** Since the refractive index changes differently with temperature for both beams, the crystals temperature is adjusted to a point, where both refractive indices are the same. Temperatures of a few hundred degrees are typically required.
- **periodically poled crystals:** In these crystals the ferroelectric effect is being used. By applying an electric field, the spontaneous polarization d_{eff} can be changed. If the electric field is applied at a period of twice the coherence length a quasi phase matching is achieved. Then, when the field amplitude of the second harmonic wave is about to begin to decrease due to the wavevector mismatch, the sign of d_{eff} is reversed and the field amplitude begins to grow monotonically.

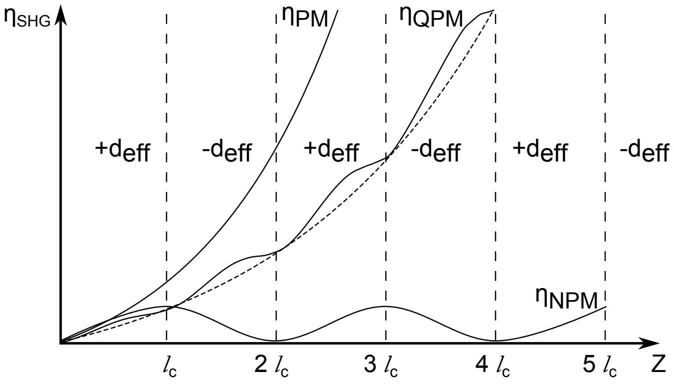

FIGURE 3.11: Example diagram of conversion efficiency for phase matching η_{PM}, quasi phase matching η_{QPM} and no phase matching η_{NPM} in a non-linear crystal. Image reproduced from [96].

At quasi phase matching it is possible to have a positive energy flow from the pump- to the signal-wave throughout the entire crystal, although condition 3.15 is not fulfilled. When the phase difference between the pump- to the signal-wave is lower than 180°, there is a positive energy flow. Above 180° the energy is transferred back to the pump-wave. The length in which a phase difference between the waves is reached is called the coherence length l_c. At a periodic poling of the crystal at the coherence length, a constant energy transfer into the signal-wave is achieved. A schematic intensity characteristic of the signal-wave in a phase matched, quasi phase matched and non phase matched crystal is shown in figure 3.11. Further advantages of quasi phase matching are that the crystal axes with the largest conversion factor can be chosen and that no high temperatures are being required.

Using equations 3.11 and 3.13 the expected conversion efficiency in a non linear crystal can be calculated. A full discussion of the derivation can be found in [95]. I shall present the derived formulae for the conversion of the fundamental power to the second harmonic power along the crystal.

The amplitudes of the fundamental u_1 and second harmonic u_2 wave along the crystal for optimum phase matching is given by:

$$u_1(\zeta) = \mathrm{sech}(\zeta) \qquad (3.16) \qquad\qquad u_2(\zeta) = \tanh(\zeta) \qquad (3.17)$$

With ζ being a normalized distance parameter, defined as follows:

$$\zeta = \frac{z}{l} \tag{3.18}$$

With z being the position along the crystal and l is the characteristic distance over which the fields exchange energy. For the case in which only the fundamental field is present at z=0, which is true for our frequency doubling, the length parameter l is given by:

$$l = \frac{\sqrt{n_1 n_2}\lambda_1}{4\pi d_{eff}\left|A_1(0)\right|} \tag{3.19}$$

With $A_1(0)$ being the field amplitude, which can be brought into relation with the intensity as follows:

$$I_1 = \frac{P}{\pi\omega_0^2} = 2n_1\epsilon_0 c A_1^2 \tag{3.20}$$

Where P is the power of the pump beam and ω_0 is the waist of the beam in the centre of the crystal. Here we are assuming a constant intensity distribution of the beam and a non diverging beam. Combining equations 3.18 to 3.20 the normalized distance parameter ζ can be written as:

$$\zeta = \frac{2d_{eff}L}{n_1\lambda\omega_0} \cdot \sqrt{\frac{2\pi P}{n_2\epsilon_0 c}} \tag{3.21}$$

We can now define the conversion efficiency η as the power in the second harmonic beam, as defined in equation 3.17, at the end of the crystal divided by the power of the fundamental beam, as defined in equation 3.16, at the beginning of the crystal.

$$\eta = \frac{u_2^2(L)}{u_1^2(0)} \tag{3.22}$$

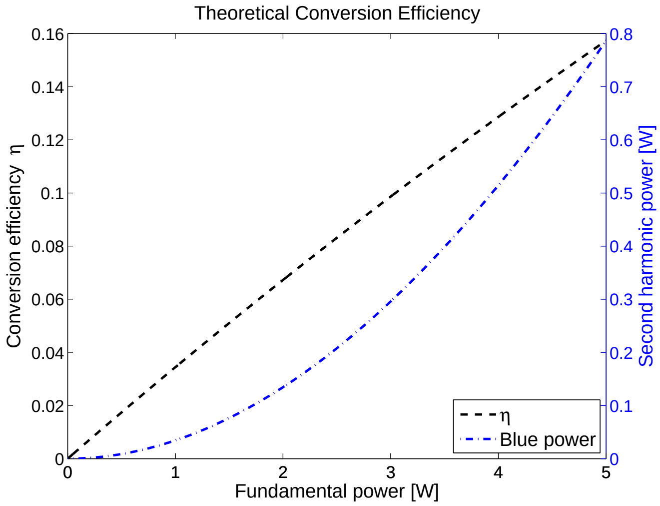

FIGURE 3.12: Theoretical conversion efficiency

Figure 3.12 shows an estimate of the conversion efficiency for the crystal used in this experiment and the expected frequency doubled power. As parameters the following values were used: for the crystal length L=20 mm, the refractive indices for potassium titanyl phosphate (KTP) are $n_{z,922nm}$=1.836 and $n_{z,461nm}$=1.918, the waist ω_0=42 μm and the effective non-linear coefficient for KTP was taken from [97] to be $d_{eff} = 9.5 \cdot 10^{-12}$. In first order approximation the conversion efficiency will increase linearly with the fundamental power, leading to a quadratic dependence of the second harmonic power. The low single pass efficiency and the quadratic dependence show the need for a cavity to gain good conversion efficiencies. The estimation presented here can only be seen as an approximation of the expected conversion efficiencies, due to the assumptions of an optimum phase matching, constant beam intensity and non diverging beam taken here.

3.3.2 Cavity Design

As can be seen in equation 3.13 in section 3.3.1 the conversion efficiency depends quadratically on the fundamental power. Since most of the pump is not converted in a single pass the pump power needs to be recycled for good conversion efficiencies. This can be achieved by placing the doubling crystal in a cavity.

For the design of a cavity two characteristics play an important role: the waist of the beam in the centre of the frequency doubling crystal and the transmission of the input coupling mirror. Boyd and Kleinman [98] have considered how to optimally adjust the focus of the incident laser beam to maximize second-harmonic conversion efficiency. They find that the highest efficiency is obtained when the incident laser beam is focussed at the centre of the crystal and L/b, a dimensionless longitudinal coordinate, describing the ratio of the crystal length L to the confocal parameter b, is equal to 2.84, with the confocal parameter b being:

$$b = \frac{2\pi\omega_0^2}{\lambda/n} \tag{3.23}$$

Following the proven design from [97] with a similar frequency doubling system the same 20 mm long PPKTP crystal was chosen. With a fundamental wavelength of 921.7 nm and the refractive index $n_{z,921.7}$ =1.836, the optimum waist can be calculated as ω_0^{opt} =23.6μm, which is independent of the incident power. At the expected second harmonic power levels of hundreds of milliwatts thermal lensing was found to be a serious issue in a KTP crystal [99, 100], with the main limitation on their power scaling were strong thermal lensing effects due to blue absorption. This strong limitation arose from the tight focussing used in the cited esperiments (with ω_0 =17 μm, being their optimum focussing) and the associated thermal lens power scaling as ω_0^{-2} [100]. To avoid thermal lensing issues and following calculations in [97] a larger waist of nearly double the optimum of ω_0 =43 μm was chosen, which still achieves nearly optimum conversion efficiency but only a quarter of the thermal lensing effects are expected.

The other important parameter is the transmission of the input coupling mirror T_1. The power coupled into the cavity needs to match the losses, mainly due to the frequency conversion, in the cavity. Considering the internal circulation fundamental power P_c in the cavity at zero cavity detuning [97, 101, 102]:

$$\frac{P_c}{P_\omega^{in}} = \frac{T_1}{[1 - \sqrt{(1-T_1)(1-\varepsilon)(1-\Gamma P_c)}]^2} \tag{3.24}$$

Where ϵ is the distributed round-trip fractional loss (excluding T_1) and Γ, expressed in W^{-1}, is the depletion due to non linear effects. With Γ, which depends on the crystal length and the focussing, ϵ ,and the maximum available mode matched power P_ω^{in} given, equation 3.24 can be optimized against T_1:

$$T_1^{opt} = \frac{\epsilon}{2} + \sqrt{\left(\frac{\epsilon}{2}\right)^2 + \Gamma P_\omega^{in}} \tag{3.25}$$

Since the values for ϵ and Γ were not experimentally available while designing the cavity, values from a very similar cavity design from [97] were taken to estimate the required transmission T_1 for our setup. The reported values were ϵ =0.02 and Γ =0.023 W^{-1}. With an available non mode matched power of 1.2 W (see section 3.3.4) and using the measured coupling efficiency of 50-60% of a Tapered Amplifier into a fibre, which is expected to be similar to the coupling into the cavity, to estimate the mode matched power available to P_ω^{in}=0.6 W. Using these values and equation 3.25 the optimum transmission of the input coupling mirror can be estimated to T_1^{opt}=12.8%.

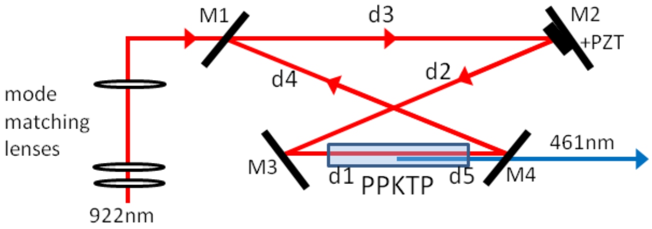

FIGURE 3.13: Schematic overview of the cavity setup. Mode matching is done via a two lens telescope and a focusing lens. Mirror M2 is mounted on a ring high voltage PZT.

A schematic of the cavity in bow tie setup can be seen in figure 3.13. The mirrors M1 and M2 are plane mirrors and M3 and M4 have a radius of curvature of R=75 mm. The beam waists are ω_0 =43 μm and ω_0 =161 μm in the crystal and at position d3 respectively. The folding angle of the ring resonator was chosen 11°, giving a negligible astigmatism introduced by the two off axis curved mirrors M3 and M4. All mirrors have an anti-reflex coating for 461 nm and 922 nm on the outside. Mirrors M2 through M4 have an anti-reflex coating for 461 nm and a high reflectivity coating for 922 nm on the inside where as mirror M1 has an anti-reflex coating for 461 nm and a measured transmission of T_1=15.5% for 922 nm. Due to production uncertainties the transmission is not at T_1^{opt}.

As the experiment is aimed at being transportable, a cavity design was devised, which would be able to withstand a transport without causing major readjustment efforts. Typically stable mirror mounts are used to keep the alignment of the cavity. Since these setups require between weekly and monthly realignment, a more stable setup was required. A monolithic cavity was designed, which would not require readjustment of the cavity mirrors. The mirrors were glued[2] onto the aluminium uni-body. To allow for

---

[2] JB-Weld

initial alignment the mirrors M3 and M4 were suspended by a translation stage. The translation of the curved mirrors along the surface of the cavity body corresponds to a tilt of the mirror, thus allowing a stable cavity mode to be seen before the final glueing of these mirrors. With the combination of a monolithic cavity and glued mirrors I was able to significantly reduce the frequency of readjustment of the input beam to regain the power to once a month or less.

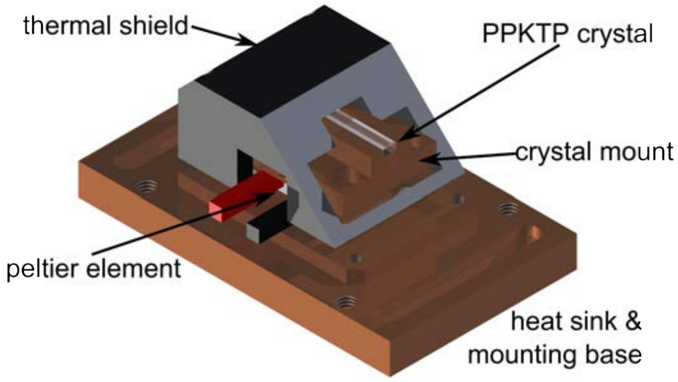

FIGURE 3.14: Rendered image of the crystal mount. The plastic shielding is cut for better visibility.

To allow for a small cavity size for easier portability a radius of curvature for mirrors M3 and M4 of r=75 cm was chosen. A cavity length of 404mm was calculated to be stable for these mirrors (see section Stability Calculations).

To house the crystal a special mount was designed. This mount needs to fulfil a range of requirements:

- The crystal needs to be uniformly heated to temperatures up to 40°C
- A good thermal contact between crystal and mount is required to allow quick temperature adjustments
- The heating should be limited to only the crystal and not the surrounding cavity

- The crystal needs to be adjustable along the x- and y-axis as well as tilted along these axes

An image of the crystal mount fulfilling all of the above requirements is shown in figure 3.14. The crystal is placed in a groove 0.1 mm wider than the crystal and contacted to the copper mount using thermal paste[3]. The temperature is controlled via a Peltier element. A plastic shield (black in the image) with an aperture of 3 mm on either side thermally insulates the crystal. The larger copper heat sink is screwed into the cavity with four adjustable screws and four locking screws, allowing for spatial adjustment.

Stability Calculations

Only a certain range of distances between the curved mirrors for a given radius of curvature produce a stable cavity. This section will show how a stable combination of cavity size and mirror curvature for the required beam waist of about 45 μm was found. The stability of a cavity can be calculated by using ray transfer matrix analysis. This method uses ABCD-matrices to calculate whether the beam is being kept in the cavity or is diverging.

For the bow tie cavity the matrix will be constructed in single steps. The three matrices we need for this are:

$$M_p = \begin{pmatrix} 1 & 0 \\ 0 & 1 \end{pmatrix} \quad (3.26) \qquad \text{Matrix for a plane mirror}$$

$$M_r(r) = \begin{pmatrix} 1 & 0 \\ -2/r & 1 \end{pmatrix} \quad (3.27) \qquad \text{Matrix for spherical mirror}$$

---

[3] Arctic Silver

$$T_d(d) = \begin{pmatrix} 1 & d \\ 0 & 1 \end{pmatrix} \qquad (3.28)$$

Matrix for the translation of a beam

Beginning in the centre of the crystal and going once around the bow tie cavity the ABCD-matrix can be constructed (see figure 3.13 for explanation of variables):

$$\mathbf{M} = T(d_1) \cdot M_r(r_1) \cdot T(d_2) \cdot M_p \cdot T(d_3) \cdot M_p \cdot T(d_4) \cdot M_r(r_2) \cdot T(d_5) \qquad (3.29)$$

Matrix **M** describes the propagation of the light in the cavity. It can also be seen as a series of thin lenses with focal length f=r/2 separated by the equivalent distance of the cavity, which is known as the lens equivalent waveguide. Using ray transfer matrix analysis the stability of the waveguide can be calculated. We need to find the light rays travelling through the cavity or waveguide which will periodically refocus. Meaning under what condition is the output of a section equal to the input multiplied by a constant λ. With $\begin{pmatrix} x_1 \\ \theta_1 \end{pmatrix}$ representing the vector at the beginning of a period and $\begin{pmatrix} x_2 \\ \theta_2 \end{pmatrix}$ the exit vector:

$$\mathbf{M} \begin{pmatrix} x_1 \\ \theta_1 \end{pmatrix} = \begin{pmatrix} x_2 \\ \theta_2 \end{pmatrix} = \lambda \begin{pmatrix} x_1 \\ \theta_1 \end{pmatrix} \qquad (3.30)$$

Which is nothing else than an eigenvalue equation:

$$[\mathbf{M} - \lambda \mathbf{I}] \begin{pmatrix} x_1 \\ \theta_1 \end{pmatrix} = 0 \qquad (3.31)$$

where **I** is the 2x2 identity matrix. Using the usual process of solving the eigenvalue equation with det$[\mathbf{M} - \lambda\mathbf{I} = 0]$ leads to the characteristic eigenvalue equation

$$\lambda^2 - 2g\lambda + 1 = 0 \tag{3.32}$$

With the substitution being our stability parameter:

$$g \overset{def}{\equiv} \frac{tr(\mathbf{M})}{2} \tag{3.33}$$

For the eigenvalues we find:

$$\lambda = g \pm \sqrt{g^2 - 1} \tag{3.34}$$

Now if we consider a ray after N passes through the system:

$$\begin{pmatrix} x_N \\ \theta_N \end{pmatrix} = \lambda^N \begin{pmatrix} x_1 \\ \theta_1 \end{pmatrix} \tag{3.35}$$

For the cavity to be stable no light ray should deviate far from the axis, which means that λ^N should not grow without limit. If we assume that $g^2 > 1$ then both eigenvalues are real. And since $\lambda_+\lambda_- = 1$, one of them has to be bigger than 1. This would imply that the ray corresponding to that eigenvalue would not converge. Therefore $g^2 < 1$ is required for a stable cavity, implying that λ has to have an imaginary part.

With the portability in mind a radius of curvature of R=-75 mm was chosen, leading to a smaller cavity size than the chosen R=-100 mm for a similar cavity [97]. For the smaller cavity we expect less misalignment due to external factors like temperature changes. With a folding angle of 11°, only a negligible astigmatism is expected. The distance between the curved mirrors is 90 mm and 110 mm between the flat mirrors. The cavity has a total length of 404 mm. For the designed cavity we get a stability parameter of $|g|$=0.274, thus the cavity is stable.

3.3.3 Master Laser

The Master Laser delivers the seeding light for the Tapered Amplifier (see section 3.3.4). The design of this laser is based on a similar design from my diploma thesis [89]. A 922 nm anti-reflex coated laser diode[4] is used in an external cavity diode laser setup (ECDL) in Littrow [90] configuration. The grating used has 1200 lines/mm and a reflectivity of 20-30%. The cavity has a length of 3.5 cm. The beam is passed through two optical isolators with an isolation of 38 dB each. Two isolators are used to suppress any standing waves competing with the cavity mode and causing instabilities. With only one isolator experience has shown that this might not be enough to fully suppress instabilities.

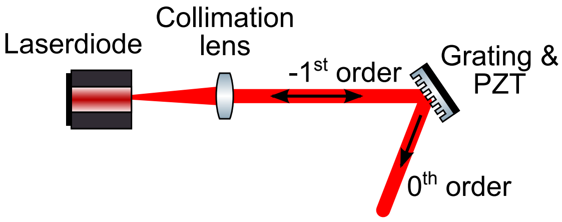

FIGURE 3.15: Schematic setup of an extended cavity diode laser (ECDL) in Littrow configuration

The Littrow configuration uses a grating as a wavelength selection and to form the laser resonator, as can be seen in figure 3.15. Depending on the angle of the grating different

---

[4] Eagleyard EYP-RWE-0980

wavelengths are reflected back into the laser diode via the minus first order. The light is coupled out of the resonator via the zero order reflection.

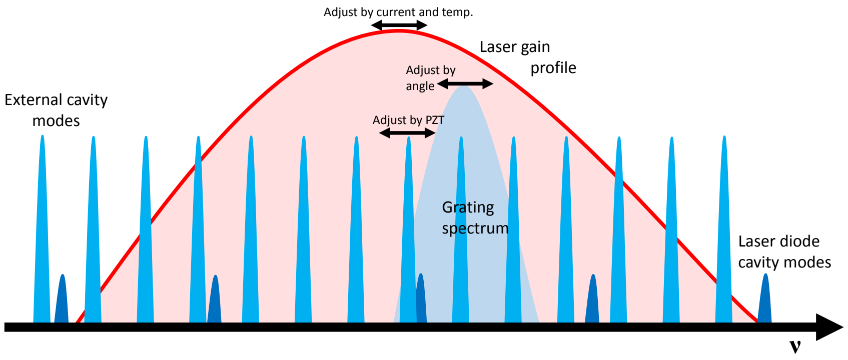

FIGURE 3.16: Illustration of competing modes in a laser cavity. Showing the overall gain profile of the laser diode,the spectrum of the grating, the wide spaced modes of the external cavity and the modes of a non anti reflex coated laser diode

The grating can be shifted via a piezoelectric transducer (PZT) on which it's mounted, allowing for changes in the resonator length. By combining the gain profile of the laser diode crystal with the wavelength selection of the grating, the resonator mode with the highest gain can be found, as illustrated in figure 3.16. This mode will be amplified the most and suppress any other modes, thus define the frequency at which the laser is emitting. The crystals of laser diodes built for extended cavity operation typically have an anti reflection coating, to prevent additional competing modes. A non anti-reflex coated crystal would act as a resonator itself, due to the reflectivity of the output facet. These additional modes cause an unstable operation, with the combined modes of both resonators, with the most amplification, not necessarily being at the desired frequency.

The lasing threshold for this diode is at 18 mA. At the recommended operational current of 100 mA a power of 34 mW is achieved.

After the isolators the light is coupled into a polarization maintaining optical fibre. Up to 65% coupling efficiency is achieved. At the typical operational current of 50-60 mA a power of 9 mW is available after the fibre. As this is not sufficient to fully seed the

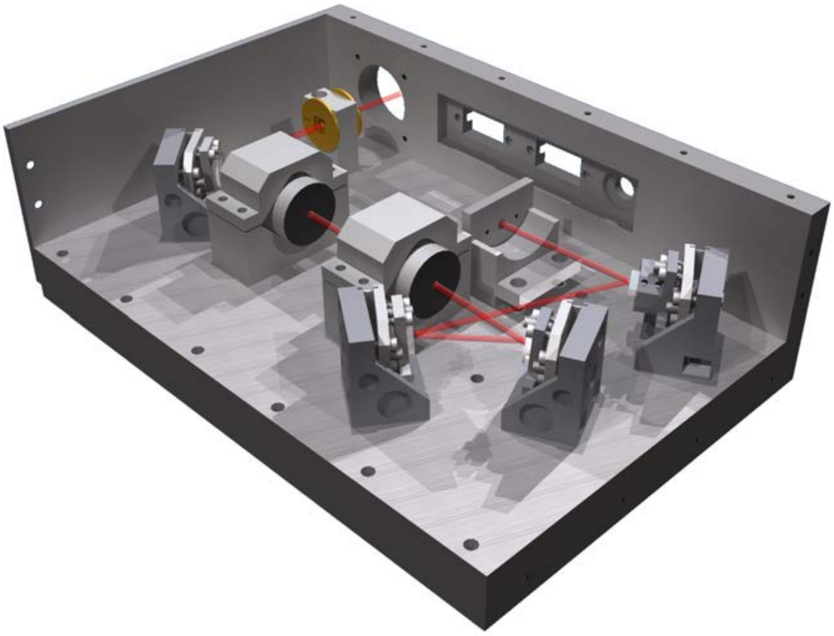

FIGURE 3.17: Schematic overview of master laser module. The laser beam originates from the laser diode, then gets diffracted from the grating, gets passed through two optical isolators and then gets coupled into a fibre.

tapered amplifier an additional amplifier module is inserted (see section 3.3.4) to amplify the power to the required 50 mW.

A currently still not explained effect can be seen when light is coupled into the frequency doubling cavity. A cavity mode is only forming in small bands of operational current for the laser diode (typically between 50-60 mA and 120-125 mA and a few 2 mA wide regions in between). The suspected multi mode operation of the laser outside these current regions was checked and has proven to be false.

3.3.4 Pre Tapered Amplifier Module

In the Tapered Amplifier (TA) Module the seeding light from the master laser (see section 3.3.3) is amplified to seed the Tapered Amplifier of the frequency doubling module for maximum power. The light entering the module from a fibre is collimated to a beam diameter of 0.9 mm and coupled into the amplifier using a f=3.5 mm lens. A maximum output power of 600 mW is achieved, which is limited by the seeding power of the master laser.

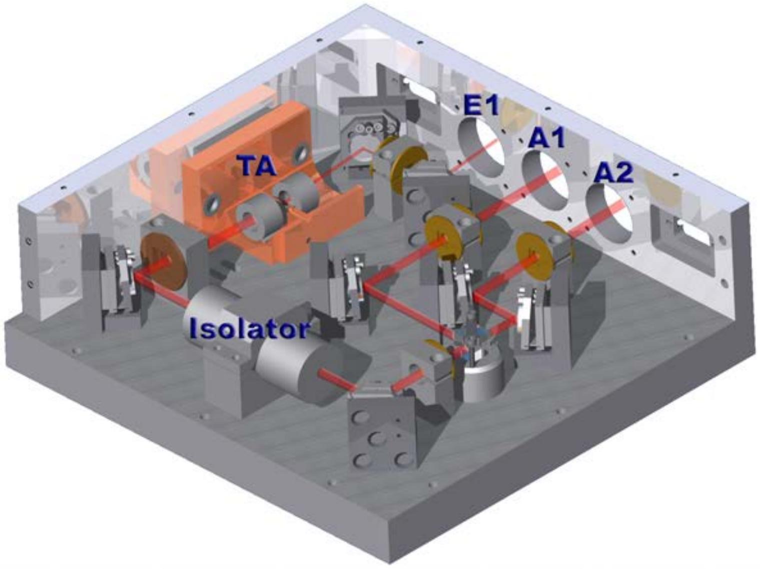

Figure 3.18: Schematic overview of Tapered Amplifier module. The seeding light enters the module at E1 and is coupled into the TA. An isolator afterwards prevents damage from reflection. The light is then coupled into two fibres.

Due to different divergence angles in the horizontal and vertical plane ($\Theta_{\shortparallel}$=14° and $\Theta_{\perp}$=28° FWHM) and an astigmatism of 600 μm two lenses are used to collimate the beam. Using an aspherical lens of f=2.75 mm and a cylindrical lens of f=40 mm the beam is collimated to a diameter of 3 mm. To prevent damage to the Tapered Amplifier from reflected light, an optical isolator[5] with an isolation >35 dB is placed in the beam path.

After the isolator, the beam is split into two beams and coupled into polarization maintaining fibres. With a coupling efficiency of 50% typically 100 mW of light is needed to seed the following Tapered Amplifier with its maximum seeding power of 50 mW.

The plot in figure 3.19 shows the output power of the Tapered Amplifier for currents

---

[5] Newport ISO-04-850-LP

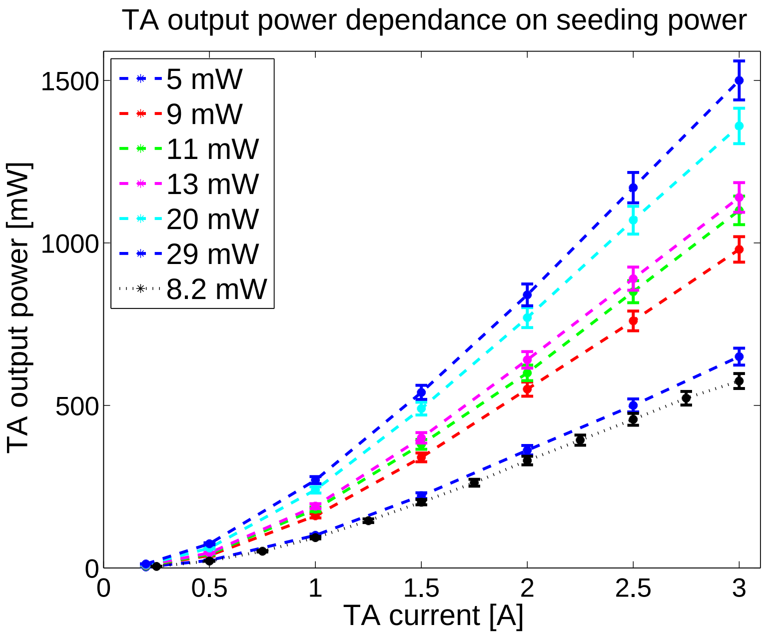

FIGURE 3.19: Output powers of tapered amplifier (TA) at initial installation for seeding powers between 5 mW - 29 mW. The data points with 8.2 mW seeding power were measured 4 years later. Errors are from the thermal power meter head uncertainty of 4%.

up to the recommended operational current of 3 A with seeding powers between 5 mW-29 mW. Also shown is the output power four years after initial installation for a similar seeding power of 8.2 mW. A decay in output efficiency after fours years of operation can

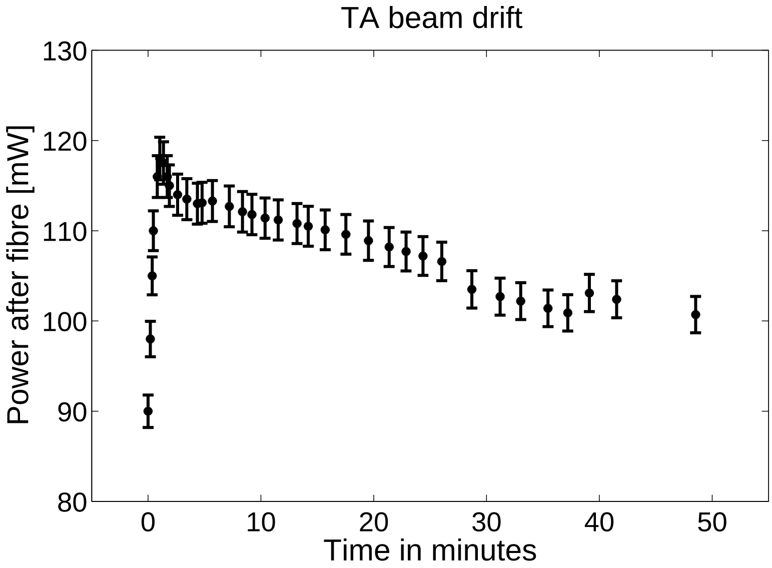

FIGURE 3.20: Power coupled into fibre from TA at 3 A for a time period of 45 min. Fibre coupling was optimized with TA at 1.5 A. The drop around 30 min is attributed to a mode hop of the laser during this time.

be seen. We expect that this is due to ageing of the crystal and misalignment of the lens glued directly in front of the TA due to creeping of the glue.

In figure 3.20 the power after fibre A1 is plotted against time. The Tapered Amplifier was operated a current of 3 A. The fibre coupling and the TA seeding were optimized at the typical operational current of 1.5 A. The maximum power is reached after one minute. Afterwards a steady decay of output power is visible. This decrease is caused by thermal drifts in the system. The outside wall will be heated by the peltier element of the TA. This non symmetric heating causes a thermal expansion of the material, which slightly moves the TA. The drop between minute 28 and 37 is due to a mode hop of the seeding laser during this time. This figure shows the importance of alignment of the system at the intended operational current and seeding power.

3.3.5 Frequency doubling module

The fibre from the Tapered Amplifier Module (see section 3.3.4) arrives at Input 1 as shown in figure 3.21. The beam is collimated with an f=7 mm lens to a diameter of 1.4 mm and coupled into the Tapered Amplifier (TA) using an f=3.1 mm lens. After the TA the beam is collimated using the same aspherical and cylindrical lens as in the Tapered Amplifier module (see section 3.3.4) and afterwards the diameter of the beam is adjusted using a two lens telescope (see Beam collimation and mode matching paragraph in this section). Preventing damage from reflections to the TA an optical isolator with >30 dB isolation is installed. To imprint side-bands onto the laser light, which are required to stabilize the cavity onto the laser light (see discussion on cavity operation in this section), an Electro-Optical-Modulator (EOM) was installed. In the current setup the current of the laser diode is directly modulated to imprint the sidebands, avoiding loosing 5-10% of the optical power by going through the EOM with an anti-reflection coating for 780 nm. The beam is then focused into the cavity by a lens. The last two mirrors before the cavity are mounted on commercial mirror mounts[6], allowing an easier and more precise alignment of the beam into the cavity.

The cavity itself is mounted on a peltier element to allow for temperature stabilisation of the cavity. The temperature stabilisation is not yet active, since thermal observed drifts are either negligible or compensated by the locking electronics. The 461 nm output of the cavity is split into two beams and coupled into fibres at outputs 1 and 2.

Beam collimation and mode matching

To collimate the beam of the TA module, the same aspheric and cylindrical lenses as described in section 3.3.4 were used. The beam was collimated at the predicted operational current of 2.5 A. The collimation was done at the operational current to account for the mode of the TA changing shape at different currents, as can be seen in figure 3.22. In these figures the mode of the beam at 2.75 A is clearly not Gaussian. The line of beams above the central beam are caused by diffraction of the aspheric lens after the TA. The beam leaving the TA was not completely horizontal and thus the lens had to be placed slightly off centred. Since the lens is only marginally larger than the beam, this diffraction pattern is visible.

For coupling into the cavity a two lens telescope and a focussing lens are used. The telescope reduces the waist of the beam from $\omega_{0||}$=840 μm and $\omega_{0\perp}$ >1360 μm to 440 μm and 1120 μm respectively. The theoretical modelling of the cavity suggests a beam waist of ω_0=41 μ m in the crystal and ω_0=162 μ m as a second waist. To check for consistency with the experiment the beam waist behind mirror M2 was measured. It was measured to be between ω_0=162 μm and 170μm. The different values arise from

---

[6] Radient dyes MNI

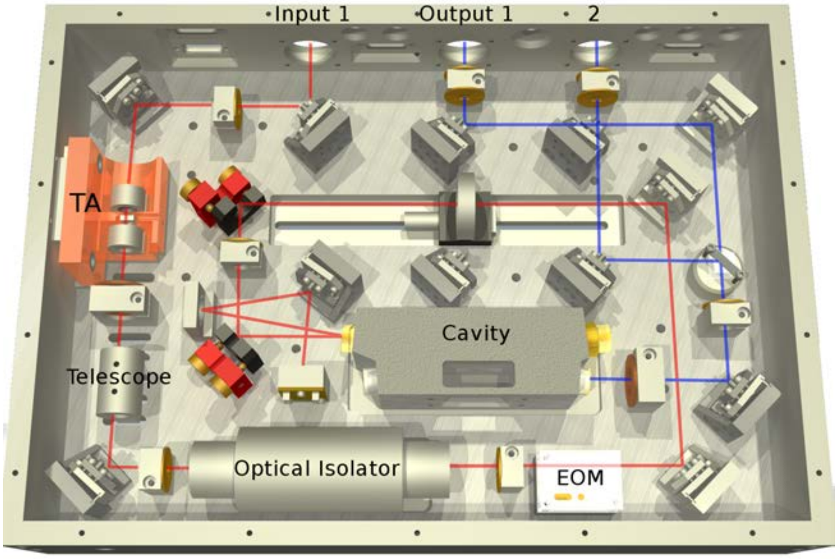

(a) Schematic overview of the frequency doubling module

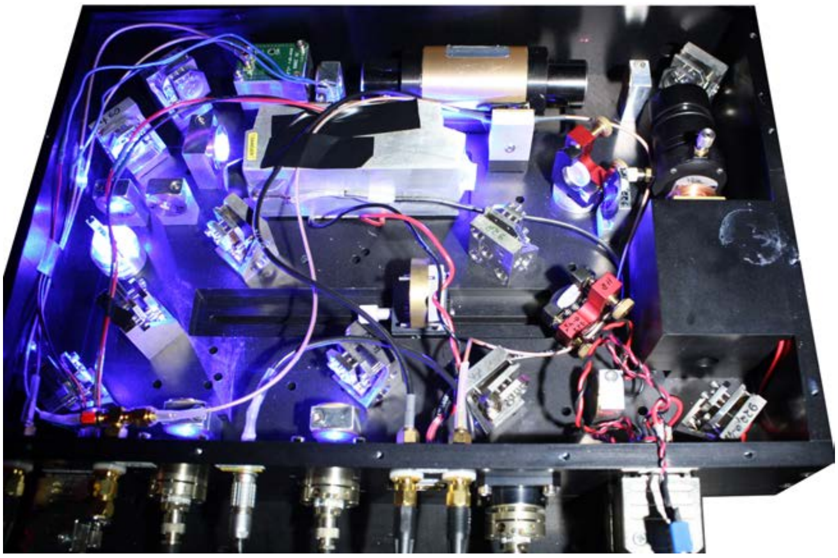

(b) Photograph of the frequency doubling module with operational frequency doubling

FIGURE 3.21: Schematic and photograph of the frequency doubling module. The module is turned 180° for the second image.

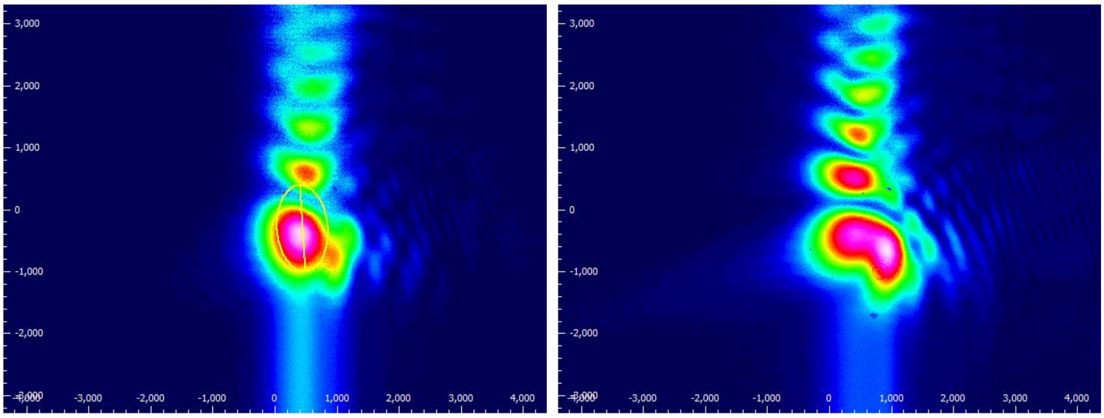

(a) TA current at 2.25 A

(b) TA current at 2.75 A

FIGURE 3.22: Beam profile of Tapered Amplifier after the isolator for 2.25 A and 2.75 A current.

different beam expansion in the parallel and perpendicular plane, caused by a slight astigmatism introduced from the curved mirrors M3 and M4. The measured beam waist is in good agreement with the simulated value.

Cavity operation

For a stable continuous wave operation of the cavity an active electronic servo control was installed. Mirror M2 is fitted on a piezoelectric actuator[7] (PZT) to control the length of the cavity. The Pound Drever Hall [103] locking technique was preferred over the Hänsch-Couillaud method, which was reported to fail when thermal effects arise [99, 104].

The current of the 922 nm laser diode is modulated at a frequency of 45 MHz to impose the required sidebands onto the laser, as can be seen in the schematic setup of the locking electronics in figure 3.23. To be able to resolve the sidebands of the cavity resonances, the sidebands should be further apart than the resonance width. With a FWHM of the resonance of 17.6 MHz (see further below) a modulation frequency of 45 MHz was

---

[7] PI P-820.10, 15 μm travel, 50/10 N push-/pull-force

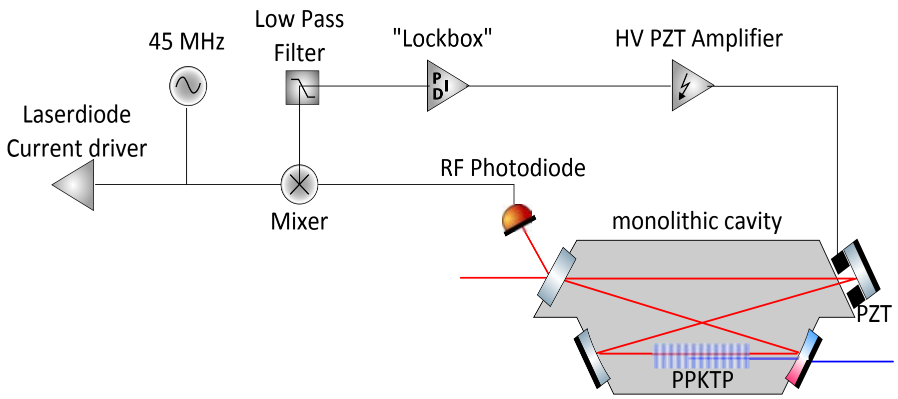

FIGURE 3.23: Schematic overview of electronic setup for locking the cavity

chosen. This large value is due to compatibility reasons with the locking electronics for the strontium spectroscopy (see section 3.3.6), where a modulation frequency of 45 MHz was implemented.

In the frequency doubling module, an EOM crystal can also be installed. Since no amplitude modulations from the direct modulation of the laser were visible when switching between the methods, the direct modulation is preferred, due to a loss of 5-10% of the light in the EOM. The cavity features are being picked up by a RF-photodiode, which is placed in the reflected beam of the input mirror. This signal is demodulated in the mixer and an error signal is produced. A low pass filter of 2.5 MHz filters any residual amplitude from the modulation signal. The servo signal produced in the PID-controller from the error signal is amplified in the HV PZT amplifier and fed to the PZT correcting for any phase changes. All electronics used were designed, tested and built within our research group.

With the final cavity dimensions yielding a cavity length of 404 mm (see section 3.3.2), the frequency spacing of the cavity's axial resonator modes, the free spectral range (FSR), can be calculated as:

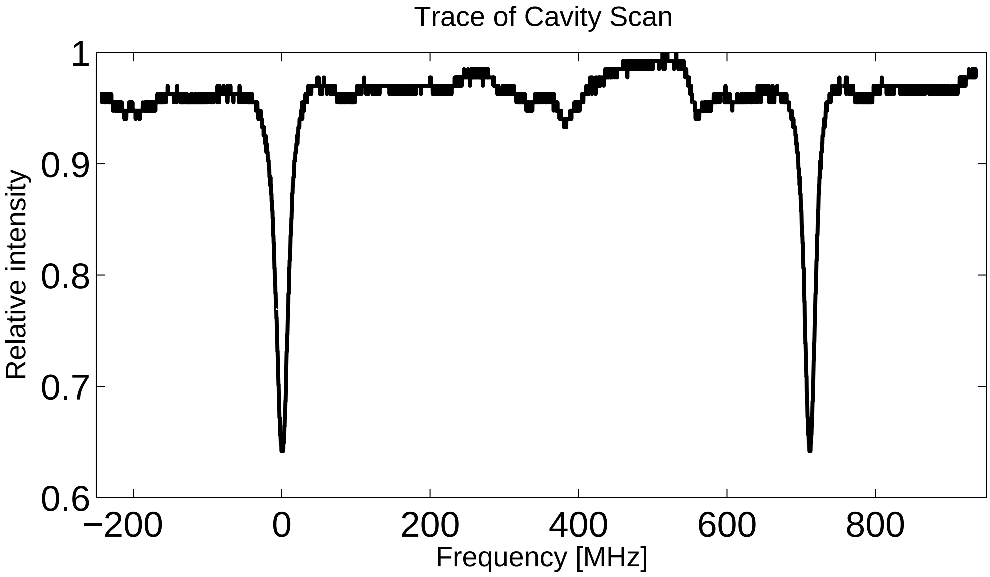

FIGURE 3.24: Scan of the intensity of the reflected light over two cavity resonances. X-axis is calibrated using the known free spectral range (FSR) of 712 MHz

$$FSR = \frac{c}{d} \tag{3.36}$$

Where c is the speed of light and d is the round trip length of the cavity. This yields a free spectral range of FSR=0.742 GHz in the absence of the crystal. If the crystal is installed in the cavity, the round trip length has to be altered accordingly:

$$FSR_{KTP} = \frac{c}{d + (n_{KTP} - 1) \cdot l} \tag{3.37}$$

Where n_{KTP} is the refractive index of KTP along the direction of light propagation and l is the length of the crystal. In our case l=20 mm and $n_{KTP,z,922}$=1.84, which gives a free spectral range of FSR=0.712 GHz with negligible errors due to very precise machining of the length.

The finesse of a cavity is defined as the free spectral range divided by the FWHM bandwidth of its resonances. It is fully determined by the resonator losses and is independent of the resonator length. The finesse can be calculated using the following formula:

$$F = \frac{\pi}{2arcsin\left(\frac{1-\sqrt{\rho}}{2\sqrt[4]{\rho}}\right)} \approx \frac{\pi}{1-\sqrt{\rho}} \tag{3.38}$$

Where ρ is the fraction of the circulating power remaining after one round trip with no incident light from outside the resonator. With a measured transmission for mirror M2 of 15.5±0.6 % and assuming the losses of the other mirrors are negligible a finesse of F=39±1.6 is calculated in the absence of second harmonic conversion. The finesse was measured in the cavity by tuning the temperature of the crystal far away from QPM temperature. The trace of a cavity scan was recorded and the FWHM of a resonance was measured to 17.6±0.7 MHz (see figure 3.24, main error contributions from the determination of the maximum ±3% and the width ±2%). The measured finesse of F_{exp}=40.5±1.7 is in good agreement with the predicted result of F=39±1.6.

Second Harmonic Generation

During the operation of the cavity a peak output power of 300 mW at 461 nm was achieved with a system conversion efficiency (non mode matched input power over blue output power) of 25%. Previous adjustment settings only yielded a power of 140 mW, with a careful readjustment of the telescope the higher powers were achieved. As can be seen in figure 3.25 the system conversion efficiency reaches its maximum of 30% between 450 mW and 800 mW of input power. From theoretical considerations (see section 3.3.1) the conversion efficiency should increase linearly with the fundamental power in the crystal. A nearly linear increase can be seen for the first measurement points between 200 mW and 450 mW input power, but it does not seem to pass through the origin as would be expected. Further measurements at lower input powers would be required to further investigate the trend towards the origin of the conversion efficiency. As the input power increases the conversion efficiency rise becomes less, reaching a stable value of 30% at 450 mW and slightly decreasing to 25% at the maximum input power. We suspect a combination of many factors for this. Most likely many thermal effects will contribute to a change in the beam alignment and mode matching. As can be seen in the Pre-TA module (see section 3.3.4) when operating the Tapered Amplifier at high currents, thermal drifts will cause shifts of the beam path. Also the mode of the Tapered Amplifier output is dependant on the operating current as can be seen in section 3.3.5. Also thermal lensing effects, although already being minimized by choosing a larger waist, will still be visible.

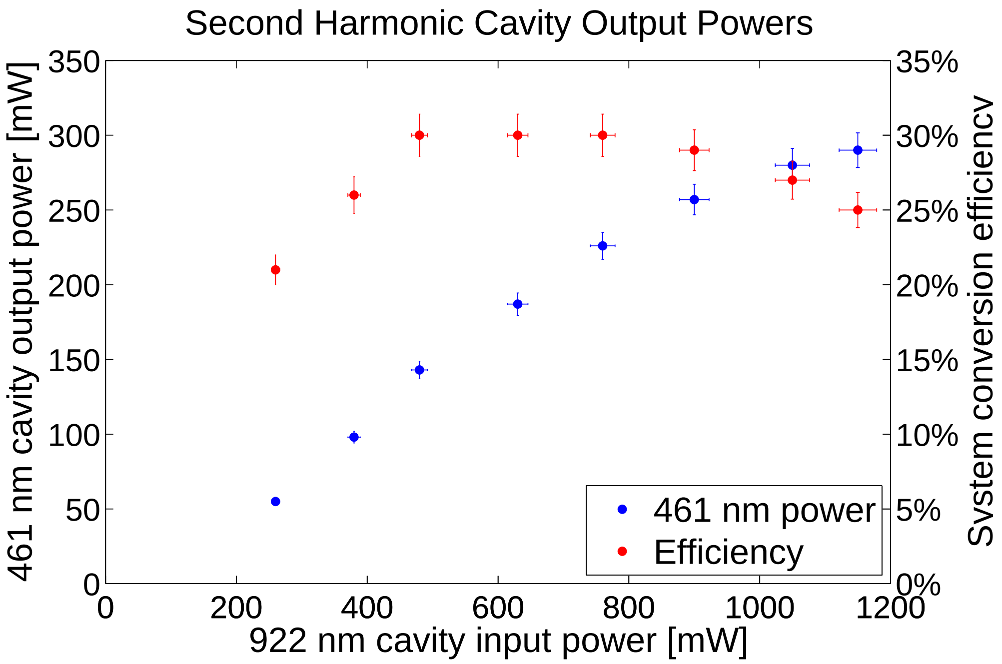

FIGURE 3.25: Blue: Measured cavity blue output power as a function of non mode matched input power. Red line: Total system conversion efficiency (defined as output power divided by non mode matched input power).

The achieved system conversion efficiency is lower than other reported efficiencies of typically between 50%-60% [97, 105, 106]. Two main reasons are identified for the discrepancies to other projects. The main reason is the mode matching. Typically 40%-47% of the input beam is coupled into the cavity, compared to typical mode matching values of around 70% being reported in other experiments [97, 105, 106]. Further beam shaping optics should be able to increase our coupling efficiency into the cavity. Due to the modular setup of our system and not having planned for additional mode matching optics in the design phase of this module, no space is left to include these. The second reason was identified as being thermal lensing in the crystal, which will be discussed in the following paragraph.

The conversion efficiency is defined as:

$$\Gamma_{eff} = \frac{P_{2\omega}}{P_c^2} \tag{3.39}$$

Where $P_{2\omega}$ is the second harmonic power and P_c is the circulating intra cavity power. As can be seen in figure 3.26 the conversion efficiency is nearly constant between 1.5 W and 2.6 W, but decreases afterwards. The maximum value of $\Gamma_{eff} = 2.1 \cdot 10^{-2} W^{-1}$ is in good agreement with another strontium experiment using the same crystal [97]. But the conversion efficiency should be a constant value for a specific crystal. This effect is most likely caused by thermal lensing reducing the conversion efficiency as it gets more dominant at higher intensities [97].

To determine the circulating power in the cavity, the 922 nm reflectivity of mirror M2 in the cavity was determined. A transmission of 0.07±0.005 % at 100 mW power on the mirror was measured. A maximum circulating power of 4.5 W was achieved.

To achieve optimum phase matching the temperature of the crystal has to be adjusted to match the wavelength. For the fundamental laser Frequency of $\nu = 325.25115$ THz

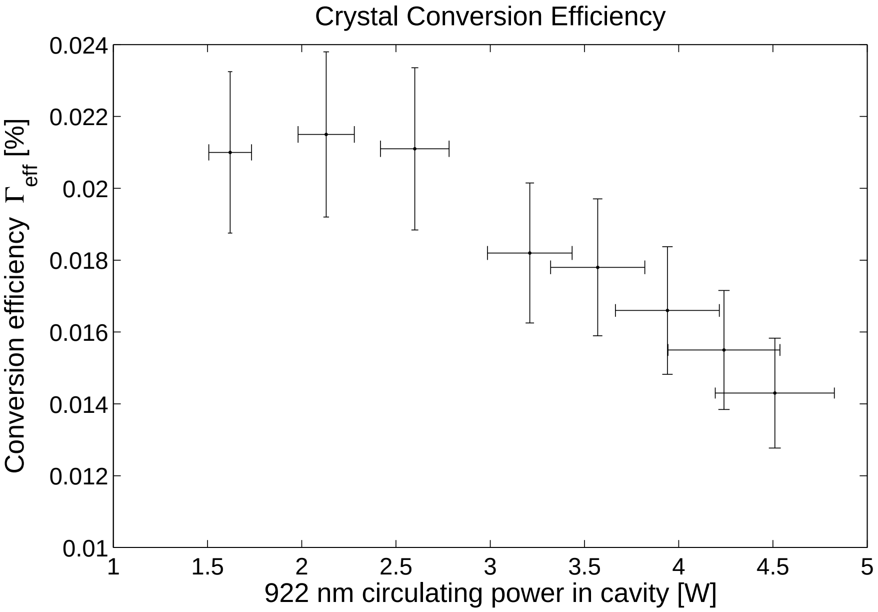

FIGURE 3.26: Measured effective crystal conversion efficiency as a function of circulating power in the cavity. Errors are from measurement accuracy of power meter.

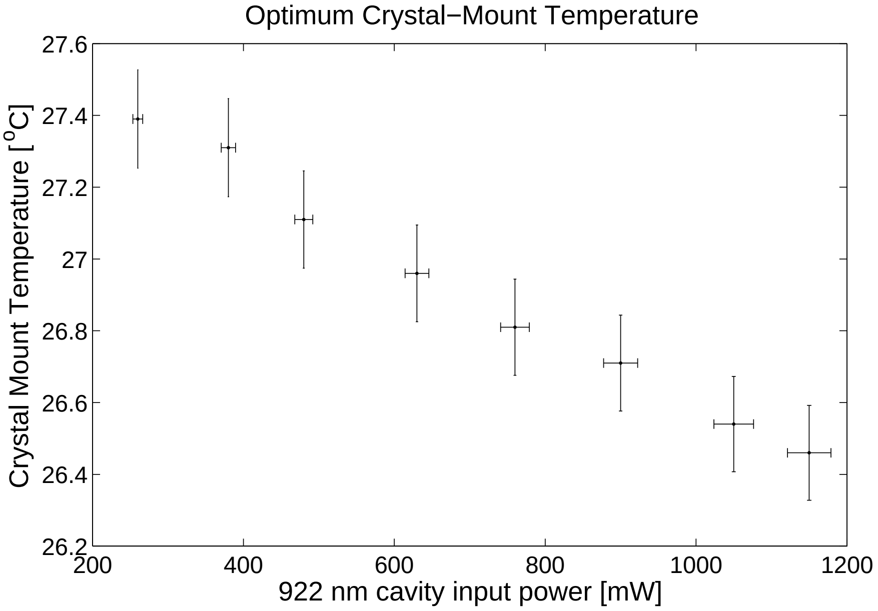

FIGURE 3.27: Measured crystal temperature for optimum conversion efficiency as a function non mode matched cavity input power. Errors are from measurement accuracy of power meter and uncertainty of thermistor. Thermistor has an absolute temperature offset of up to 5%.

(measured by wavelength meter) for strontium the crystal is kept at a temperature of R_T/R_{25}=0.93 (with R_{25} being the resistance of the thermistor at 25°C and R_T the resistance at the measured temperature) which is 26.6°C for the typical operational current of 2.25 A of the Tapered Amplifier. In figure 3.27 the temperature dependence on the input power for optimum conversion is plotted. These measurements were taken in the same test series as figure 3.25. Here the laser was running at a frequency of $\nu = 325.25115$ THz ± 50 MHz. The temperature had to be decreased from T=27.4°C to T=26.4°C for low power to maximum power operation. This can be explained by the additional heating caused by the absorption of the fundamental and second harmonic light in the crystal.

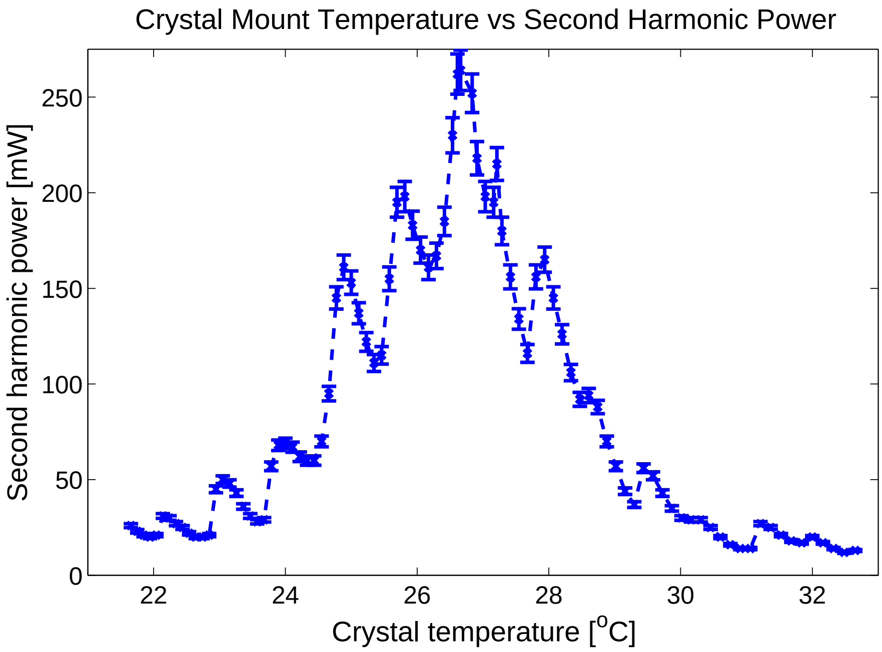

FIGURE 3.28: Crystal temperature tuning curve. The temperature is measured in the copper mount for the crystal. The TA was at the typical operational current of 2.25 A. Measurement was taken from the peak outwards.

For the typical operational current of 2.25 A for the Tapered Amplifier the temperature tuning curve measured internal to the cavity is shown in figure 3.28. The FWHM temperature tuning bandwidth is ΔT=2 °C being almost a factor of two larger than reported in [97] which are using a crystal from the same company. The reason for the several side maxima as well as the larger temperature width are unknown. We suspect our crystal has a lower quality in the periodicity in the periodic poling, causing several side maxima in the conversion.

3.3.6 Spectroscopy

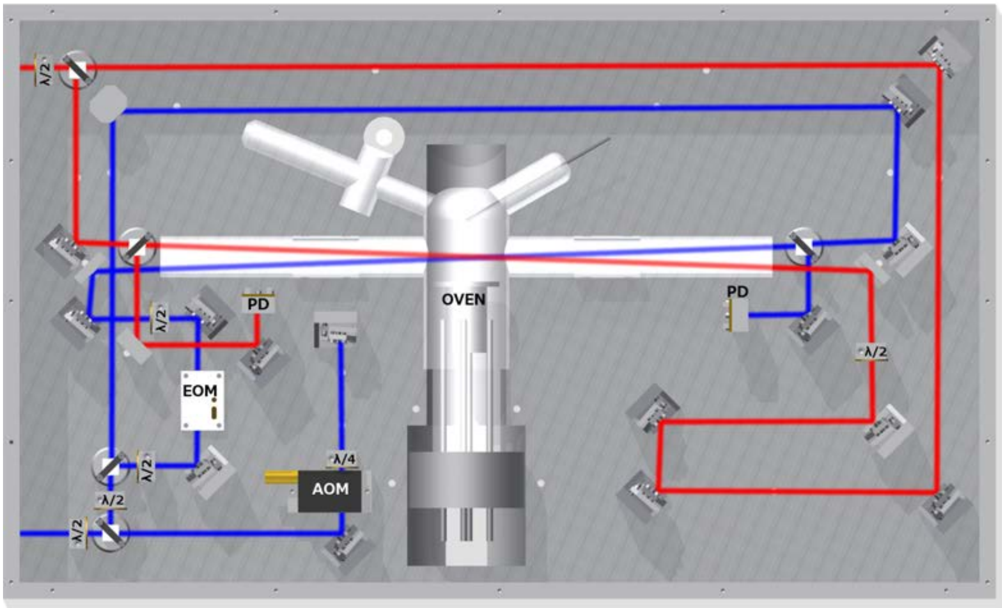

FIGURE 3.29: Schematic overview of the Spectroscopy Module. The beam paths for the blue 461 nm and the red 689 nm laser are shown. The blue light enters the module on the bottom left, is then double passes through an AOM and is split into two beams. One is modulated by am EOM, sent through the cell and is measured by a photo diode. The other beam is guided around the cell and then overlayed in the cell. The red 689 nm laser is not yet implemented. The red light enters the module on the top left, is split into two

To stabilise the 461 nm laser to the $^1S_0$ to $^1P_1$ transition (see section 2.1) in strontium, a heated vapour cell is used. Strontium has a low vapour pressure compared to alkali metals such as Rb. To reach a similar vapour pressure as Rb at room temperature it needs to be heated to 600 K and even higher temperatures are required to reach a suitable pressure for spectroscopy. The spectroscopy cell constructed for this experiment has a built in oven. The oven consists of a metal tube in which 1-2 g of strontium are kept. Surrounding that is a ceramic with a tantalum wire wound around it, used as a heating source. Finally a thermal shield is fitted around the oven, which can be seen in the centre of figure 3.29. The viewports are kept at a distance of 15 cm from the oven to prevent coating with strontium.

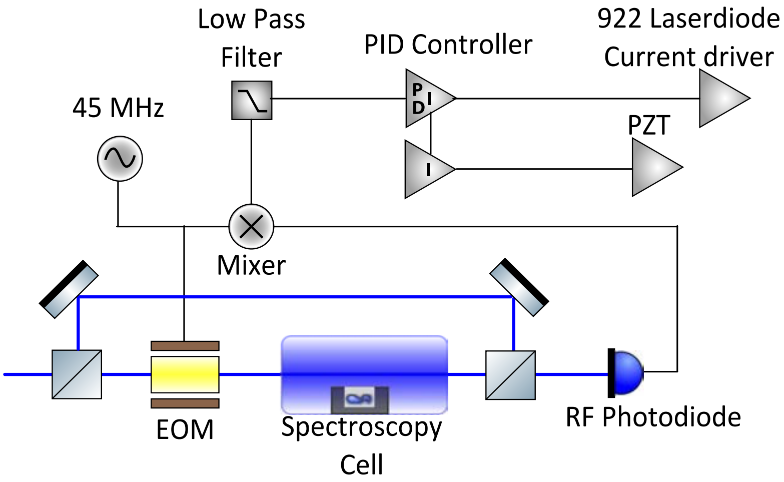

FIGURE 3.30: Schematic overview of locking electronics used to lock the 461 nm laser to the $^1S_0$ to $^1P_1$ transition in strontium

The light entering the module is frequency shifted in a double pass AOM. Afterwards the light is split into a probe and a pump beam. The side-bands of 45 MHz for the FM-spectroscopy [103, 107] are modulated onto the probe beam by an electro optical modulator (EOM). A schematic of the electronics used can be seen in figure 3.30. The probe beam is sent through the cell and is focused onto a photo diode. The pump beam is directed around the cell and counter propagates through the cell to achieve Doppler free spectroscopy. A cube is used to overlay the beams in the spectroscopy cell.

The RF signal from the photo diode is fed back into the mixer, where the error signal is extracted by a lock in amplifier. The error signal is filtered by a 2.5 MHz low pass filter to filter out any residual 45 MHz modulation. The error signal is fed to the proportional, integral and differential (PID) controller to produce a control current for the laser diode and the PZT. In the fast path the PID control signal is generated to compensate any rapid changes in the frequency of the laser. In the slow path only an integral control signal with a longer integration time is generated and fed to the PZT to compensate for drifts.

In figure 3.31 a plot of the error signal and the DC part of the transmitted beam are

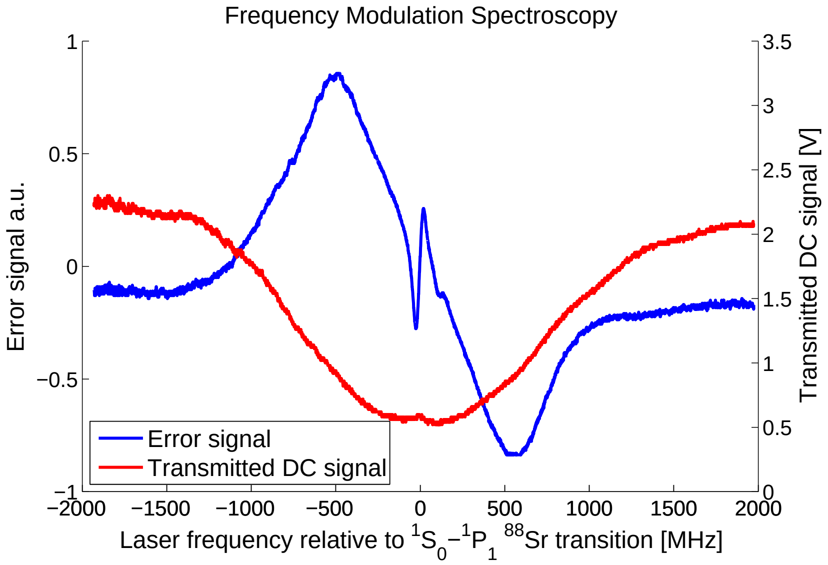

FIGURE 3.31: Blue line: Error signal for spectroscopy on the $^1S_0$ to $^1P_1$ line in strontium showing features of the Doppler valley (large signal), ^{88}Sr (centred signal) and ^{86}Sr (small signal to the right of the centre). The frequency axis is calibrated by the ^{88}Sr and ^{86}Sr features. Red line: Absorbed light in strontium cell showing the Doppler valley

shown. The Doppler Valley can be seen in this plot. A FWHM of 0.73 GHz of the Doppler valley was measured. The Lamb Dip [108] for the Doppler free spectroscopy is visible in the centre of the Doppler Valley. Three features are visible on the error signal. The large slope is the spectroscopy actually resolving the Doppler Valley, this is believed to be due to the large modulation frequency chosen here. The feature at the Lamb Dip is the error signal of ^{88}Sr, which we are locking to. A smaller feature on the right of the centre is from ^{86}Sr.

I have set up, in conjunction with a fourth year project, a second locking system using modulation transfer spectroscopy. This system uses a dispenser as a strontium source in a standard Conflat (CF) vacuum system, following the setup in [109]. This allows for better transportability and easier reduction in size. In modulation transfer spectroscopy the pump beam is modulated and the modulation is transferred only to the probe beam if both beams interact with the same atom, meaning only atoms with zero relative velocity to the beams will be visible. Due to this fact only the atomic feature is probed

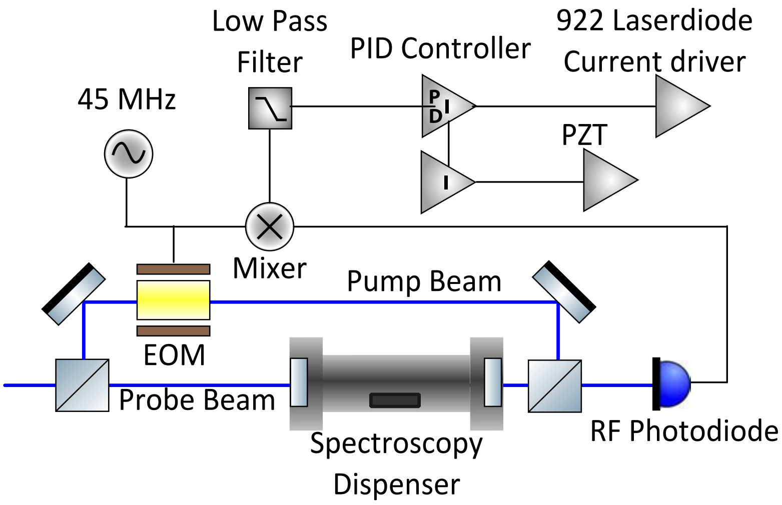

FIGURE 3.32: Schematic overview of locking electronics used to lock the 461 nm laser to the $^1S_0$ to $^1P_1$ transition in strontium using modulation transfer spectroscopy

and not the Doppler valley as it was visible in frequency modulation spectroscopy. This eliminated the drifting frequency offset caused by the resolved Doppler valley, which was visible during a beat measurement with the 461 nm diode laser (see section 3.2.3). The setup is shown in figure 3.32 illustrating the altered modulation setup and the new vacuum system. A typical locking signal is shown in figure 3.33, with a feature from ^{86}Sr also visible.

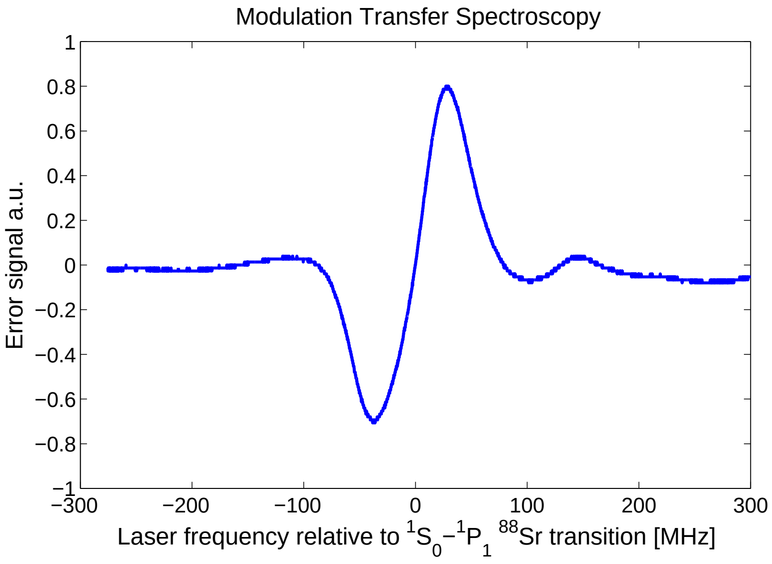

FIGURE 3.33: Error signal for spectroscopy on the $^1S_0$ to $^1P_1$ line in strontium using modulation transfer spectroscopy. The large feature if from ^{88}Sr and the small one from ^{86}Sr. The frequency axis is calibrated by these two features.

3.4 Repumping modules

The main cooling transition of strontium is, as described in section 2.1, not fully closed. Atoms can decay into a metastable state, limiting the atom numbers of the MOT. To prevent this two repumping lasers are used.

I have designed and built two repumping modules. Both have an extended cavity diode laser (ECDL) setup with an anti-reflex coated diode and a 1800 l/mm grating[8] in the common Littrow [90] configuration.

In the current version of the repumping modules anti-reflection (AR) coated laser diodes at a wavelength of 679 nm[9] and 707 nm[10] are used. The laser diode is mounted on a temperature stabilized mount in which the lens is glued to give a beam diameter of 1 mm. The 5x5 mm wide and 3 mm thick grating is mounted on a PZT[11]. Maximum powers of 53 mW and 13.2 mW with a lasing threshold current of 32 mA and 38 mA are achieved for the 707 nm and 679 nm diodes respectively, being well above the required low powers in the lower mW range.

In a previous version of these modules non anti-reflex (AR) coated diodes were used, which are available at a considerably lower price. The in section 3.3.3 described competition of the modes required continuous, time consuming retuning of the laser. With the new AR coated diodes the mode hop free range increased from around 100 MHz to 5 GHz, measured by observing the mode hops on the wavelength meter, and a considerably lower drift is observed.

---

[8] Zeiss 263232xx91

[9] Laser 2000, SAL-0680-025, 60 mW original power, AR-coated

[10] Laser 2000, SAL-0705-020, 60 mW original power, AR-coated

[11] PI P-820.10, 15 μm travel, 50/10 N push-/pull-force

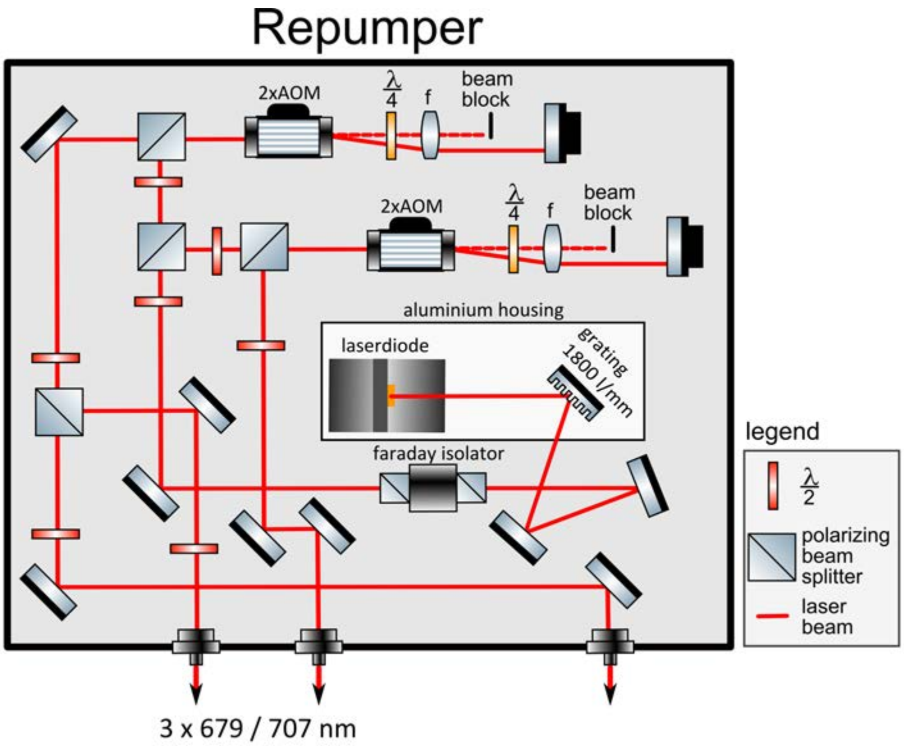

(a) Schematic of the repumper module

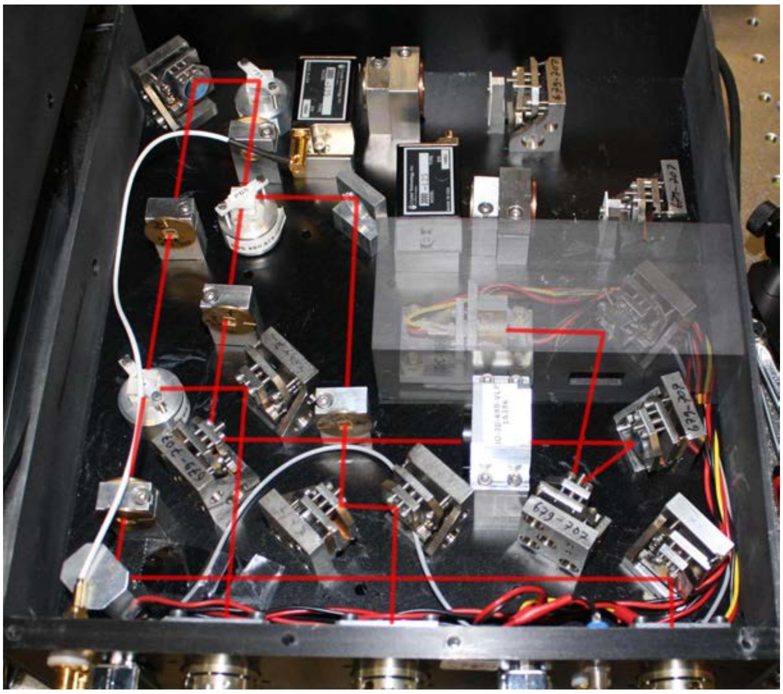

(b) Photograph of the repumper module with drawn beam path

FIGURE 3.34: Schematic showing the laser path and optical elements of a repumping module. The ECDL is thermally stabilised by an aluminium housing. Reflections back into the laser diode are minimized by a faraday isolator. The beam is split up into two paths, one for locking the other for 2D- and 3D-MOT. The laser can be passed through a double pass AOM, if detuning is required, but they can be bypassed as they currently are.

The two modules have the same layout, except for a shifted mirror after the grating to compensate for the slightly different angles. The ECDL setup is shielded by an aluminium housing to further stabilize the laser from thermal and air fluctuation drifts. After the grating the beam passes through a 35 dB optical isolator[12], suppressing any reflections back into the laser diode, which can act as additional competing modes. A second isolator can be installed if the suppression of reflections from the first isolator is not sufficient. The beam is then split into two paths.

The beams can each be sent through an AOM in double pass configuration, as described in section 3.1. In the current setup the AOMs are bypassed, since no detuning is required. A total efficiency, measuring the power before and after the PBS, of up to 65% is achieved. The beams are then coupled into three fibres, one for the each of the MOTs and one for spectroscopy.

3.4.1 Repumper Stabilisation

The repumpers can be operated without being stabilized to an external reference, but their frequency will need to be readjusted after a certain time. The first installed non anti-reflex coated laser diodes would stay at the required frequency from anywhere between 5 to 30 minutes. The new anti-reflex coated diodes show more stability, but still require readjustment after 30-60 minutes. To avoid the constant readjustment of the repumpers and have consistent parameters for the MOT operations, I devised a scheme to lock the repumping lasers.

Up to now typically the repumping lasers for strontium were referenced to cavities for stabilisation. In the scheme presented here, a direct stabilisation on the atomic transition

---

[12] OFR IO-3D-700-VLP

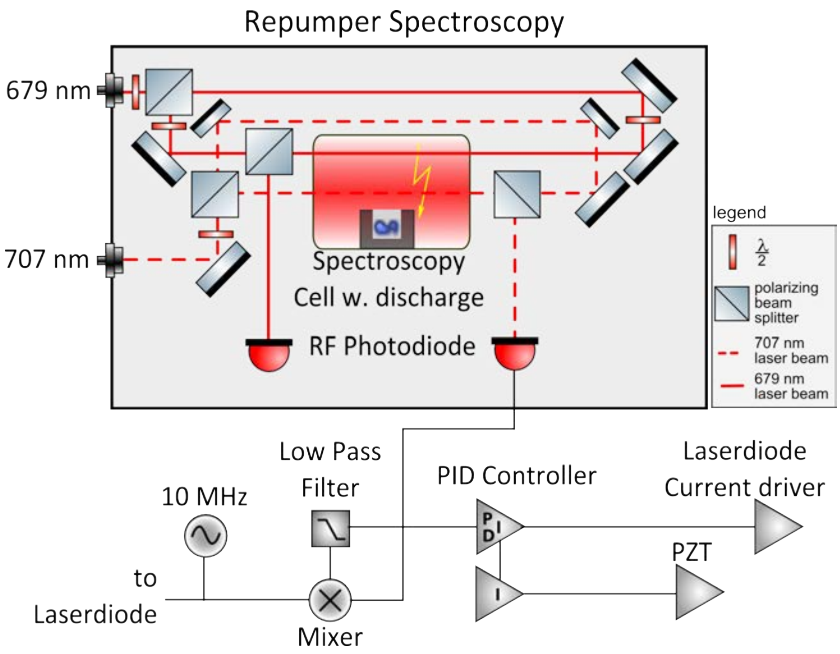

(a) Schematic of the spectroscopy cell for the repumpers with dc discharge

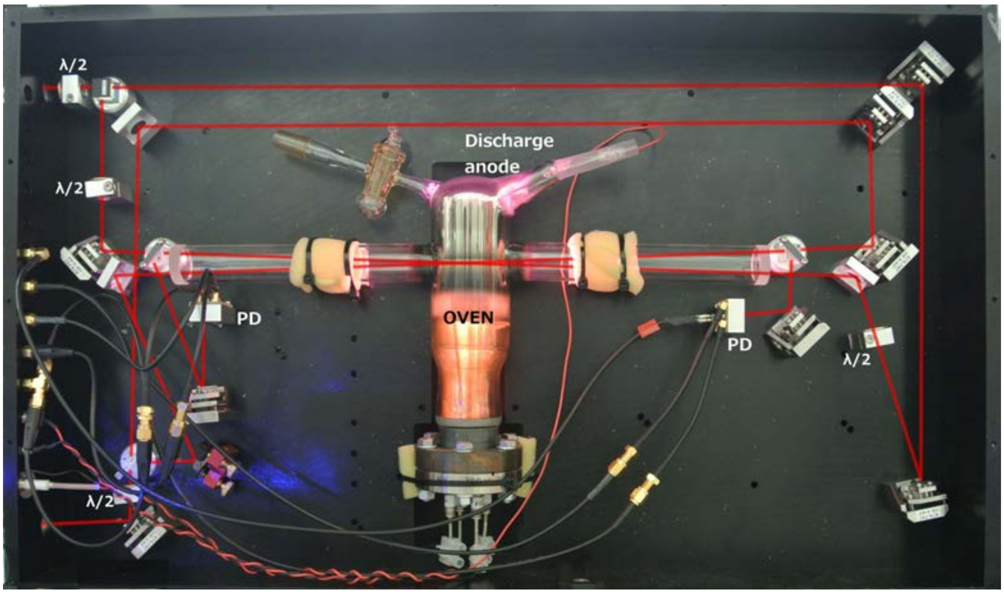

(b) Photograph of the spectroscopy cell for the repumpers with dc discharge.

FIGURE 3.35: Schematic overview and photograph of the repumper spectroscopy module. (a) Schematic overview of the repumper spectroscopy module. The electronics is shown for the 707 nm laser. The electronics for the 679 nm laser is identical. The 10 MHz laser modulation for the FM-spectroscopy is achieved by directly modulating the laser diode. (b) Photograph of the repumper spectroscopy module showing the beam path. The discharge in the oven is visible by the purple and yellow colour.

is possible. Since the repumping transitions are not directly accessible from the ground state (see section 2.1), a dc discharge is used to populate the ^3P_j states to allow for spectroscopy of the repumping transitions. The module housing the components and the spectroscopy cell have the same design as described in section 3.3.6 for the 461 nm spectroscopy. To create the discharge an electrode is placed above the strontium oven. The dc discharge ignites at a voltage of 300 V and a yellow to purple glowing is visible in the spectroscopy cell, as is shown in figure 3.35. To generate a locking signal the same FM-Modulation scheme and electronics as for the 461 nm laser are used.

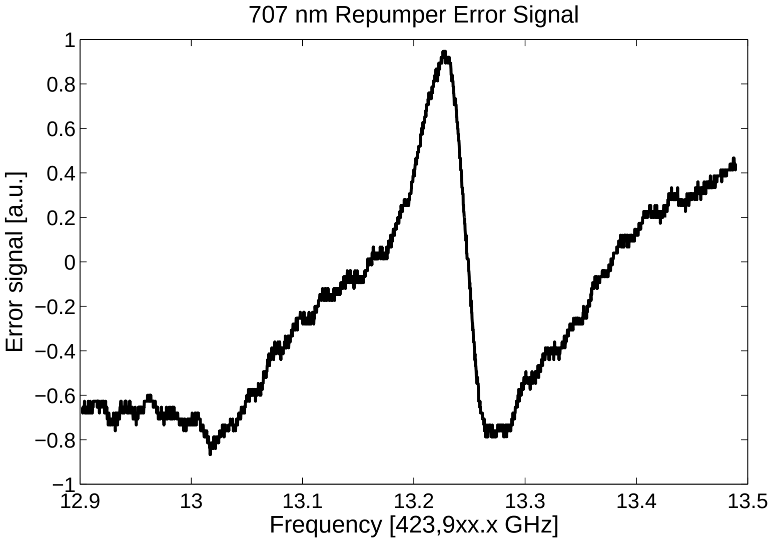

FIGURE 3.36: Error signal of 707 nm repumper laser. DC discharge in the oven is on. When discharge is turned off this signal disappears.

Out of the two repumpers the 707 nm repumper shows a clear error signal, which is shown in figure 3.36. The error signal is about 20 MHz wide, which is in the expected range, since the linewidth of this transition is 7 MHz. This repumper has been successfully in lock for several hours while operating the MOT. The 679 nm repumper has also successfully been locked. Due to electronic noise of unknown origin on the signal from the RF photo diode currently no usable error signal can be obtained.

3.5 Distribution modules

To supply the 2D- and 3D-MOT with the laser beams, I have designed and built two distribution modules. These modules detune the blue laser, overlay it with the repumpers and split the beams into the required number of outputs.

The 2D distribution module (see figure 3.37) supplies two fibres to the 2D-MOT as well as one fibre each for pushing and detection beam. It has one input for the 461 nm laser and two inputs for the repumping lasers. Part of the 461 nm beam is directly diverted to a fibre output for the spectroscopy module. The other part of the beam is split in a polarizing beam splitter (PBS) and the frequency of each beam is adjusted by two AOMs. The beam for the 2D-MOT is overlayed with the two repumping beams using a dichroic mirror and coupled into two fibres for the 2D-MOT. The other beam is again split into two beams. One is the pushing beam for the 2D-MOT and the other one is an optional detection beam for the 3D-MOT. They share the same AOM since they will not be operational at the same time.

The double pass AOMs in this module have an efficiency of 60%, which is measured as the power before and after the polarizing beam splitter (PBS). The fibre coupling typically has an efficiency of 60%, being the power before and after the fibre. In total this module offers a 33% efficiency, combining the AOM and fibre coupling efficiency and adding an additional 10% loss for all the optics along the path, for the 2D-MOT, pushing and detection beam. Due to limited blue power available (see section 3.3) the two beams for the 2D-MOT are guided via free space (see figure 3.37b) to the vacuum chamber to prevent the intensity loss from fibre coupling.

The 3D distribution module (see figure 3.38) supplies the 3D-MOT with six fibres, one for each beam of the MOT. It has four inputs: one for the 461 nm cooling laser, two for

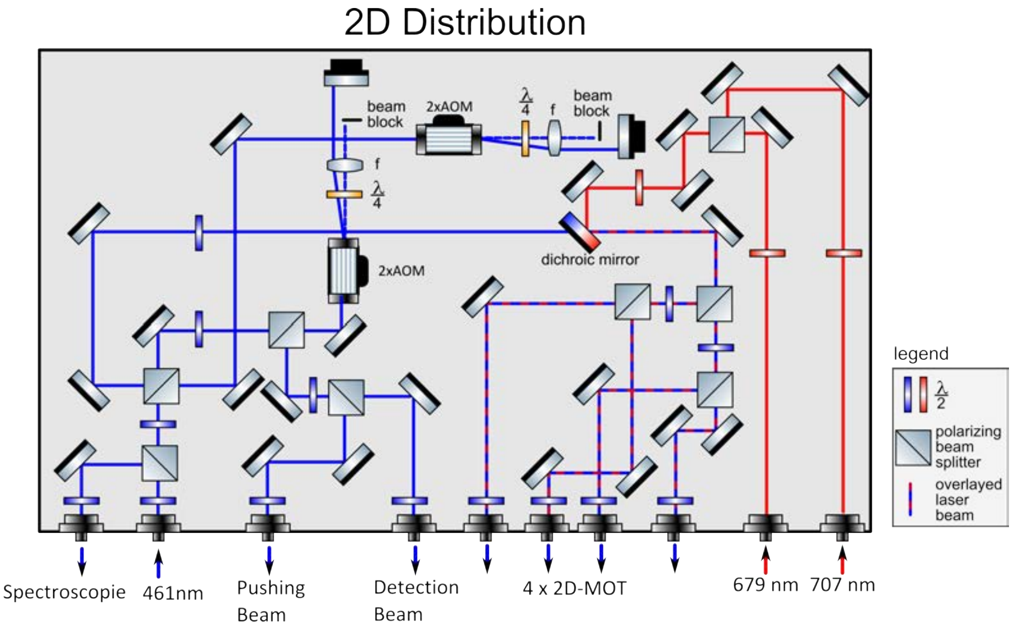

(a) Schematic of the distribution module for the 2D-MOT

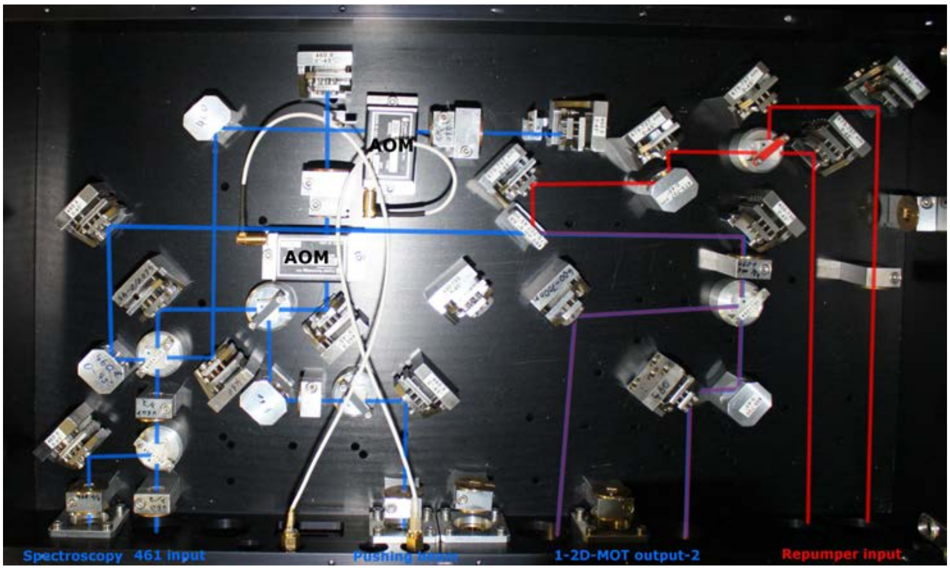

(b) Photograph of the 2D distribution module with drawn beam path

Figure 3.37: Schematic and photograph of the distribution module for the 3D-MOT. The 461 nm laser entering the module gets split into several beams: i) one for spectroscopy, ii) one for pushing and detection and iii) one for the 2D-MOT. Beams ii and iii get frequency shifted by a double pass AOM. The for the 2D-MOT gets overlayed with the repumping lasers, is split into four beams and coupled into fibres. As can be seen in b) the detection beam is currently not yet installed and only two outputs are used for the 2D-MOT.

the repumpers and one optional one for the 689 nm cooling laser. All of the inputs can be overlayed and coupled into the same fibre. The 461 nm beam is first double passed through an AOM to adjust the detuning and allow for quick on and off switching of the beam. The repumpers are overlayed using a PBS. Afterwards they are overlayed with the 689 nm beam in a second PBS. For this the polarization of the repumping has to be turned by 45°, leading to a loss of 50% of the power. This is acceptable since the repumping modules deliver sufficient power. Due to the wavelength difference between the blue and the red beams, a dichroic mirror is used to overlay them. The beam is split into six beams and coupled into the polarization maintaining fibres for the 3D-MOT.

Since a broad wavelength range is coupled into the fibres a different type of fibre coupling lens is used to ensure optimum focussing for all wavelengths. Typically an aspheric lens (M5) is used in fibre couplers. Aspheric lenses focus light without introducing spherical aberration into the transmitted wavefront, enabling very good coupling efficiencies. But this is only achieved for the designed wavelength range of the lens. To still have a nearly diffraction limited performance for both red and blue light an achromatic lens (M4) is used. Achromatic lenses offer a nearly similar optical quality as aspheric lenses, but they achieve this over a wide wavelength range. In figure 3.39 the theoretical coupling efficiencies for both lenses are plotted. When the M5 aspheric lens would be used for both wavelength ranges a theoretical coupling efficiency of 99% for 689 nm and 89% for 461 nm for a perfect beam would be achieved. With the M4 achromatic lens theoretical coupling efficiencies of 100% and 97% respectively are expected.

In reality coupling efficiencies are a lot lower than the theoretical predictions, due to a combination of several factors. For one the surface of the fibres are not anti reflection coated causing a 4% loss at each surface. Also the beam is being distorted from the many optical elements in the beam path, causing a reduced coupling efficiency. From

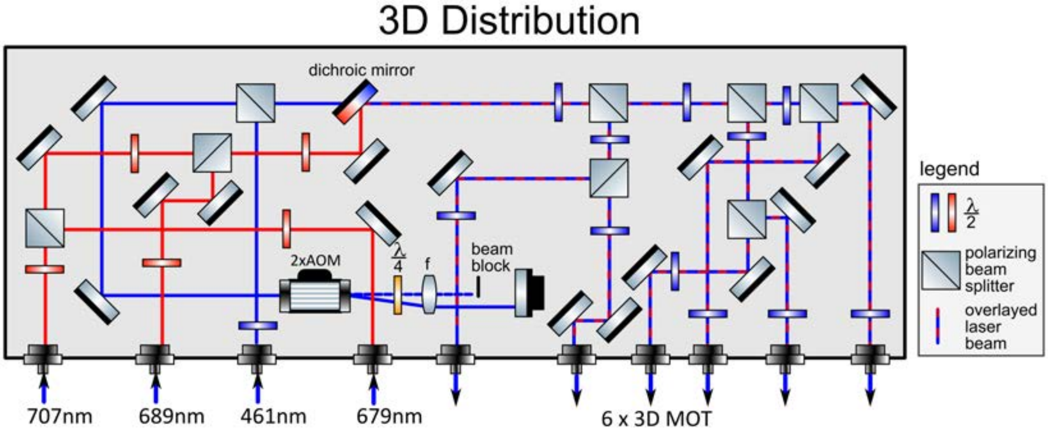

(a) Schematic of the distribution module for the 3D-MOT

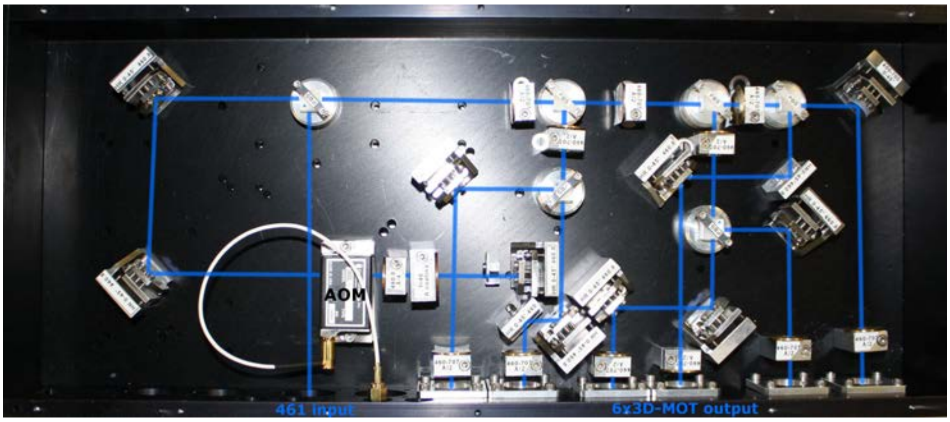

(b) Photograph of the 3D distribution module with drawn beam path

FIGURE 3.38: Schematic and photograph of the distribution module for the 3D-MOT. The 461 nm laser entering the module gets frequency shifted by a double pass AOM and is overlayed with the two repumping lasers as well as the 689 nm laser. The overlayed laser beams are then split into six beams, two for each axis of the 3D-MOT and coupled into fibres. In the current module the repumpers and the 689 nm laser are not yet installed.

experience I expect a coupling efficiency of 65%-75% for a single wavelength using an aspheric M5 lens. In the 3D-module I get a maximum coupling efficiency of 55-65% with the blue light using the achromatic M4 lens. This is a 10% lower coupling efficiency than expected indicating that the achromatic M4 lens does not have a similar performance compared to the aspheric M5 lens. Simultaneous coupling of the blue and red beams has not yet been implemented.

Combining the efficiency of the AOM of 60%, the fibre coupling efficiency of 55% and adding a combined loss of 10% for all the additional optics, the 3D-module offers a total

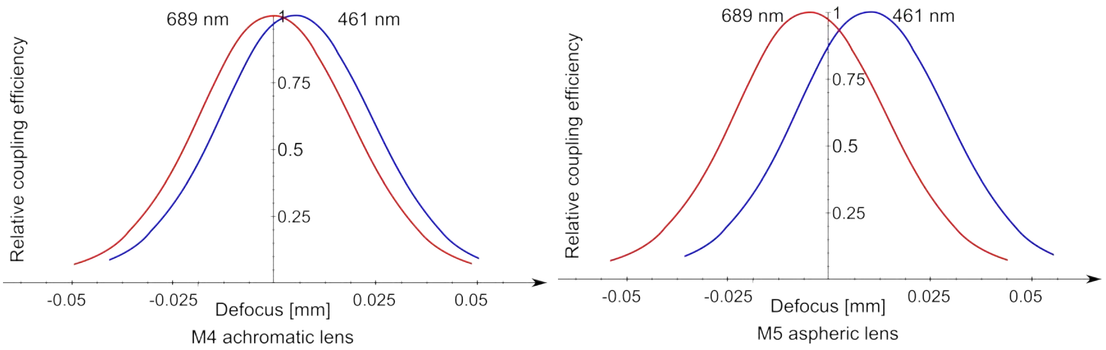

(a) M4 achromatic lens (b) M5 aspheric lens

FIGURE 3.39: Approximation of the coupling efficiency for Schäfter und Kirchhoff fibre coupling lenses. Defocus donates how much the coupling lens has to be moved to reach this point. The M5 aspheric lens offers the best coupling efficiency for a single frequency, where as the M4 achromatic lens offers better results for a broad range of wavelengths at a slightly decreased efficiency at optimum defocus for a specific wavelength. More detailed plots can be found in appendix B.

efficiency of 30%. The repumpers and 689 nm cooling laser are not yet implemented in this module. This module offers a good stability over time, but regular readjustment of the fibre coupling is required. Typically the coupling of the fibres is readjusted up to every month with them having lost up to 5% of the coupling efficiency.

3.6 Summary

In this chapter I have given an overview of the laser systems constructed to successfully trap neutral strontium atoms. A total of nine modules were constructed for a mobile system. The frequencies of the lasers are detuned by AOMs in double pass configuration, allowing for an adjustment of the detunings without readjusting the beams. Two repumping modules at 679 nm and 707 nm have been constructed with the frequencies being stabilised to the atomic transition with a discharge spectroscopy cell. They provide a power of 5 mW and 22 mW respectively in up to three fibres. A laser system at 461 nm using a robust monolithic frequency doubling cavity for the main cooling transitions of strontium has been constructed and characterized. A maximum output power of 300 mW was observed. This allows for a power of 1.5 mW per beam for the 3D-MOT from the 3D-distribution module and 30 mW per beam for the 2D-MOT from the 2D-distribution module. Although three additional blue laser sources were analysed for their suitability for a mobile system, currently only the home made frequency doubling cavity provides the required power level for the experiment.

Chapter 4

Experimental Setup

In this chapter the vacuum apparatus for the magneto-optical trapping of strontium and the experimental control system are presented. For the vacuum apparatus modified and newly developed techniques for the sealing of viewports and generation of magnetic fields will be introduced. For the control of the experiment the components of the experimental control system will be presented and the design of the computer control and imaging system will be discussed.

4.1 Vacuum Apparatus

For the mobility of the experiment, the vacuum apparatus is build on a breadboard allowing it to be transported. A CAD drawing of a slice of the vacuum apparatus can be seen in figure 4.1 highlighting the main components and a photograph showing the entire setup in figure 4.2. It can be divided into two main areas (see section 4.1.1): The vacuum chamber for the 2D-MOT and the vacuum chamber for the 3D-MOT and lattice for the clock operation. The two chambers are connected via a differential pumping

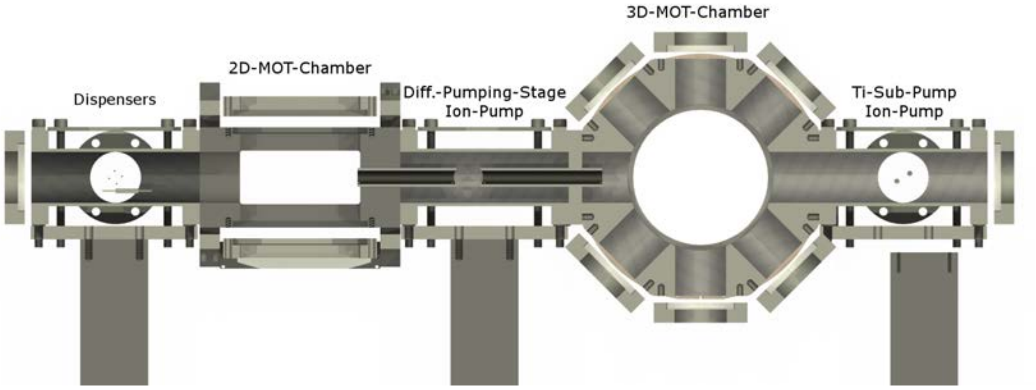

Figure 4.1: CAD drawing of the vacuum apparatus. Components from left to right: 4-way-cross with two dispensers and foil, custom made vacuum chamber for 2D-MOT, T-piece with differential pumping stage and ion pump for 2D-MOT chamber, vacuum chamber for 3D-MOT, 4-way-cross with ion pump and titanium sublimation pump for 3D-MOT chamber

stage (see section 4.1.2), which will create a pressure difference of up to two orders of magnitude. All viewports are custom made and sealed with a special lead seal, to be able to achieve a better optical quality (see section 4.1.4). The vacuum apparatus is set up horizontally to have two vertical viewports for the optical lattice, to avoid mechanical oscillations, which could arise from a high vertical setup and allow for an easier transport. For almost all major components 316L steel was used. This steel has a low magnetic permeability (typically below μ_r =1.005[1]) to lower magnetic stray fields, which could affect the accuracy of the clock transition.

4.1.1 MOT Chambers

The experimental apparatus has two vacuum chambers: One for the pre-cooling of atoms and one to capture and probe the atoms. The two chambers have different requirements for the optical access and the pressure. Whilst the 2D-chamber needs long viewports with a relatively high pressure to ensure a large flux of pre cooled atoms, the 3D-chamber requires optical access for six MOT beams and the optical lattice, whilst being at a low

---

[1] Source: S. Yadev, Fermilab Report, TD-01-065, September 2001, Fermi National Accelerator

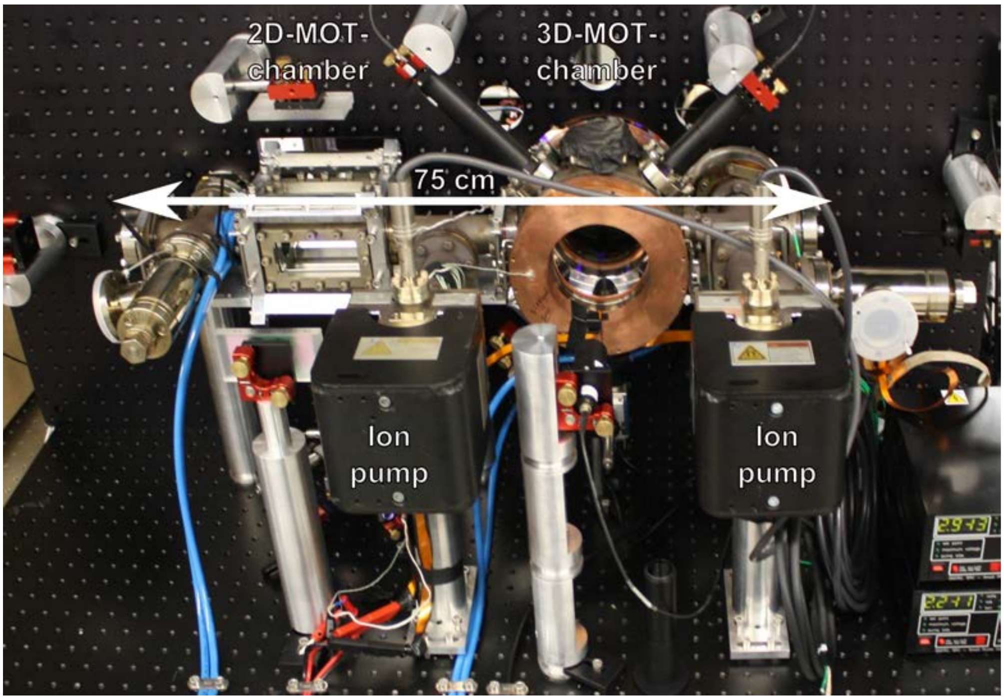

Figure 4.2: Photograph of the vacuum chamber

pressure. At an early stage of planning it was considered to coat the inside of the 3D-chamber with special titanium layer, which would serve as a getter material to ensure a good vacuum pressure. This getter layer required to be baked to 180°C for activation. Due to time constraints this option was not further pursued.

To reduce the outgassing of the stainless steel surfaces a special baking procedure was used. First the evacuated vacuum chambers, with blind flanges instead of viewports installed, were cycled three times between room temperature and 400°C with venting them with air between cycles [110]. To create a protective oxide layer the final assembly was heated to 120°C and vented with air for five minutes [111], before the final bakeout at 200°C for several days. After firing the Titanium-Sublimation-Pump a measured pressure by an ion-pump of in the region of 10^{-12} mbar was achieved in the 3D-chamber. But at these pressure levels ion pump pressure readings are very inaccurate and can easily be off by an order of magnitude.

2D-MOT Chamber

In a two dimensional MOT atoms are cooled in two dimensions. This results in an elongated one dimensional atomic ensemble, which delivers pre-cooled atoms for the 3D-MOT.

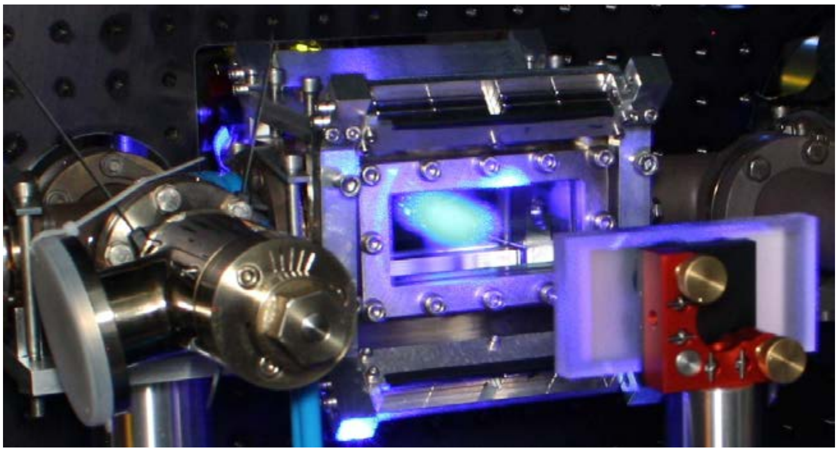

(a) Photograph of 2D-MOT chamber

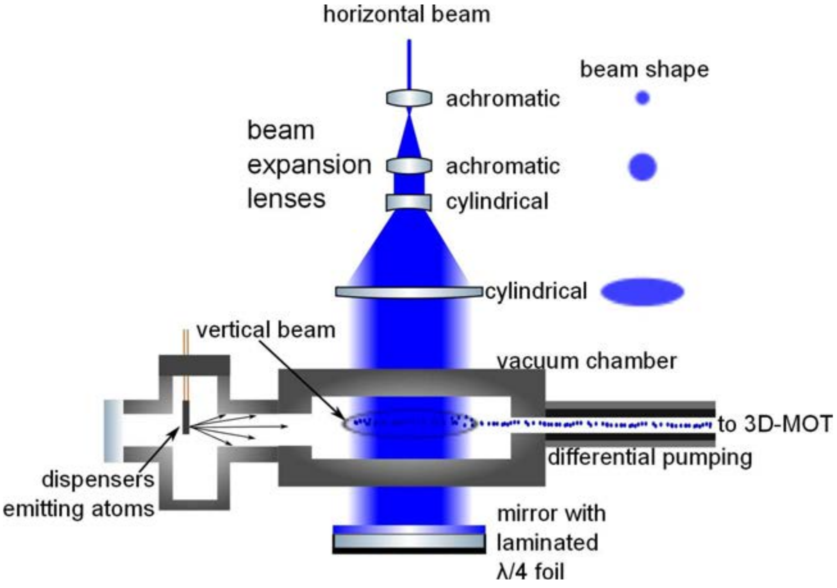

(b) Schematic of 2D-MOT chamber

Figure 4.3: (a) Side view photograph of the 2D-MOT chamber with fluorescence visible. Around the chamber the permanent magnets are visible. In front rectangular mirror with quarter waveplate foil. (b) Top view schematic of the 2D-MOT chamber. The path of the horizontal laser beam is shown. The vertical beam has an identical setup. The atoms in the 2D-MOT and their path to the 3D-MOT are shown.

In this experiment the first 2D-MOT with strontium was realised. The 2D-MOT offers a range of advantages over Zeeman-slowers, which use an oven as a strontium source, which are currently used in strontium experiments [9, 86, 87]. In a Zeeman-slower an atomic beam is slowed by a counter propagating laser beam, which is kept on resonance with the majority of the atoms by a tailored magnetic field, allowing them to effectively cool atoms with a large initial velocity and have a high atomic flux. But Zeeman-slowers are usually quite large (up to 1 m in length) [112], thus not being easily transportable. Furthermore there is still a big particle flux coming from the oven, which is not slowed, reducing the lifetime of the 3D-MOT. Due to the high temperature of the oven and the direct line of sight with the 3D-MOT the black body radiation emitted causes a shift of the clock frequency [5]. Initial estimations show that the 2D-MOT can have a similar atom flux as Zeeman-slowers (see section 2.2.1). The dispensers (see section 4.1.3) are mounted out of line of sight of the 3D-MOT, thus minimizing the effect of black body radiation on the atoms probed on the clock transition (see section 1.2.3).

The 2D-MOT chamber is a custom made rectangular shape vacuum chamber (see figure 4.3). The viewports have a 8 cm long aperture to allow for a long capture region of the 2D-MOT to increase the flux. The viewports are sealed using lead (see section 4.1.4) and have an anti-reflex coating for 461 nm and a second transmission peak at 689 nm ranging from 679 nm to 707 nm for the repumpers. On the left hand side of figure 4.3 a 4-way-cross with the dispensers installed is attached. The dispensers are mounted in such a way that the direct dispenser and the foil (see section 4.1.3 for a detailed explanation of the atomic source) have no direct line of sight to neither the viewports nor the 3D-MOT chamber via a differential pumping stage. This is to prevent coating of the viewports with strontium and to prevent black body radiation from shifting the clock transition. A differential pumping stage is installed to have a high vacuum pressure in the 2D-MOT chamber for a maximum flux, while still maintaining a low vacuum pressure in the 3D-MOT chamber (see section 4.1.2).

Viewport birefringence An important effect to consider during the 2D-MOT operation, especially with rectangular viewports, is stress-induced birefringence. I investigated this effect as a function of temperature gradient. I found that the rectangular viewports of the 2D-MOT chamber where acting as a $\lambda/8$ plate each, resulting in a linear, from initially circular polarized, laser beam after passing through both viewports. The effect causing this is a temperature gradient, caused by the dissipating heat of the dispenser and foil. The effect was repeatedly visible during operation of the dispenser and foil, but disappeared after cooling down. Further investigations with a heating strip showed polarization changes up to $\lambda/4$ per viewport at higher temperatures. A water cooling was installed to prevent the observed birefringence.

3D-MOT Chamber

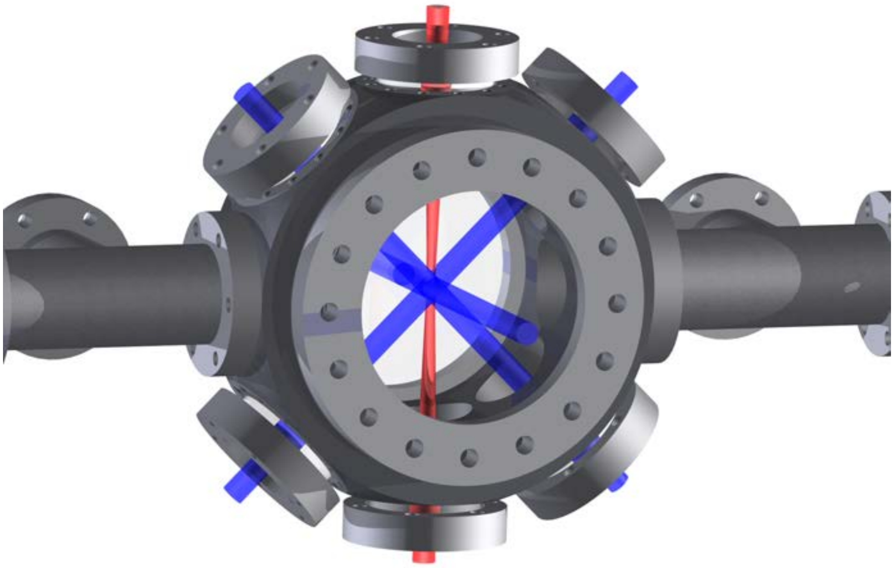

FIGURE 4.4: CAD rendering of 3D-MOT Chamber with the beam path of 1 cm diameter beams for blue MOT and optical lattice beam included

The 3D-MOT chamber is a commercial vacuum chamber from Kimball physics. It has eight DN 35 and two DN 100 flanges and is made out of 316L steel. Two flanges are used to connect the differential pumping stage on the left hand side and the titanium sublimation pump and ion pump on the other side. The viewports on this vacuum chamber are custom made and sealed with a special technique using lead (see section 4.1.4). BK7 is used as a window material with a surface flatness of $\lambda/10$. The viewports for the DN 35 and DN 100 flanges have a thickness of 1 cm and 1.5 cm respectively. The viewports have an anti-reflex coating at 461 nm for the blue MOT, a broad peak at 689 nm ranging from 679 nm to 707 nm for the red MOT, clock transition and repumpers and one at 813 nm for the optical lattice at 0° angle of incidence.

The six beams for the blue MOT will be entering the vacuum through the two large horizontal viewports and four orthogonal vertical viewports (see figure 4.4). The top and bottom viewport are for the optical lattice and clock transition probing beam.

4.1.2 Differential pumping stage

The required pressure ranges for the 2D-MOT and 3D-MOT vacuum chamber vary by a few orders of magnitude. For the 2D-MOT a high strontium background pressure is required to be able to have a high atomic flux. When operating the 2D-MOT I found a typical pressure in the 10^{-8} mbar range to be ideal (see section 5.2). For the 3D-MOT and especially for later steps in the experiment, like the optical lattice, low pressures are required. Typically pressures in the 10^{-10} mbar range are required to optimally operate the optical clock transition.

To achieve the difference in pressure a differential pumping stage is installed. The differential pumping stage is a 183 mm long tube with an inner diameter of 6 mm. The stage consists of a metal tube with 10.1 mm inner diameter in which two carbon tubes with an inner diameter of 6 mm are inserted (as can be seen in figure 4.5). The carbon tubes serve two purposes: The carbon acts as an absorbing material for particles hitting

Figure 4.5: CAD rendering of Differential Pumping Stage. Carbon tubes are visible on the inside.

the wall, thus further decreasing the conductance of the pumping stage. Also the carbon has a low reflectivity for black body radiation, reducing the radiation emitted from the dispenser being reflected into the 3D-MOT region. The diameter of the pumping stage was chosen based on the maximum deflection of the atomic beam due to gravity. With an estimated minimum velocity of 10 m/s for the atomic beam, a deflection of 2 mm is calculated. Including the divergence of the atomic beam, a diameter of 6 mm was chosen.

To estimate the expected pressure difference the conductivity for molecular flow of the differential pumping stage needs to be calculated [113]:

$$C_{tube} = \frac{d^3 \cdot \pi}{12 \cdot L} \cdot \overline{c} \tag{4.1}$$

Where d is the diameter of the tube, L is the length and $\overline{c}$ is the mean particle speed:

$$\overline{c} = \sqrt{\frac{8 \cdot R \cdot T}{\pi \cdot M}} \tag{4.2}$$

Where R is the general gas constant, M is the mean molar mass for air and T is the temperature. For room temperature the mean particle speed is $\bar{c}$=464 m/s. This gives a conductance of C_{diff}=0.15 l/s.

Around half way along the differential pumping stage has a 22 mm wide hole with a 15 l/s ion pump attached to it. This is used to further reduce the pressure and to pump the 2D-chamber. The pumping stage to this point has a conductance of 0.4 l/s.

To estimate the expected pressure difference the effective pumping speed of the 3D ion pump at the exit of the differential pumping stage needs to be calculated. The 3D ion pump also has a pumping speed of 15 l/s. From the ion pump to the 3D-MOT chamber only a four way cross has any relevant conductance. The conductance is calculated using equation 4.1 to L_{cross}=45 l/s, with modelling the four way cross as a pipe elbow, which has the same conductance value as a straight pipe of equal length.

This reduces the pumping speed of the ion pump to an effective pumping speed:

$$\frac{1}{S_{eff}} = \frac{1}{S_{ion}} + \frac{1}{C_{tot}} \tag{4.3}$$

With an effective pumping speed of S_{eff}=11 l/s.

From the ratio of the pumping speed the pressure difference can be estimated to a factor of 75. Taking into account the additional measures like the carbon tubes, a pressure difference of at least two orders of magnitude can be expected. From the 2D chamber to the hole in the centre of the pumping stage a pressure difference of $\frac{0.4\mathrm{l/s}}{15\mathrm{l/s}} = 37.5$ is expected.

During operation a typical pressure reading for the 2D ion pump would be $1 \cdot 10^{-8}$ mbar and the 3D ion pump would show a pressure reading in the lower 10^{-10} mbar range, confirming the expected pressure difference.

4.1.3 Dispensers

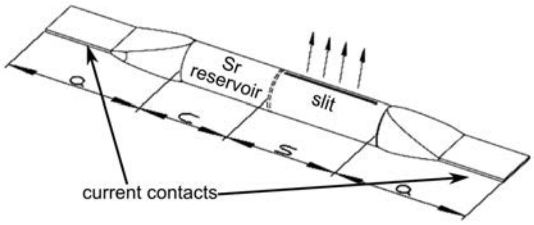

FIGURE 4.6: Drawing of dispenser with custom slit (image from Alvatec) showing slit of the dispenser, the strontium reservoir and the electrical contacts

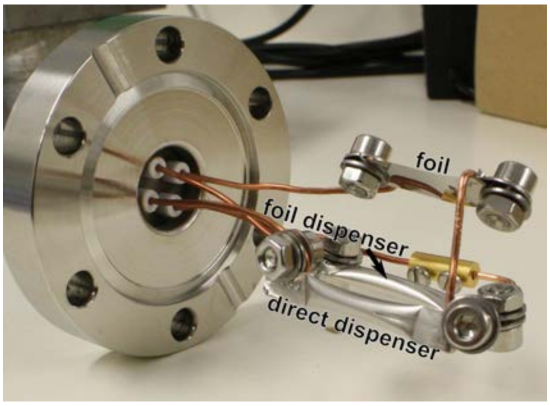

FIGURE 4.7: Dispenser setup with NiChrome foil. In front dispenser pointed directly into 2D-MOT chamber. Behind the dispenser pointing at the foil.

We are using dispensers (see figure 4.6) from Alvatec. These are slitted dispensers, allowing them to be installed in any orientation. The slit is specially designed with a laser cut width of only 0.1 mm, to narrow the beam divergence of the out coming atoms. This is to avoid any coating of the viewports in the 2D-MOT chamber. A problem which could arise is the nozzle effect. Due to the aperture being very small and a high atomic flux, the fast atoms leaving the dispenser are likely to collide with the slower ones, thus accelerating them. The velocity distribution of the strontium beam would no longer follow the Maxwell-Boltzmann distribution, but a similar distribution where the slow and fast atoms are shifted to the middle. This would significantly lower the number of atoms which can be trapped in the 2D-MOT, since it can only capture the slowest 1% of the atoms (see section 2.2.1). To avert this potential problem, a second dispenser is installed, which is pointed towards a heated NiChrome foil (see figure 4.7). This foil gives us two advantages: The atoms evaporated from this foil will follow the Boltzmann distribution, including the slow end tail, and, by adjusting the current passing through the foil, the thermal velocity distribution of the atoms leaving the foil can be reduced at a cost of decreased flux. Both dispensers are installed in a four way cross attached to the 2D-chamber with no line of sight to the viewports to prevent coating with strontium. The option of installing a dispenser perpendicular to the 2D-MOT was explored but rejected due to the high risk of coating the viewports.

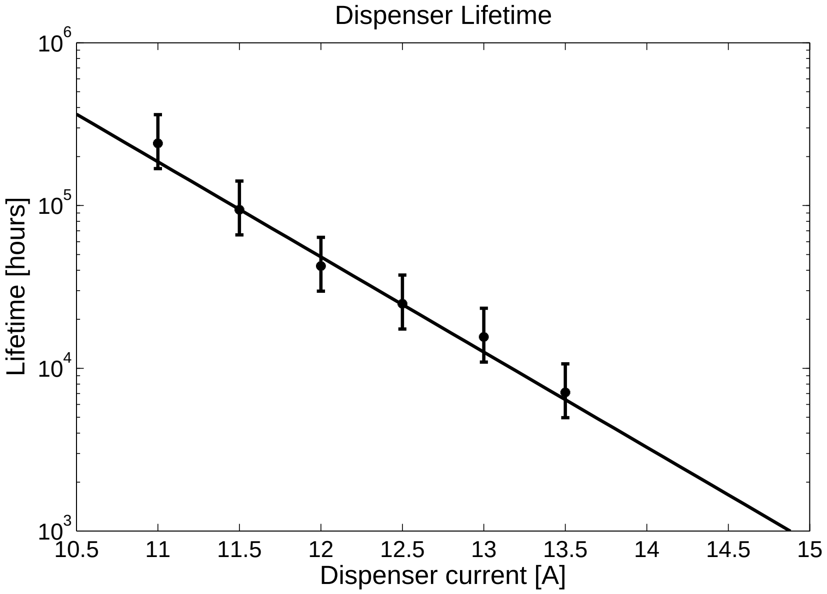

FIGURE 4.8: Lifetime of 100 mg dispenser.

To give us valuable insight into the operation of the dispenser the flux and velocity distribution of the emitted atoms was determined. The probe beam in the spectroscopy setup using the dispenser (see section 3.3.6) was shifted across the output to determine the angular dependence of the emitted atoms parallel to the slit. Contrary to the manufacturers estimations, who estimated the emitted atoms to have an angle of about 15°, the angular distribution was almost uniform with only a slight drop towards the edges visible. Due to the length of the slit the perpendicular distribution is considered nearly uniform.

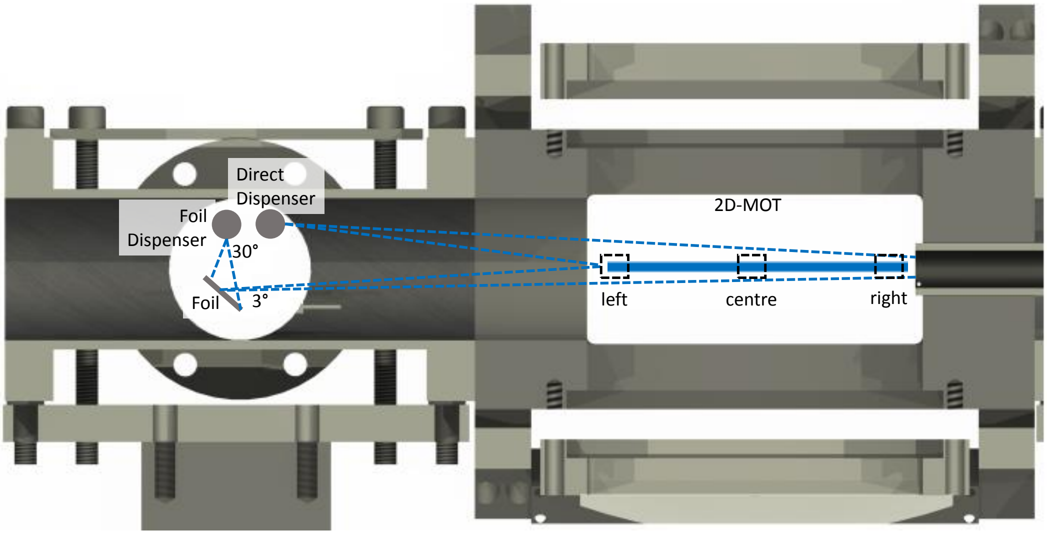

FIGURE 4.9: Geometrical alignment of dispensers and foil in vacuum chamber. One out of 10^4 atoms emitted from the foil dispenser will pass through the capture region of the 2D-MOT. The dispensers have no direct line of sight with viewports to prevent coating with strontium. The squares labelled left, centre and right show the measurement regions for figures 4.10 and 4.11

Measuring the absorption in the probe beam and assuming a uniform distribution, the flux of the dispenser was determined for various currents. From the calculated flux and the fill amount of 100 mg of strontium the lifetime of the dispenser was calculated for typical operational currents as shown in figure 4.8.

From geometrical considerations, shown in figure 4.9, the partial flux hitting the foil and passing through the 2D-MOT capture region can be calculated. One out of twenty atoms will hit the foil and, assuming an isotropic radiation of atoms from the foil, one out of 500 atoms emitted from the foil or the direct dispenser will pass through the capture region of the 2D-MOT. The operational temperature of the foil was determined by looking at the colour of the foil. With a current of 4-5 A a faint red colour was visible, which translates to a temperature[2] of 770±80 K. For a current of 3 A the temperature was estimated to 700±80 K.

---

[2] http://www.processassociates.com/process/heat/metcolor.htm

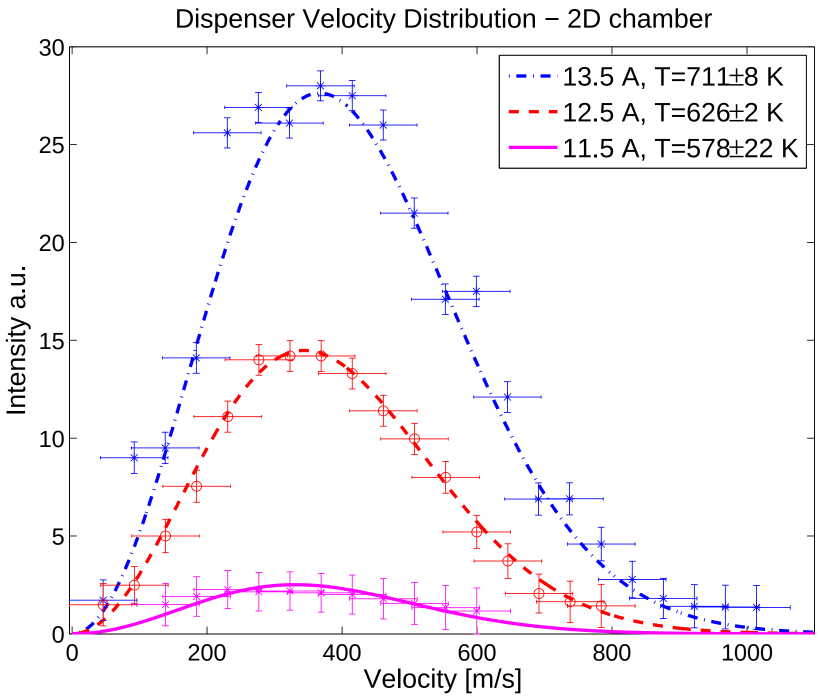

(a) Dispenser current varied between 11.5 A - 13.5 A

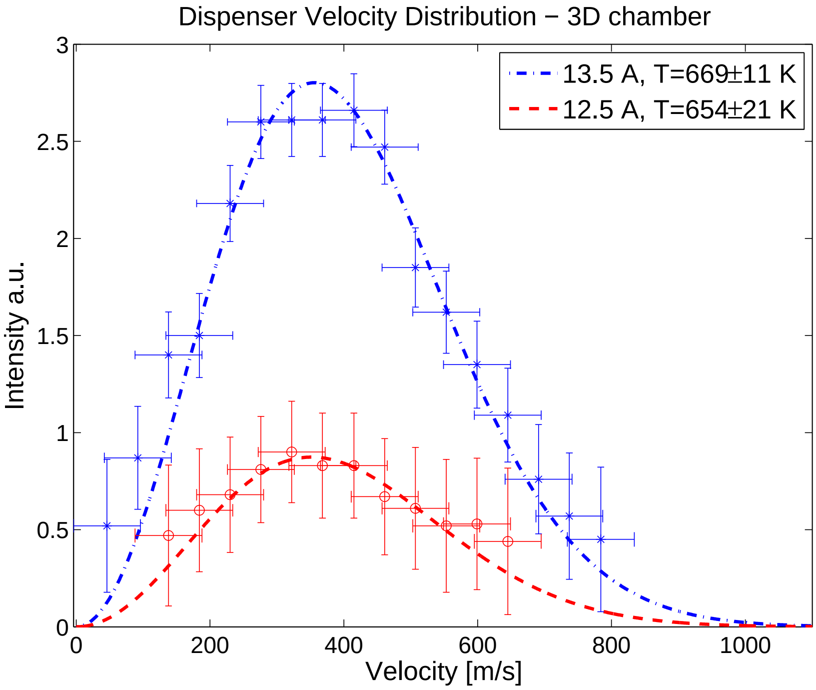

(b) 3D Chamber with dispener current varied between 12.5 A - 13.5 A

FIGURE 4.10: Velocity distribution of the dispenser for currents of 11.5 A, 12.5 A and 13.5 A in the 2D and 3D chamber with a fit of the thermal Maxwell-Boltzmann distribution. The measurements in (a) were taken on the side close to the dispenser of the 2D-MOT chamber and in (b) they were taken in the centre of the 3D chamber. The error in the velocity is due to the uncertainty in the frequency measurement and the error for the intensity is estimated from the goodness of the fit to the data.

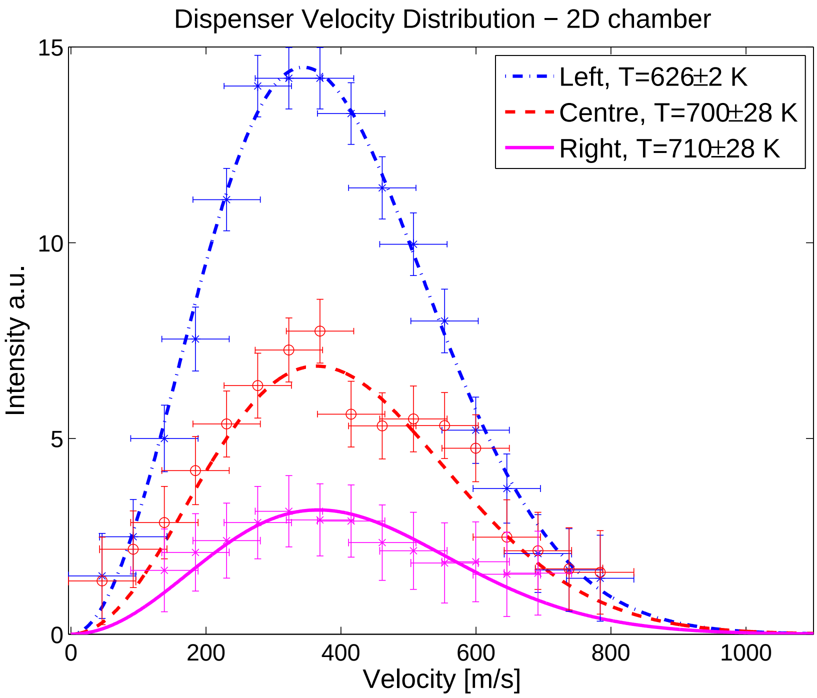

(a) Left, center and right hand side of chamber for a dispenser current of 12.5 A

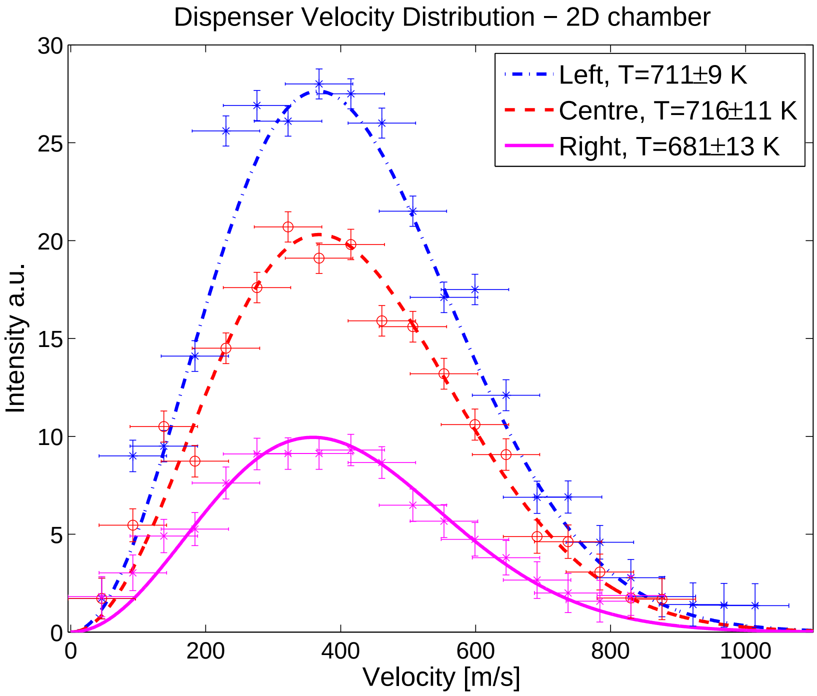

(b) Left, center and right hand side of chamber for a dispenser current of 13.5 A

FIGURE 4.11: Velocity distribution of the dispenser for currents of 12.5 A and 13.5 A in the 2D chamber with a fit of the thermal Maxwell-Boltzmann distribution. Measurements of the "left" being near the dispenser and on the "right" near the differential pumping stage. The error in the velocity is due to the uncertainty in the frequency measurement and the error for the intensity is estimated from the goodness of the fit to the data.

An important characteristic of the dispenser is the velocity distribution of the dispenser, which determines the amount of atoms I can capture. To measure the velocity distribution of the direct dispenser, a blue laser beam was shone along the symmetry axis of the 2D-MOT chamber. A camera was focussed on the beam and in a region of 5x5 mm the fluorescence of the beam was recorded for a detuning ranging from on resonance to 2 GHz. These measurement were taken at three positions in the 2D-MOT chamber, as shown in figure 4.9, and in the centre of the 3D-MOT chamber. The small measurement region allows us to look at the velocity distribution only in a small output angle of the dispenser.

The small angle of the atom velocity relative to the laser beam only causes a correction of less than 1% and is ignored. With the Doppler effect and the detuning the velocity currently resonant with the beam was calculated:

$$f_D = f_0 \left(1 + \frac{v}{c}\right) \Rightarrow v = \frac{\Delta f \cdot c}{f_0} \tag{4.4}$$

With f_0 being the atomic transition frequency, f_D the frequency shifted by the Doppler effect and $\Delta f = f_D - f_0$.

Figures 4.10 and 4.11 show the measured velocities at the four measurement points with the dispenser current being altered between 11.5 A and 13.5 A. The lines show a fit of the Maxwell-Boltzmann distribution, as defined in equation 2.11. We can see that the temperature corresponding to the velocity distribution is nearly constant along the entire 2D- and 3D-MOT region for a dispenser current of 13.5 A. The temperature at 12.5 A shows more variation which is due to the lower intensity leading to a higher uncertainty in the fit. The atoms leave the dispenser with a velocity distribution corresponding to a temperature of 694±20 K for a current of 13.5 A. If the current is lowered to 12.5 A and 11.5 A the temperature drops to 672±35 K and 578±22 K, respectively.

Effects of the expected nozzle effect are not visible in these measurements, with no deviation from the Maxwell-Boltzmann distribution showing within the measurement tolerances of ±50 m/s. The important velocity region between a few m/s to 80 m/s, which are the capture velocities of the 2D-MOT calculated in section 2.2.1, is not resolved in this measurement. So no conclusive evidence can be given here, if the nozzle effect is present or not, only that at velocities above 100 m/s no derivation from the expected thermal distribution is visible.

From figure 4.10 and 4.11 we can also estimate the relative atomic flux intensity, the number of strontium atoms passing through region of space per time, for the measured regions of the MOT chambers. The intensities shown in the two figures are to scale relative to each other. For a dispenser current of 13.5 A the atomic flux relative to the beginning of the 2D-MOT chamber is 74%, 33% and 10% in the 3D-chamber. For 12.5 A the relative flux is 54%, 22% and 6%. Especially in the 3D-chamber no flux would be expected without a 2D-MOT for the simple case of no collisions in the gas, since dispenser nor foil have direct line of sight into the 3D-chamber. Due to collision a flux is still observed. As expected the relative flux decreases from 10% to 6% with less dispenser current, suggesting a lower pressure causing less collisions.

4.1.4 Custom Viewports

Viewports allow optical access to the atoms in the vacuum chamber. They are the last optical element the laser beam passes before interacting with the atoms. For most optical components before hand beam deformations can be compensated, with for example the use of optical fibres.

In normal off the shelf viewports from vacuum companies the glass is welded into a CF steel flange. This welding process yields a big thermal strain on the glass, thus most of these viewports only have a surface smoothness of 4λ. Also requiring viewports for DN100 flanges and heating up to 200°C, for the initially planned coating of the vacuum chamber (see section 4.1.1), the pricing for these viewports increase exponentially. For these reasons I have decided to use custom optics with a custom vacuum seal. Our viewports have a surface smoothness of λ/10 and a thickness of 1 cm and 1.5 cm for the DN35 and DN100 flanges respectively.

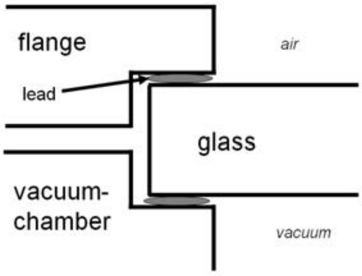

FIGURE 4.12: Schematic drawing of vacuum seal for 2D-chamber

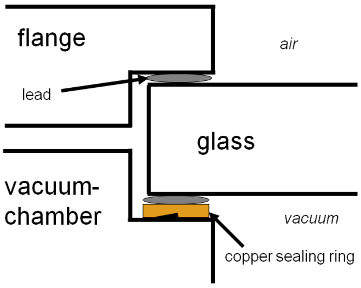

FIGURE 4.13: Schematic drawing of vacuum seal for 3D-chamber

The majority of custom vacuum seals uses the following principle: A soft wire is placed between the vacuum chamber and the glass and is then compressed. The softness of the wire fills out all the unevenness and the viewport is sealed. The most common material used is Indium. Indium has a Young's modulus of E≈ 10 GPa, which makes a it a very soft metal. Only needing a very small contact pressure, the risk of cracks on the glass is reduced. But indium has a melting point of 157°C, limiting the baking of the vacuum chamber to around 120°C. For the seals I am using lead [114, 115], which has a Young's modulus of E≈ 18 GPa, being not significantly more than indium, but still a lot less than e.g. copper with E≈ 117 GPa. The advantage of lead is that it has a melting point of 327°C. Hence bake outs of above 200°C are possible. This would have allowed the proposed coating and activation of the vacuum chamber with a getter material (see section 4.1.1).

For the 2D-Chamber I am using a solder lead wire[3] between glass and vacuum chamber (see figure 4.12) and the same wire again between glass and mounting flange. A lead alloy instead of pure lead was used to prevent corrosion. The second wire should distribute the pressure on the glass, thus preventing cracks. To maintain a constant pressure on the seal while baking four disc springs[4] are used in series. When the chamber and glass expand differently while baking due to the thermal expansion not being matched the disc springs will keep a constant pressure.

For the 3D-chamber a slightly different setup is used, because our chamber is not custom built. It has the knife edge of the CF flange. Now an annealed copper gasket is being placed between the lead seal and the knife edge (see figure 4.13). Here again disc springs are used to keep a constant pressure. To keep magnetic stray fields to a minimum, INCONEL® 718 was used as a spring material. This material can be baked up to 700°C and has a very low magnetic permeability. It's main usage is usually in gas-turbines, rocket motors or nuclear reactors. For the DN35 viewports four disc springs are used in parallel, resulting in a force of 1,3kN[5] at full disc deflection. For the DN100 viewports four disk springs are used in parallel resulting in a force of 2kN[6] at 68% deflection.

---

[3] Indalloy 165: 97,5% Pb, 1,5% Ag and 1% Sn with a melting point of 309°C; Indalloy Corporation of America

[4] X7CrNiAl17-7

[5] Manufacturer specification: Bauer Springs Limited

[6] Manufacturer specification: Bauer Springs Limited

To pre flatten the lead wire from 0.7 mm diameter to 0.3 mm a stamp with a pre cut groove was used. The screws where tightened to 2.5 Nm and 2 Nm for the DN35 and DN100 viewports respectively. After baking the screws had to be retightened to 2.7 Nm and 3.6 Nm respectively. On one DN35 and one DN100 viewport even after retightening small leaks in the lower $< 10^{-9}$ mbar range were left. Vacseal was used to seal these leaks.

With this sealing technique pressures of $< 10^{-11}$ mbar for the 3D-MOT chamber and $< 10^{-10}$ mbar for the 2D-MOT chamber measured by the ion pumps are achieved. The achievable low pressures show the suitability of lead sealing for custom viewports, when high bake out temperatures of above 120°C are required.

4.1.5 Quadrupole fields

For the operation of a MOT a magnetic field gradient is required to have a velocity selective deceleration force. For strontium field gradients of typically 45 G/cm (see section 2.2.1 and [93]) are required for the operation of the MOT. This is a considerably higher gradient than typically required in other cold atom experiments (for example Rubidium requires 15 G/cm [116]).

2D Permanent Magnets

The 2D-MOT requires a magnetic quadrupole field. Since this is the first setup with a strontium 2D-MOT I cannot revert to experience from previous experiments. Looking at experiments with similar atoms the magnet gradient typically has the same range as for the 3D-MOT. From simulations in section 2.2.1 estimating the expected atomic flux for the 2D-MOT a similar gradient is confirmed. Due to the larger beam diameters and limited available blue power a slightly lower gradient is favourable for optimum pre cooling of the atoms than in the 3D-MOT.

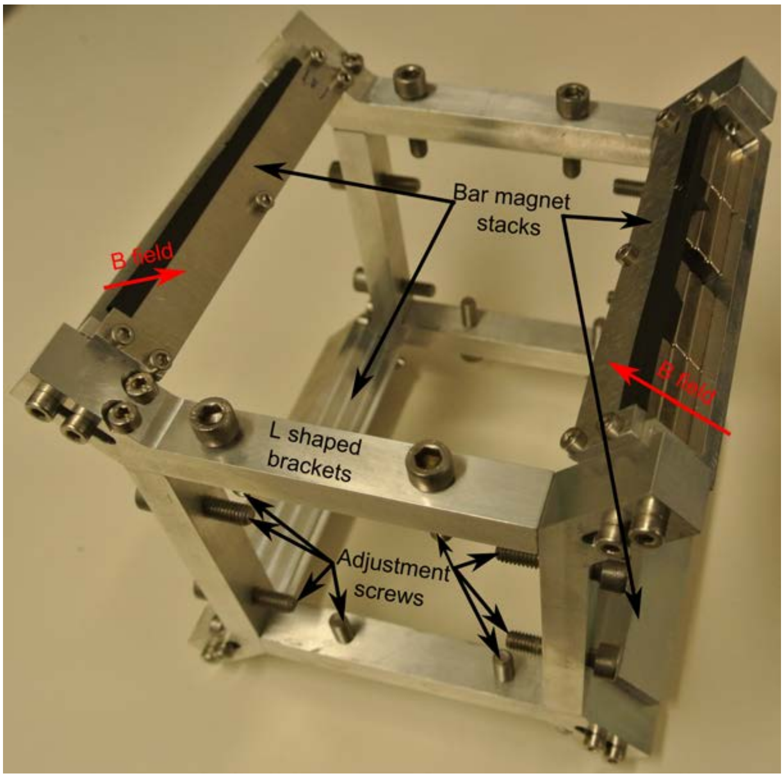

Figure 4.14: Photograph of the assembled permanent magnets. The magnetic field direction of the top two magnet assemblies is indicated.

Two types of coils and magnets were considered for generating the magnetic field for the 2D-MOT: One option was to use a similar design for the coils as used for the 3D-MOT (see next section). This would also allow a compact design, but would also require water cooling. Another option was the use of permanent magnets as has been done on an experiment with a lithium 2D-MOT [117]. Permanent magnets have the advantage of not consuming any power nor requiring additional cooling at the cost of very limited adjustability of the magnetic field strength.

As this setup can also be seen as a step towards the design of a Space-Optical-Clock the permanent magnet setup was pursued. With no power consumption and no required cooling, the permanent magnets offer great advantage over coils for space missions, since weight, power consumption and heat generation are of great concern.

Commercially available Neodymium block magnets with a dimension 25x10x5 mm are used. They have a measured magnetization of $6.3 \cdot 10^5$ A m^{-1} which is similar to the magnets used in [117]. Great reductions of magnetization were observed, when the magnets were not carefully handled by letting them snap to each other. The impact caused a loss of magnetization of up to 50%.

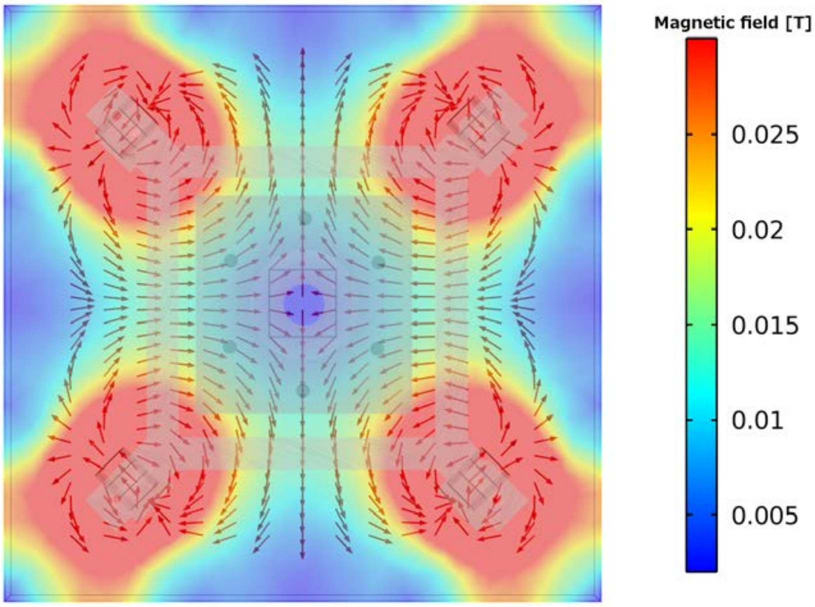

FIGURE 4.15: Schematic drawing of the geometry used to simulate the magnetic field of the bar magnets. The outline of the 2D-MOT vacuum and magnet components is overlayed in grey. The outside shape consists of the magnets and their mount as shown in figure 4.14 and the inside square is the vacuum chamber of the 2D-MOT. The red arrows show the direction of the magnetic field, whilst the colour coding of the background shows the field strength.

To determine the optimum position and number of magnets to generate the magnetic field gradient was simulated using finite element analysis in Comsol. A photograph of the magnets and their mount is given in figure 4.14 and a schematic drawing of the geometry used with the simulated generated field can be seen in figure 4.15. The outline of the 2D-MOT vacuum chamber is overlayed in grey in figure 4.15. The red arrows show the direction of the magnetic field and the colour coding of the background shows the field strength.

The lowest field gradient for the maximum capture velocity at an intensity of 2.5 mW/cm^2 is 4 mT/cm (see section 2.2.1). The simulations showed that the optimum combination to generate the required field consists of stacks of three bar magnets with four of these stacks being placed in parallel along the vacuum chamber.

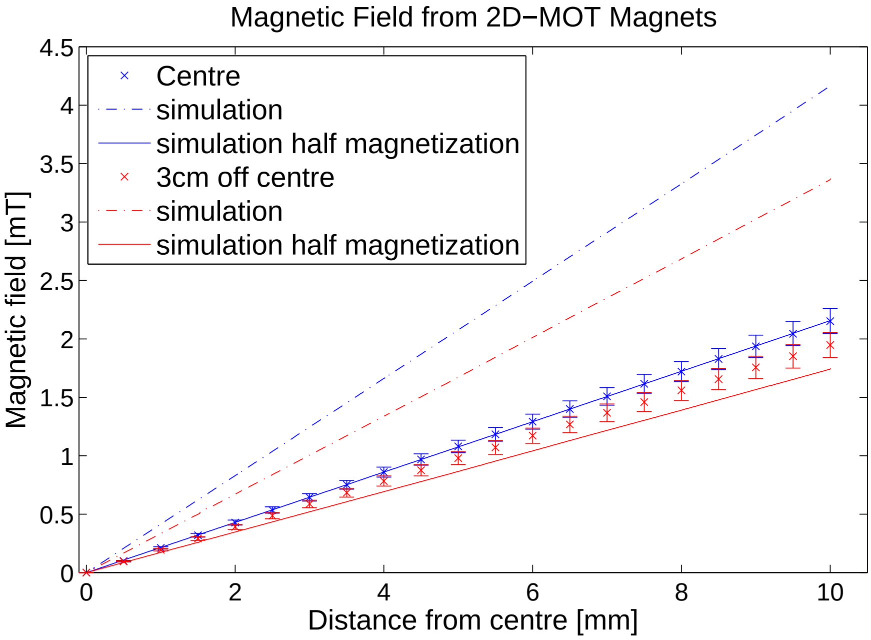

FIGURE 4.16: Measured and simulated magnetic field generated by permanent magnets for 2D-MOT. The x-position marks the position along horizontal axis of the magnets starting from the centre. Two measurements were taken at the position of the 2D-MOT. One at the centre and one three cm to one side. The simulation using finite elements analysis and an initially measured magnetization of $6.3 \cdot 10^5$ over estimates the measured gradient by a factor of two(dotted line). For the second simulation the magnetization was $3.3 \cdot 10^5$

The bar magnets are mounted in an aluminium tray, which clamps them tightly in place as can be seen in figure 4.14. The trays are mounted to the vacuum chamber using specially designed L shaped brackets in which they can be moved outward to adjust the magnetic field strength. The brackets are then screwed onto the vacuum chamber, allowing for adjustment of the magnetic centre to align the 2D-MOT with the differential pumping stage.

A plot of the simulated field is given in figure 4.16. The gradient is plotted along the axis of the cooling beam for two positions along the symmetry line of the magnets starting at the centre at 0 cm and going to 3 cm. Compared to the expected value of 4.2 mT at 1 cm distance, the measured field strength is 50% smaller at 2.1 mT. This difference can be attributed to losses of magnetization during assembly. Although great care was taken to avoid snapping the magnets together during assembly, it could not be completely prevented.

With the use of permanent magnets it is possible to achieve the magnetic field gradients required for strontium. They have shown to be a suitable replacement for coils at the limitation of very limited adjustability of the magnetic field. Just additional care needs to be taken during the assembly to prevent a loss of magnetization. If the required field gradient is known, the use of permanent magnets does not only save space and weight but is also a very cost effective solution, since no expensive power supplies are required.

3D Coils

To generate the quadrupole magnetic field for the 3D-MOT I have designed two coils with a new cooling system, which allows for efficient cooling at a reduced complexity compared to other designs with similar requirements.

The minimum distance and inner diameter of the 3D coils is defined by the dimensions of the 3D-MOT vacuum chamber. The coils are at a distance of 110 mm with an inner diameter of 55 mm. To calculate the required current for producing a gradient of 45 G/cm the coil is modelled as a single-turn coil with its radius being the average radius of the coil. The magnetic field on the symmetry axis of this coil can be calculated using the following formula derived from the Biot-Savart law:

$$B_Z = \frac{\mu_0}{2} \frac{n \cdot I \cdot R_C^2}{(R_C^2 + x^2)^{3/2}} \tag{4.5}$$

Where I is the current, n is the number of turns, R_C is the average radius of the coil and x is the distance from the coil along the symmetry axis. Taking the derivative and adding the second coil the field gradient can be calculated.

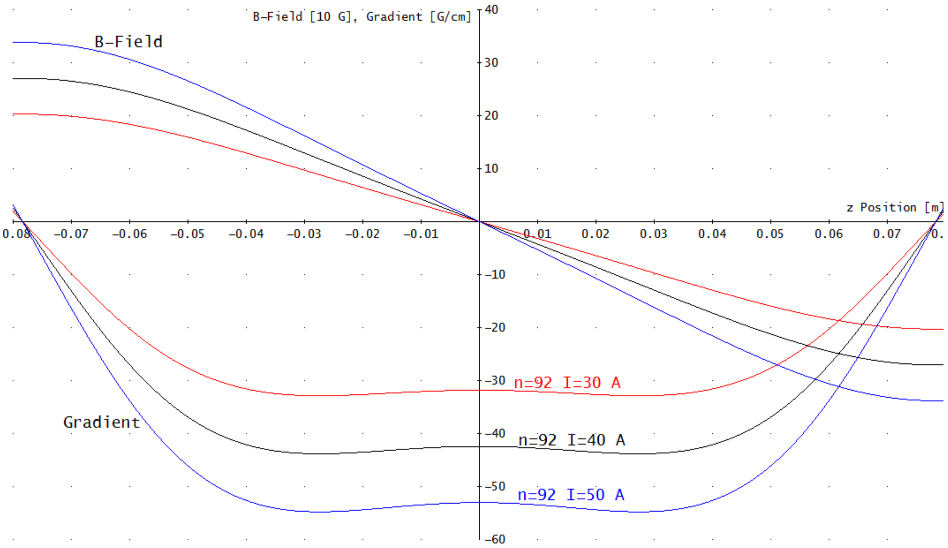

FIGURE 4.17: Calculated magnetic field strength and gradient for 3D-Coils. Field and gradient for 30, 40 and 50 A current is shown with 92 windings on the coil

A plot of the magnetic field gradient is given in figure 4.17. The magnetic fields and gradients are plotted for currents of 30 A, 40 A and 50 A with 92 turns giving a gradient of 32 G/cm, 42.5 G/cm and 53 G/cm respectively.

From figure 4.17 it can be seen that a total current (turns in a coil times current) of 4000 A is necessary to produce the required gradient for the 3D-MOT at the given coil dimensions. To build a coil with such a high current water or other liquid cooling is required. For the water cooling to be effective a good thermal contact needs to exist between the copper wire and the cooling fluid. In previous cold atom experiments various designs of water cooling have been implemented, which include hollow copper wire with water flowing through it or an encapsulated coil with water flowing around the copper

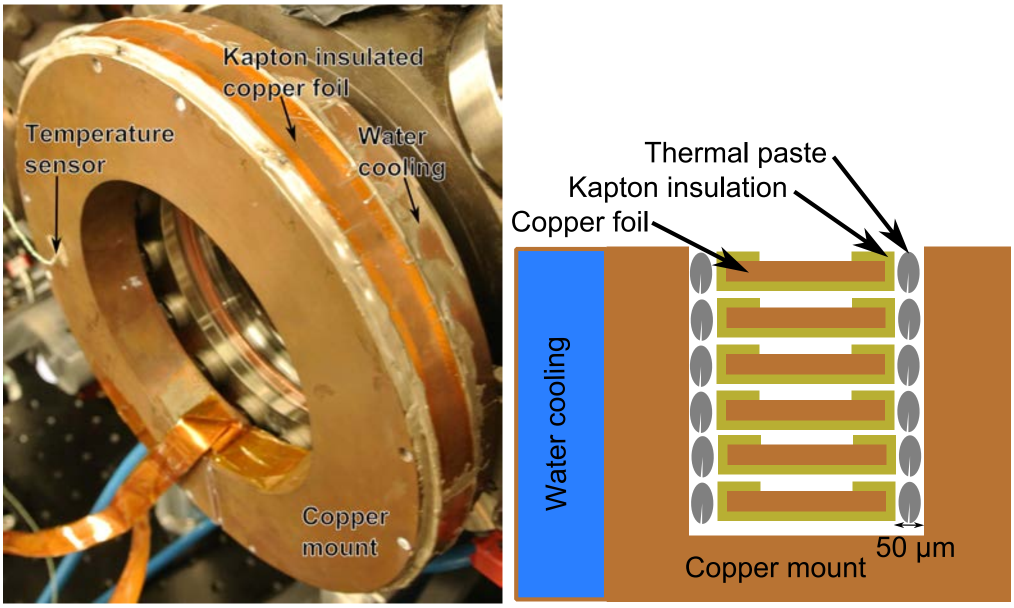

(a) Photograph of 3D-MOT coil (b) Schematic drawing of 3D-MOT coil

Figure 4.18: (a) Photograph of an installed 3D-MOT coil. (b) Schematic drawing of 3D-Coil setup (not to scale). The copper conductor (12.7 x 0.254 mm cross section)with Kapton insulation is thermally contacted by a thin layer of thermal paste to the mount, which is 100 μm wider than the cuffed copper conductor.

wire. These designs usually require complex setups and are suitable for even higher currents.

I have developed different a design, which still allows for sufficient cooling at a reduced complexity. In our newly developed design a Kapton insulated copper foil is wound in a machined-to-fit water cooled copper mount. The foil is 12.7 mm wide and 0.254 mm thick and is insulated with a 25 μm thick Kapton layer. The mount is only 0.1 mm wider than the foil and the walls are coated with thermal paste ensuring a good thermal contact. The copper mount has a water cooling channel on one side as can be seen in a schematic drawing in figure 4.18. In figure 4.2 a photograph of the wound coils attached to the 3D-chamber can be seen.

In figure 4.19 the temperature of a 3D coil is plotted for different currents. At the typical operational current between 30 A - 50 A the temperature stays below 60 °C. Critical temperatures near 100 °C are not reached for the required operational currents. The

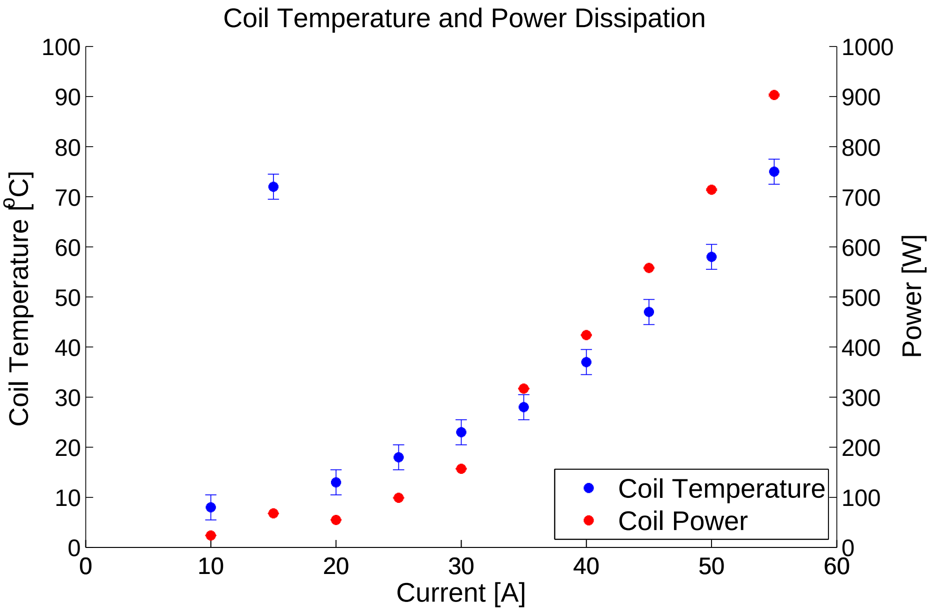

Figure 4.19: Temperature and power consumption of 3D coil for various currents. Temperature was measured using an installed thermocouple at the centre of the coil. For a current of 10 A and 15 A water cooling was switched off.

newly developed design has proven to ensure sufficient cooling for current of up to 55 A to have an optimal gradient for cooling and trapping of strontium in a 3D-MOT.

4.1.6 Quarter Waveplate Foil

In the 2D-MOT reflected cooling beams are used to achieve a higher intensity. If separate beams were used, half the intensity would be lost. The direction of the circular polarization of the reflected beam needs to be changed. To change the polarisation of the reflected beams for the 2D-MOT a new method is used. Usually the beam, which is much larger than the quarter waveplate, is recollimated by one or two lenses to a smaller diameter and then double passed through a $\lambda/4$ waveplate. This has the disadvantages of the beam being mirrored and passing through four additional lenses distorting the intensity profile.

Figure 4.20: Photograph of rectangular mirror for the 2D-MOT with foil laminated onto it.

We are using a quarter waveplate foil[7] which is directly laminated onto a rectangular mirror the size of the beam as is illustrated in figure 4.20. This has the advantage of the beam maintaining its profile compared to the usual setup using lenses, where the reflected beam is mirrored, and thus the atoms are seeing a more constant intensity of both beams. The foil is typically used in computer displays and is designed for the entire optical range. It has two crossing points in the optical range, where the quarter wave retardation is nearly optimal, with one of them being near 461 nm.

Since this foil is new to an optical clock setup the retardation of the foil was evaluated. To test the foil linear polarized light was passed through a polarizing beam splitter (PBS) and reflected off the mirror with the foil. A schematic of the setup is shown in figure 4.21(a). Depending on the angle of the mirror the light is transmitted or reflected in the PBS. With 9.7 mW of light after the PBS between 0.14 mW and 8.4 mW were reflected for an angle of 0° and 45° respectively as can be seen in figure 4.21(b). A reference quarter waveplate was showing power levels of 0.14 mW and 9.2 mW. The better maximum value can be attributed to the surface of the foil not being anti-reflex coated, thus $\sim$4% of the light will be reflected without a change. This shows that the

---

[7] ITOS WP140HE

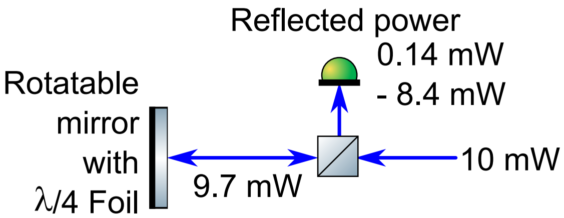

(a) Setup used to measure retardation of quarter waveplate foil

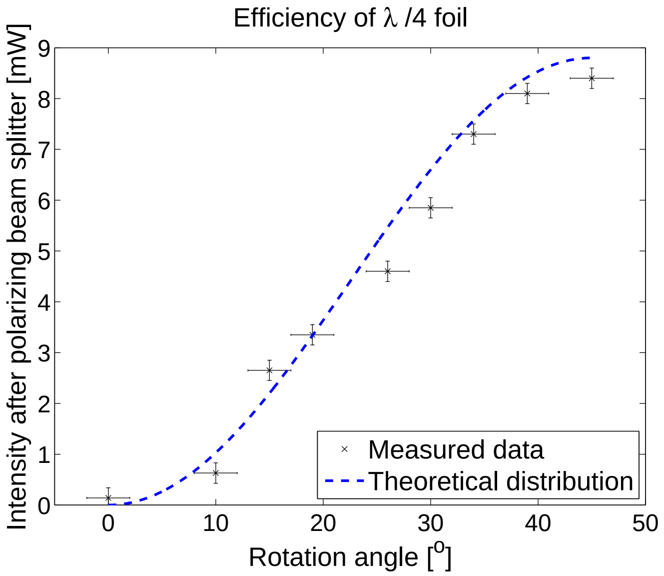

(b) Measured reflection of PBS

FIGURE 4.21: Measured reflection after polarizing beam splitter (PBS) for different rotation angles of mirror with quarter waveplate foil. Errors bars are defined by the measurement accuracy of the rotation angle of ±2° and laser power fluctuations of up to 0.2 mW.

new quarter waveplate foil has proven suitable in maintaining a better beam quality at nearly equal quarter wave retardation.

4.2 Experimental Control System

To control the experiment a computer controlled experimental control system is required. The computer control needs to have a repeatable timing with a resolution of less than a ms, be able to control several digital and analogue output channels simultaneously and be able to convert from the required units for the controlled device to a control voltage (for example MHz detuning for the AOMs to voltage or current for the coils to voltage).

For portability the control systems also needs to be of a compact size. The control system used in this experiment, which fulfils these and more requirements is introduced in section 4.2.1.

Further to the computer control system an imaging system is required to record and analyse the MOT. The imaging system needs to have a low noise to record images at low light levels from the MOT. In post-processing the system also needs to be able to correct for background lighting and calculate various parameters of the MOT, such as atom number and temperature. A detailed description of the imaging systems and its control program will be given in section 4.2.2.

4.2.1 Control Electronics

An embedded control and acquisition device from National Instruments is used as the control hardware. The control board has a Field Programmable Gate Array (FPGA) installed. The FPGA system offers a wide range of advantages over systems using pre calculated buffers for the outputs. The executing processor is installed on the board eliminating potentially slow or disrupted communication from the main processor to the output boards. The ability to execute commands with high bandwidth and low latency during operation allows for the potential implementation of feedback loops. This comes at the cost of increased programming effort required to run the FPGA. A control program already written for a different experiment in the group [118] was adapted to run on our system.

The FPGA control board[8] has a 400 MHz Freescale CPU with 128 MB of RAM and a 2M gate Xilinx Spartan-3 FPGA. It offers 110 digital input output (DIO) lines, 32 analogue

---

[8] National Instruments sbRIO-9632

input (AI) channels and 4 analogue output (AO) channels. With an add-on card 16 additional AO channels are available. The board is designed for high-volume OEM applications. This offers the benefits of having a well tested, integrated and compact board making it suitable for our portability needs. With the installed control program timings of 100 ns for the digital and 1 μs for the analogue channels are achievable.

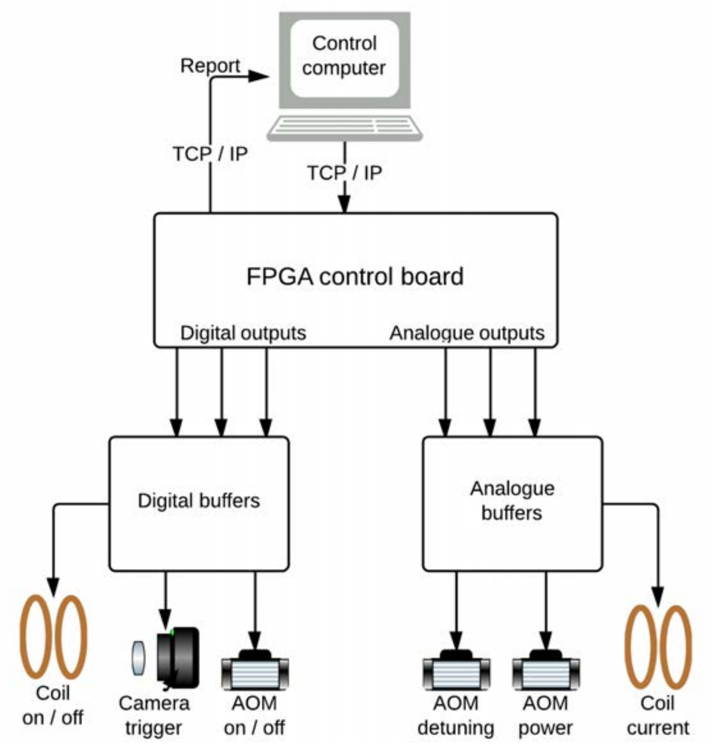

FIGURE 4.22: Flowchart of the setup of the control electronics. From top to bottom: Control computer running the control program. FPGA control board with 96 digital and 20 analogue channels. Digital and analogue buffers protect the board and ensure correct timing. Examples of equipment controlled are shown.

The FPGA control board continuously cycles through the experimental routine. Running the routine only on demand could cause thermal drifts due to experimental components being used in a non continuous way. The experimental routine is programmed on the control computer. To program the routine a table is used with a column for each time slot containing all the data for the individual outputs. The digital outputs can be either on or off and the analogue outputs can be set to a value with the option to linearly ramp to this value. Via a calibration file for the analogue channels any unit can be used as an input, which will be converted to the correct output voltage for the specific device. This can be for example a detuning frequency set for an AOM, which is converted into an output voltage controlling the voltage controlled oscillator (VCO).

From the control computer the routine data is uploaded to the FPGA control board via a TCP/IP connection through our lab network as illustrated in figure 4.22. Once the board has the data it begins to autonomously cycling the routine. After every cycle a report can be sent to the control computer or any computer on the lab network detailing the parameters used.

To protect the electronics of the control board and to maintain accuracy buffers are installed between the outputs and the experiment components. The buffer boards completely decouple the control board from the experiment to avoid ground loops as well as protect the hardware from voltage spikes or short circuits. Further information on the design of the buffer electronics can be found in [118].

4.2.2 Imaging System

To record images and measure properties of the MOT an imaging system is required. In our setup a PCO Pixelfly camera, which is connected to a computer running a LabVIEW control program, is used. The camera[9] has a resolution of 1392x1040 pixels with a quantum efficiency of 55% for 461 nm. The camera has digital temperature compensation instead of a space consuming thermo-electrical cooling unit, allowing exposure at low light levels with limited noise. Currently fluorescence imaging is used to image the MOT. A commercial zooming lens system is used, which has a reproduction scale of one pixel corresponding to a size of 36 μm at the MOT. An additional feature available on this

---

[9] PCO Pixelfly USB double shutter

camera is the double shutter mode. Although currently not required this feature allows a second image to be recorded a few microseconds after the initial image. This feature will be used when, at a later stage in the experiment, imaging is done via absorption imaging, allowing fringes on the detection beam to be subtracted from the original image before they can shift. The camera is connected to the computer via a USB connection.

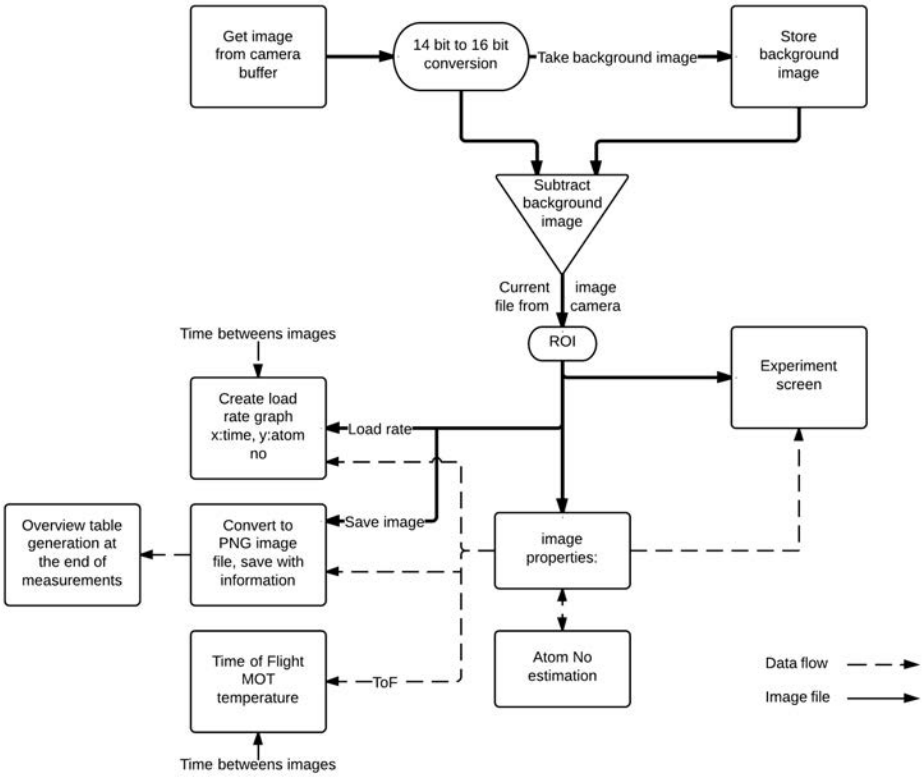

Figure 4.23: Flowchart of the processes in the imaging program. Going from image transfer from camera via image manipulation and analysis to output routines for saving images, loading rate and measure the temperature of the MOT

The camera control and analysis program is written in LabVIEW. It offers a variety of functions to analyse the images of the MOT ranging from determining its size, over measuring its atom number to determining the temperature of the captured atoms. In the following a brief overview of the programming will be given as can be seen in figure 4.23. The program downloads the currently stored image on the camera. The image file is in a 14 bit grey scale resolution format. To be able to work with it in LabVIEW it is converted into a 16 bit format. A background image with no atoms is taken on request, which is subtracted from the images to remove unwanted light. The main portion of light being subtracted is the scattering of the MOT beams in the viewports. Afterwards a region of interest can be selected from the image. The image file is then analysed by various sub routines. The sum over the x- and y-axis is taken and a Gaussian profile is fitted respectively from which the cloud width is calculated. By summing the intensity the illumination of the MOT is measured, which is the number of electrons counted by the camera from the exposure. These properties together with the background subtracted image are displayed on a separate screen on the experimental table to be used as an aid to adjust settings on the experiment.

Using the MOT illumination the number of atoms in the MOT can be estimated. For this the number of photons emitted per second from an atom in the MOT has to be calculated from the scattering rate of a single atom in a light field [62]:

$$\gamma_p = \frac{I/I_s \cdot \gamma/2}{1 + I/I_s + \left(\frac{2\delta}{\gamma}\right)^2} \tag{4.6}$$

Where $\gamma/2\pi$=32 MHz is the linewidth of the atomic transition, I_s =43 mW/cm^2 the saturation intensity, δ the detuning of the laser and I the intensity of the laser. In the case of the MOT all six beams have to be taken into account. Since the size of the MOT is small compared to the extend of the laser beams and the magnetic field, effects of the field gradient on the detuning do not have to be taken into account.

The fraction of the photons leaving the MOT and being detected on the camera has to be calculated using the distance of the camera lens from the MOT and its size:

$$fr = \frac{r_c^2}{4 \cdot r_{MOT}^2} \tag{4.7}$$

Where r_c is the radius of the camera lens and r_{MOT} is the lens distance from the MOT.

The final parameter required to calculate the atom number is the number of photons per second detected by the camera. For this the previously calculated MOT illumination N and the quantum efficiency of the camera of 55% for 461 nm are used to calculate the number of photons detected by the camera during the exposure time t. From this the photon flux on the camera per second n can be calculated:

$$n = \frac{N}{0.55 \cdot t \cdot T_L} \tag{4.8}$$

Where T_L=0.75 is the transmission of the lens system.

Comparing a laser beam at 461 nm with a measured power of 468 nW from a laser powermeter with the calculated power of 508 nW this method shows an error of less than 10%. Combining equations 4.6 - 4.8 the number of atoms in the MOT N_{MOT} can be estimated:

$$N_{MOT} = \frac{n}{\gamma_p \cdot fr} \tag{4.9}$$

This estimation can be seen as a lower limit of the number of atoms captured in the MOT. Effects such as the emission and reabsorption in the MOT, and the decrease in beam intensity as the MOT beams pass through the MOT are not taken into account. These effects, especially in larger MOTs, will decrease the number of photons emitted compared to the number calculated in equation 4.6 and will lead to an under estimation of the atom number.

The program offers three options to save the images and data. One option is to save the currently shown image and the measured data as an image file. When the program is stopped, all the measured data is additionally stored in a table for further analysis. Another option is to measure the load- or decay-rate of the MOT. In this mode a set number of images is taken at the maximum possible speed. The MOT illumination is plotted against the time between images to calculate the MOT lifetime. The third option is a time of flight measurement routine, which was implemented as part of a fourth year project to measure the temperature of the MOT.

In the near future the report generated by the FPGA control board (see section 4.2.1) will be received via TCP / IP and used to automatically trigger the imaging process and fill in the experimental parameters. This will allow one to automatically control the functions of this camera program by the control program as compared to having to manually enter the experimental parameters.

4.3 Summary

In this chapter I have presented the construction of the experimental apparatus for an atomic optical clock with strontium. The mobile vacuum chamber consists of two main chambers, one for pre-cooling strontium atoms in a 2D-MOT and one for the trapping and interrogation of these atoms. The chambers are connected via a differential pumping stage, which allows for a pressure difference of more than two order of magnitude and shields black body radiation emitted from the atomic source. The viewports were sealed with a special technique using lead permitting high baking temperatures and the use of custom high quality viewports.

The velocity distribution of atoms leaving the dispenser was characterised, suggesting a temperature of the dispenser between 620-700 K. With respect to a mobile setup and especially potential space applications, permanent magnets were installed to generate the magnetic gradient for the 2D-MOT. Also a compact experimental control system and imaging system were built to automatically operate the experiment.

Chapter 5

Magneto Optical Trapping of Strontium

In this chapter I will present the experimental results for a 3D-MOT with strontium. In the 3D-MOT section the influence of the laser beam intensity and the foil temperature on the number of captured atoms will be discussed as well as the use of the repumping lasers. In the following section I will discuss the effects of the 2D-MOT on the numbers of captured atoms in the 3D-MOT and validate the simulation for estimation of the flux of the 2D-MOT from section 2.2.1. A measurement of the number of trapped atoms and the lifetime of the MOT will be given.

5.1 3D-MOT

I have successfully trapped strontium atoms in a 3D-MOT, which was loaded either directly from the dispenser or from pre cooled atoms of a 2D-MOT. This section will focus on the characteristics of the 3D-MOT. For all the measurements presented in this section the 2D-MOT was not in operation and both repumpers were on, but the locking scheme, as described in section 3.4.1, was not active.

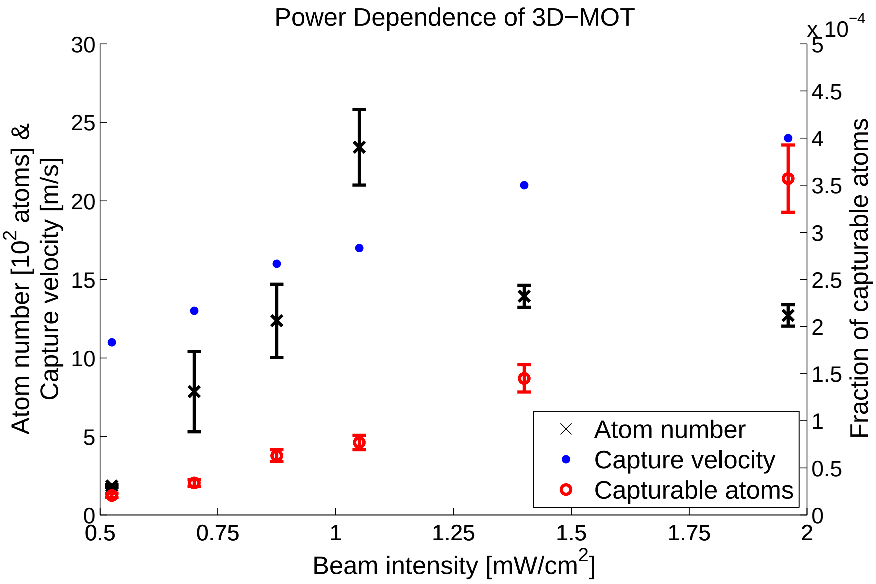

FIGURE 5.1: Atom number of the 3D-MOT with varying laser beam intensity. The atom number in the MOT can be seen as nearly constant down to an intensity of 0.75 to 1 mW/cm^2, with a significant drop of atom number below 0.75 mW/cm^2. The large increase in atom number for an intensity of 1.05 mW/cm^2 is attributed to a drift of the blue cooling laser. The capture velocity is the velocity a 1D-MOT would be able to capture with the given intensity, detuning of 20.5 MHz and a field gradient of 0.4 T/m using data from section 2.2.1. The fraction of capturable atoms is calculated from the capture velocity and the Maxwell-Boltzmann velocity distribution at 700±80 K (the temperature of the foil). Both repumpers were on and the MOT was loaded from background gas with a dispenser current of 15 A for this measurement.

To have as much power available for the 2D-MOT I investigated the dependence of the trapped atom number as a function of the laser intensity. From the simulations carried out in section 2.2.1 we would expect an increase of atom numbers proportional to the percentage of capturable atoms for higher laser intensities. Figure 5.1 shows the number of trapped atoms for laser intensities between 0.5 to 2 mW/cm^2. Instead of the expected increase, which should follow the capturable atoms, we see a nearly constant number of atoms for intensities between 0.85 and 2 mW/cm^2 and a drop below. The reason for this is unclear and was not further investigated. A potential reason might be the increased collisions within the MOT with an increasing atom number. Since a nearly constant atom number is achieved down to an intensity of 1 mW/cm^2, the 3D-MOT was operated with this intensity and the remaining available power was given to the 2D-MOT. The high atom number at an intensity of 1.05 mW/cm^2 is believed to be caused by a drift of the blue cooling laser. Since the new locking scheme was not yet implemented for these measurements (see section 3.3.6) a drift of up to 30 MHz was possible. This might have caused a higher fluorescence for which the atom number calculation was not adjusted accordingly. The main source for the errors in this image is the just mentioned drift of the blue cooling laser as well as the repumpers, which weren't stabilised during these measurements.

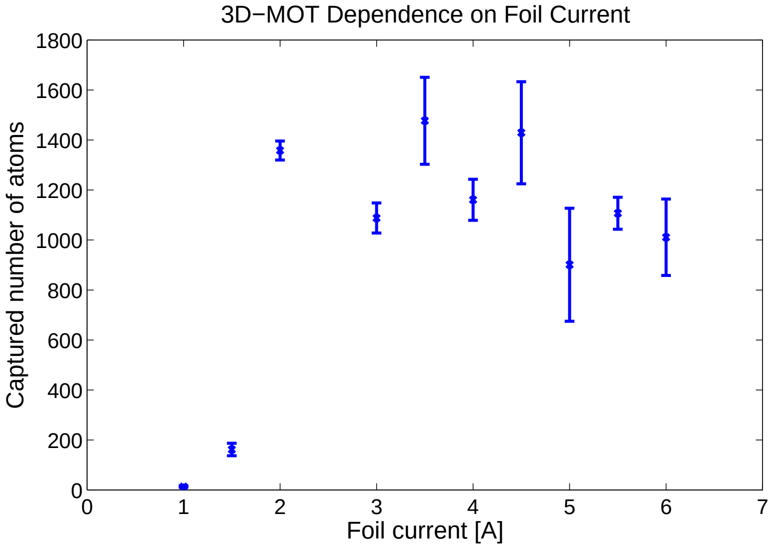

FIGURE 5.2: Atom number for 3D-MOT with varying foil current. Down to a current of 2 A the number of captured atoms in the 3D-MOT is nearly constant. The same experimental setting as in figure 5.1 were used with a beam intensity of I=2 mW/cm^2.

To find the optimum temperature of the foil, its current was varied between 1-6 A. Figure 5.2 shows the number of captured atoms in the 3D-MOT (see section 4.1.3 for further information on the dispenser-foil setup). For very low currents between 1-2 A only a small number of atoms is captured, due to the temperature of the foil being too low to fully evaporate the atoms. Between 2-6 A a nearly constant amount of atoms is trapped in the MOT. The increased temperature and thus higher velocities of the atoms for higher currents seems to be compensated by the increase in flux of atoms emitted from the foil. For most measurements a foil current of 3.5 A was chosen, which lies in the centre of the measured plateau.

5.1.1 Repumpers

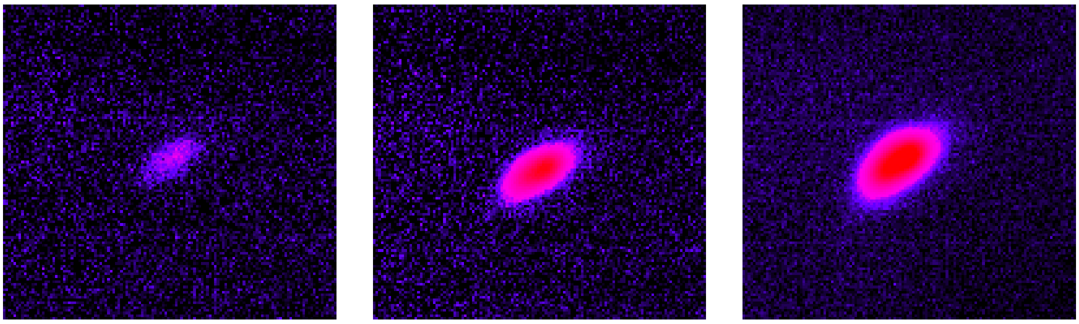

(a) 707 nm off - 679 nm off (b) 707 nm on - 679 nm off (c) 707 nm on - 679 nm on

FIGURE 5.3: 3D-MOT size for no (a), only 707 nm (b) and both repumpers (c) on. With a respective atom number of 47 ± 5, 322 ± 29 and 1055 ± 95 atoms. Images are to scale. The parameters are the same as in figure 5.1 with an intensity of I=1.5 mW/cm^2.

The $^1S_0 -^1 P_1$ cooling transition is not perfectly closed due to a decay channel to the meta stable $5s5p^3P_2$ state with a branching ratio of $2 \cdot 10^5$. For a detailed discussion see section 2.1. Unlike in alkaline atoms, the use of a repumper is not essential for the operation of a MOT, as can be seen in figure 5.3(a). With the use of the repumpers the number of trapped atoms in the MOT can be considerably increased. Figure 5.3 shows images of the MOT intensity and size with (a) no repumpers present, (b) only the 707 nm repumper on and in (c) both repumpers on. A relative increase of a factor of 6.8±1.3 for trapped atoms with the first repumper on and a further increase of a factor of 3.3±0.7 with both repumpers on can be seen. In total 23 times as many atoms are captured in the 3D-MOT with the repumpers. This increase is a factor of two larger than the previously reported one order of magnitude increase in other experiments [93, 119]. With our experiment having a lower background pressure, due to the use the differential pumping stage compared to a Zeeman slower, less collisions with the background gas

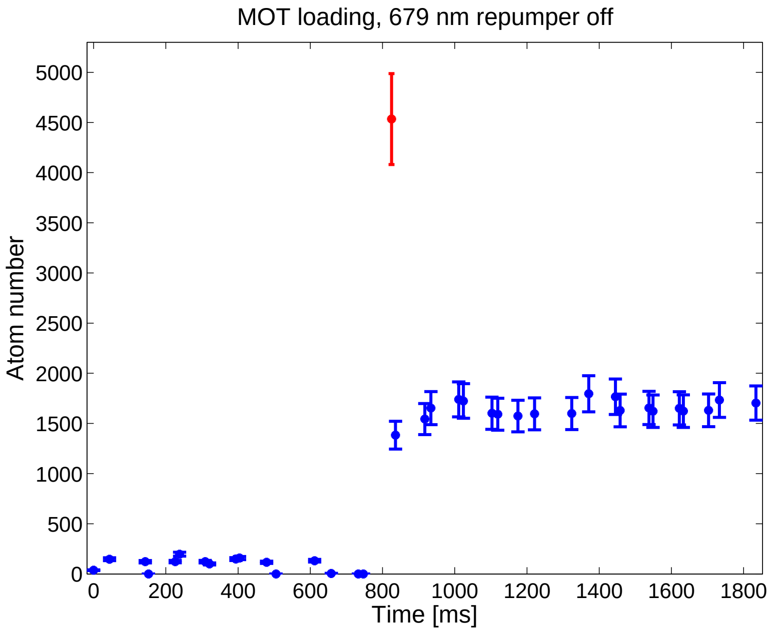

FIGURE 5.4: Number of atoms in the 3D-MOT with the 679 nm repumper off showing the loading of the 3D-MOT with the 707 nm laser being switched on at 750 ms. The spurious data point shown in red is believed to be caused by a false fit on the camera program during the switching on of the repumper. For these measurements the 2D-MOT was on and the experimental parameters were the same as in figure 5.8.

lead to a longer lifetime of the atoms in the MOT and one would expect a larger influence of the repumpers on the atom number.

The loading time of the 3D-MOT with only the 707 nm repumping laser on is shown in figure 5.4. The number atoms in the MOT are determined by the camera program (see section 4.2.2), with an average cycle time between images of 50 ms. The loading times of the MOT with none of the repumpers active were too fast to be captured with the camera program. The expected time an atom is captured in the MOT with only the 707 nm repumper on is primarily limited to the average time after which the atom has decayed to the metastable $5s5p^3P_3$ state, from which the 679 nm repumper should remove it. From the scattering rate given in equation 4.6 and the branching ratio we can estimate the expected lifetime.

For the measurement shown in figure 5.4 we get a scattering rate of $\gamma_p/2\pi = 12{\cdot}10^6$, with I=$6 \cdot 1$ mW/cm^2 for six beams and a detuning of $\delta/2\pi$=20.5 MHz. Taking into account the branching ratios of $1/(2 \cdot 10^5)$ from the main transition, 1/3 into the $5s5p^3P_2$ state and 1/9 into the $5s5p^3P_0$ state from the $5s6s^3S_0$ state [40], which means that on average the atom will be in the $5s5p^3P_0$ state after an average of $8.1 \cdot 10^6$ photon absorptions. Combining this with the scattering rate we get an estimated lifetime for an atom in the 3D-MOT of 110 ms, since once it is in the $5s5p^3P_0$ state with only the 707 nm repumper on it's not resonant to any light any more.

Figure 5.4 shows the number of atoms in the 3D-MOT before and after switching on the 707 nm repumping laser at 750 ms. After 100 ms to 200 ms the MOT is saturated. The atom number in the MOT is now limited by atoms falling into the $5s5P^3P_0$ state. The time scale is in the range of the expected 110 ms.

5.2 2D-MOT

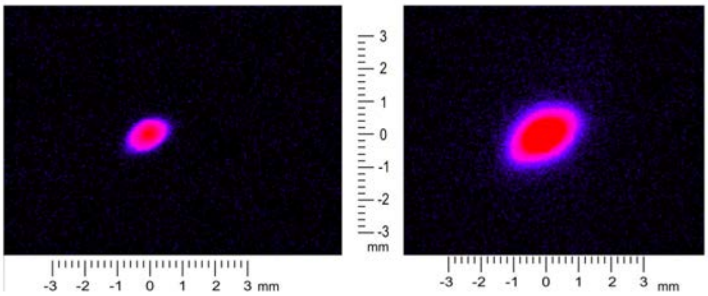

FIGURE 5.5: Left: 3D-MOT without 2D-MOT; Right: 3D-MOT with 2D-MOT; Dispenser at 12.5 A, both repumpers are on, 8 mW and 1 mW power per beam and a detuning of 2.5 MHz and 25 MHz for the 2D- and 3D-MOT respectively. The intensity is colour coded ranging from black for low intensities over blue to red for high intensities.

In this experiment I have successfully precooled strontium atoms in a 2D-MOT configuration with an observed 11 fold increase in the number of trapped atoms in the 3D-MOT as shown in figure 5.5. Due to a limited power available from the frequency doubling cavity of only 120-140 mW during these measurements, the configuration of the 2D-MOT setup was slightly altered. The fibre between the 2D-module (see section

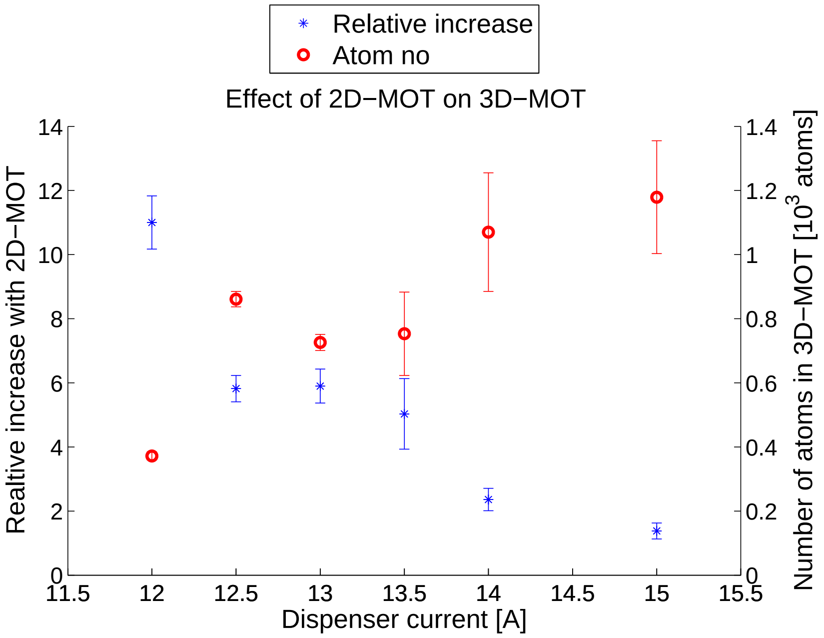

Figure 5.6: Effect of the 2D-MOT for various dispenser currents. A clear increase in the effect of the 2D-MOT is visible for lower dispenser current, but the absolute number atoms captured in the 3D-MOT increases with a higher dispenser current. The bigger atom no seen for a value of 12.5 A current is probably caused by the repumpers running at a better frequency. For this measurement both repumpers were on, a power of 5 mW and 1 mW per beam was available and a detuning of 2.5 MHz and 25 MHz for the 2D- and 3D-MOT respectively with a foil current of 3 A. For the measurement at 12 A the foil current was increased to 4.5 A.

3.5) and the 2D-MOT telescope was omitted and the beam was guided in free space to the 2D-MOT, having 80% more power available at the acceptable cost of a slightly lower beam quality. The shape of the beams in the 2D-MOT was changed from an 8x1 cm elliptical beam, which would have had an intensity of <1 mw/cm^2, to beams with 2 cm diameter. These measures allowed a power of up to 8 mW per beam and an intensity of 2.5 mw/cm^2.

Figure 5.6 shows the relative and absolute increase of the atoms captured in the 3D-MOT after precooling atoms in the 2D-MOT with varying dispenser current, which had a power of 5 mW per beam. The graph shows a linear decrease in the effect of the 2D-MOT for lower dispenser currents. It ranges from only less than doubling the atom number in the 3D-MOT with the dispenser at 15 A to an 11 fold increase with

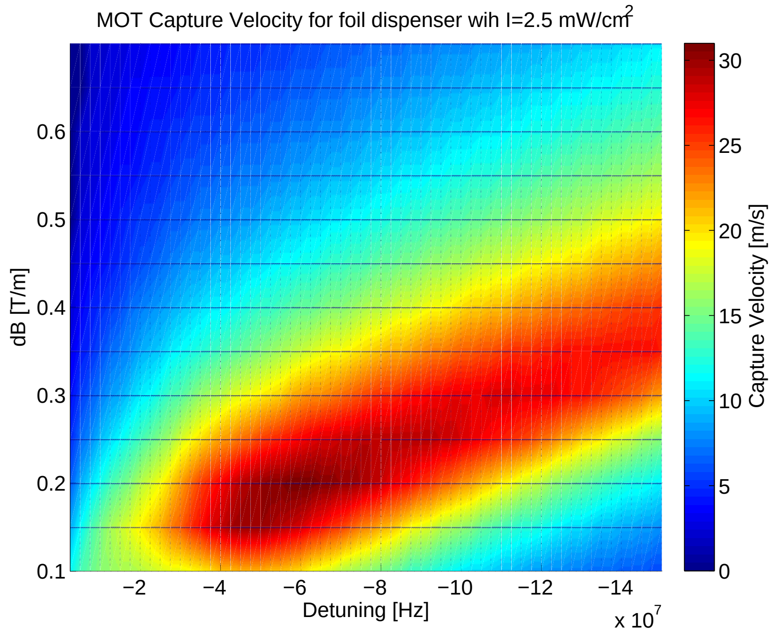

FIGURE 5.7: Plot of the capture velocity of the 2D-MOT in the modified configuration of only 2 cm long beams. The detuning was varied between $\delta/2\pi$=0 MHz to -150 MHz and the magnetic gradient from dB=0.1 T/m to 0.7 T/m. The laser intensity was I=2.5mW/cm2. The maximum capture velocity is achieved for a detuning of $\delta/2\pi$=-50 MHz and a magnetic gradient of dB=0.2 T/m.

the dispenser being at 12 A. The number of captured atoms in the 3D-MOT shows a linear behaviour up to currents of 14 A. The decreasing effect of the 2D-MOT with higher dispenser currents is believed to be caused by collisions of pre cooled atoms with the background gas. With the flux of the dispenser increasing by almost two orders of magnitude from 12 A to 14 A, the background collisions become increasingly dominant. The strange value in figure 5.6 for a current of 12.5 A of the dispenser is likely caused by a drift of the cooling laser during this measurement since the new spectroscopy, as described in section 3.3.6, was not yet implemented for these measurements. The main source of the errors are the drifts of the cooling laser as well as the repumping lasers.

Using the simulation tool introduced in section 2.2.1, we can estimate the expected flux of the 2D-MOT in this configuration. Figure 5.7 is showing the maximum capture velocity of the 2D-MOT in this configuration for magnetic field gradients between dB=0.1 T/m to 0.7 T/m and detunings between $\delta/2\pi$=0 MHz to -150 MHz. In this configuration the maximum capture velocity of 30 m/s is achieved for a magnetic field gradient of dB=0.2 T/m and a detuning of $\delta/2\pi = -50$ MHz. At dB=0.25 T/m, the magnetic field gradient produced by the permanent magnets, the optimum detuning is at $\delta/2\pi = -60$ MHz. The maximum flux of the 2D-MOT was achieved for a low detuning of $\delta/2\pi$=-2.5 MHz. When increasing the detuning to $\delta/2\pi$=-50 MHz only a small drop in atoms was observed in the 3D-MOT. Above this value the AOM caused a considerable loss of laser power. This is considerably lower than the expected value. Further investigations are required to gain more insight into this behaviour.

With carefully optimizing every step along the beam path I was able to increase the power per 2D-MOT beam to 8 mW. Figure 5.8 shows intensity colour coded image of the achieved 3D-MOT. The dispenser was at a current of 14 A and the 2D-MOT had a detuning of $\delta/2\pi$=-2.5 MHz. With a detuning of $\delta/2\pi$=-20.5 MHz for the 3D-MOT and using equation 4.9 the number of atoms in the 3D-MOT can be estimated to be $4 \cdot 10^5 \pm 0.4 \cdot 10^5$ atoms.

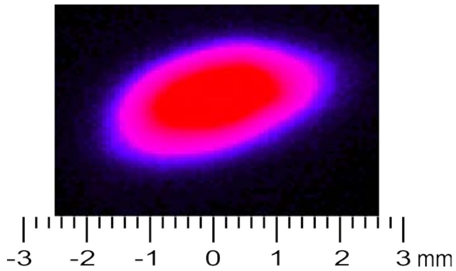

FIGURE 5.8: False colour image of 3D-MOT. For this measurement the 2D-MOT was in operation and both repumpers were on. The field gradient was at 0.2 T/m and the detuning was set to 20.5 MHz. The dispenser is at a current of 14 A.

By setting the exposure time of the camera to 50 ms, being just enough to get a good intensity fit, the lifetime of the 3D-MOT was determined. Figure 5.9 shows a plot of the loading and decay curve with a limited exponential growth fit. By blocking the reflected beam from the 2D-MOT, blowing away all the atoms, the flux of atoms from the 2D-chamber was effectively lowered to zero, allowing the measurement of the decay of the

3D-MOT. The jump visible at an atom number of $9 \cdot 10^4$ is believed to be caused by a problem in the camera program. It is up to now unclear what causes this consistently appearing error at the same atom number. From the fit the lifetime of the MOT was calculated to be τ=1/b=5.5±0.6 s. This is considerably higher than typical lifetimes of 0.2 s - 0.5 s reported in other strontium experiments [119, 120]. The increased lifetime can be attributed to two main factors. One is the low atom number in our MOT, limiting collision induced losses [119, 121]. The other one is attributed to the good vacuum pressure combined with a low residual flux from the 2D-MOT chamber, which causes less losses due to collisions with the background gas.

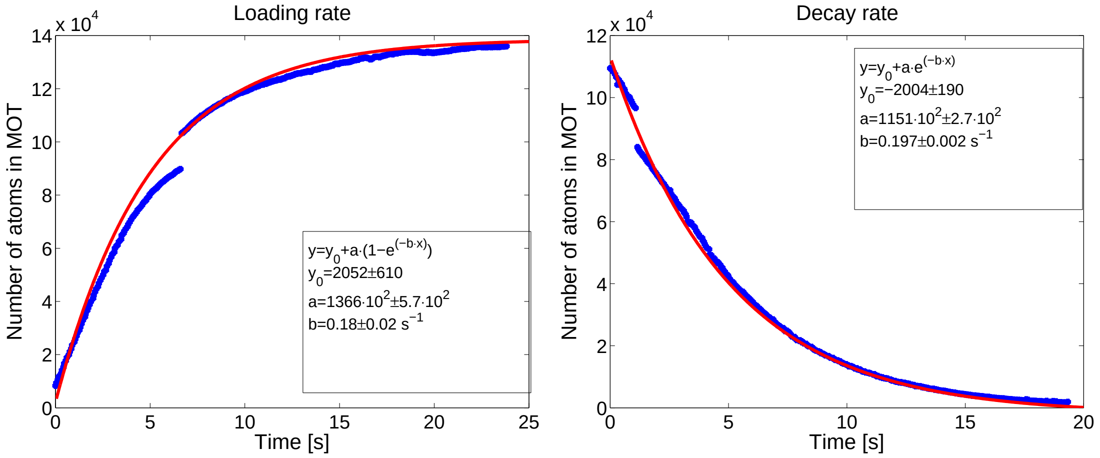

(a) Loading curve

(b) Decay curve

FIGURE 5.9: 3D-MOT (a) Loading of 3D-MOT (b) Decay of 3D-MOT. The blue curve shows the measured atom number. The red curve is a limited exponential growth or decay fit to measured data with the fit parameters given in the inset. The jump at $9 \cdot 10^4$ atoms is caused by an error of the camera program. Experimental parameters are the same as in figure 5.8.

Following the same calculations as in section 2.2.1 and using the calculated maximum capture velocity of figure 5.7 the expected flux of the 2D-MOT in this configuration can be estimated. The estimated flux is plotted in figure 5.10 for dispenser currents between 12 A to 14 A ranging from $(1 + 0.3 - 0.5) \cdot 10^4$ atoms/s to $(1.4 + 0.5 - 0.7) \cdot 10^5$ atoms/s respectively.

Using the from figure 5.8 calculated atom number of the 3D-MOT of $4 \cdot 10^5$ atoms and the measured loading time of 5.5 s, I have measured a loading rate of $1.75 \cdot 10^4 \pm 0.3 \cdot 10^4$ atoms/s. With the refined alignment for this measurement an increase in atom number with the 2D-MOT on of a factor of eight was visible. Taking this into account we can assume as a good estimate that all of the atoms trapped in the 3D-MOT were pre cooled in the 2D-MOT. This allows us now to compare the measured loading rate to the simulated flux of atoms from the 2D-MOT. Comparing the measured flux to the estimated flux of $(1.4 + 0.5 - 0.7) \cdot 10^5$ atoms/s our model is over estimating the flux of the 2D-MOT by a factor of eight. Considering the limitations of this model, mainly having not taking into account any collisions, the estimated order of magnitude for the flux can be seen as a good estimate.

To compare the simulation to our experiment at lower dispenser currents the previously calculated loading rate needs to be extrapolated, since no measurement data with the improved alignment is available for lower dispenser currents. Using the linear relationship of the number of atoms captured in the 3D-MOT in dependence of the dispenser current from figure 5.6, we can extrapolate the atom number of the 3D-MOT for a current from 12 A and 13.5 A. Combining these with an observed similar loading time of the 3D-MOT for different currents, we get an atomic flux of $1.1 \cdot 10^4 \pm 0.3 \cdot 10^4$ atoms/s and $0.7 \cdot 10^4 \pm 0.6 \cdot 10^4$ atoms/s for dispenser currents of 13 A and 12 A, respectively.

Between a dispenser current of 12-13 A the simulated flux shows a good agreement with the extrapolated flux of the 2D-MOT. The changing agreement is due to the linear dependence of the simulation on the dispenser flux, which increases exponentially with current. While the measured flux only shows a linear dependence on the dispenser current.

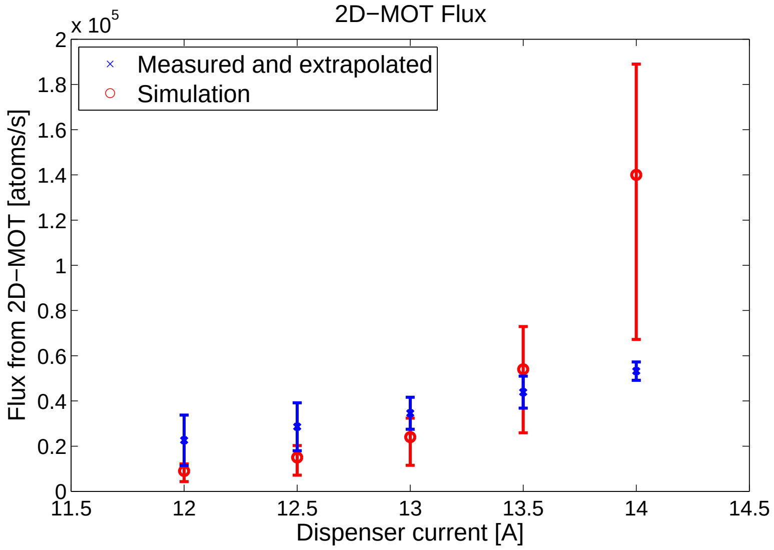

Figure 5.10: Simulated and measured flux of atoms from the 2D-MOT for dispenser currents between 12-14 A. The flux for 13.5 A to 12 A was extrapolated from the 14 A value using the linear relationship from figure 5.6. For the simulated flux the same method as in section 2.2.1is used. It shows an exponential increase due to the exponential increase of atoms emitted from the dispenser with increasing current.

Using the good agreement of the simulated flux up to 13.5 A of the dispenser and assuming the planed beam size of 8 cm and with an intensity of 5 mW/cm^2, as the current state of the doubling cavity will provide, we can expect a flux of up to $1.2 \pm 0.4 \cdot 10^6$ atoms/s with the dispenser at a current of 13.5 A, as calculated in section 2.2.1. When at a later stage a dispenser at 45° is installed, with appropriate shielding to protect the viewports, a flux of up to $8.2 \pm 2.5 \cdot 10^8$ atoms/s can be expected. If the laser intensity is increased close to saturation intensity up to several 10^9 atoms/s seem feasible. Compared to a typical reported flux between $8 \cdot 10^8$ and $4 \cdot 10^{10}$ atoms/s [9, 86, 87] in other strontium experiments using Zeeman-slowers, our 2D-MOT configuration will be able to deliver a similar order of magnitude of atomic flux with enough laser intensity.

5.3 Summary

In this chapter I have discussed our results on the successful trapping of strontium. The atoms were pre cooled in a 2D-MOT with an achieved loading rate of $1.75 \cdot 10^4 \pm 0.3 \cdot 10^4$ atoms/s for the 3D-MOT. In the 3D-MOT a total of $4 \cdot 10^5 \pm 0.4 \cdot 10^5$ atoms was captured. The effect of the dispenser current on the number of captured atoms in the 3D-MOT was investigated, showing a decreasing effect of the 2D-MOT for higher currents which was attributed to collisions in the 2D-MOT with the background gas.

Chapter 6

Conclusions and Outlook

The aim of this thesis was the development of a mobile experiment for trapping of strontium, which can be used as a clock. Much has been achieved in the last four years. Our lab has developed from a construction site to an experiment demonstrating the first 2D-MOT for strontium. For the cooling and trapping of strontium I have built and characterized the modular and mobile laser systems. This includes a frequency doubled master oscillator power amplifier system for the main cooling transition. The constructed monolithic frequency doubling cavity can generate 300 mW of blue light and has proven to be a stable setup suitable for a mobile system. The two modular repumping lasers were successfully locked to their respective transition in strontium with the use of a dc discharge.

I have constructed a mobile vacuum apparatus with a two chamber concept, allowing for efficient loading and offering an experimental chamber with low pressure and shielding for black body radiation from the strontium source, which is one of the main limitations for current strontium clocks.

The first magneto-optical trapping of strontium using a 2D-MOT as a source of pre-cooled has been demonstrated with this experiment. $4 \cdot 10^5 \pm 0.4 \cdot 10^5$ atoms were captured in the 3D-MOT with a lifetime of 5.5 s.

Over the last year great improvements have been made to the system. A fourfold increase in laser intensity is now available for the 2D-MOT with the output power of the cavity having been doubled from initially 140 mW and by the bypassing the 2D distribution module, saving the losses of a fibre coupling. The change of the repumping diodes and their stabilisation to the atomic transition will enable us to have more stable experimental parameters. With careful planing to protect the viewports from coating with strontium the addition of a 45° dispenser is being prepared to benefit from the full potential of the 2D-MOT. With these improvements I expect to see a substantial increase in atomic flux from the 2D-MOT and in the number of trapped atoms in the 3D-MOT, showing the suitability of a 2D-MOT for the operation of an atomic optical clock with neutral strontium atoms. Combining the simulation in section 2.2.1 and the results of section 5.2 a flux in the order of 10^8 atoms/s can be expected.

In the near future a second frequency doubling cavity should further increase the intensity and provide a significant increase of the expected flux of the 2D-MOT, allowing for fast loading of the 3D-MOT, which is necessary for short cycling times required to reduce the uncertainties of a clock.

With the implementation of the second stage red MOT in the near future, the atoms will be cooled enough to be loaded into the optical lattice. The clock laser, which will probe the clock transitions was developed in parallel in our group.[122]

On a broader view, strontium offers attractive potential for laser cooled experiments, benefiting from its versatile level structure, whilst the easily accessible wavelength allows for simpler setups. strontium is showing its potential in the fields of ultra-cold gases [123], cold molecules [124] and in the studies of Rydberg atoms [125].

Optical lattice clocks with strontium have now an agreement in the $< 10^{-15}$ level, but much work lies ahead to repeatedly reach uncertainty levels at the 10^{-17} level. The biggest challenge remaining is the further detailed study of black body radiation effects. But also collisions in the optical lattice are not to be neglected, where the step towards a three dimensional blue detuned lattice could help resolve current issues, which is planed to be installed in this experiment.

With new mobile optical clocks now emerging, such as the space optical clock project (SOC)[70], a range of exciting new applications are coming within reach. The European Union wide project SOC is targeted at harnessing unique opportunities offered by space.

Looking in the metrology field, many precision experiments are showing great progress with consistently decreasing uncertainty levels. With exciting new approaches for even the next generation of precision experiments being on the horizon. Such as the use of the radio isotope 229-Thorium, using a nuclear transition [126] opens up an exciting way to realise an ultra precise time keeper.

Appendix A

MOT Capture Velocity Simulations

Simulated Maximum capture velocities as described in section 2.2.1 for intensities from I=1.25 mW/cm^2 to I=40 mW/cm^2. In each step the intensity is doubled. The plots are showing the simulation for the 45° dispenser (a) and the foil dispenser (b).

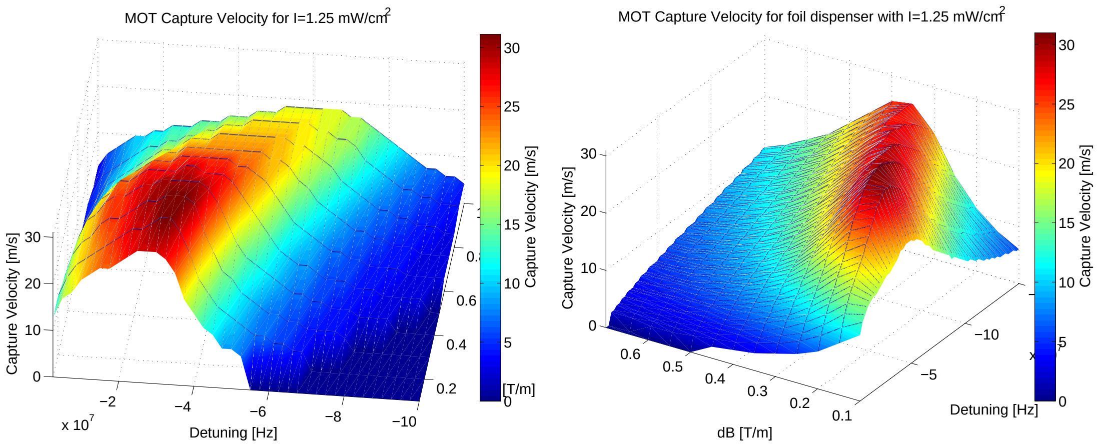

(a) 45° dispenser

(b) foil dispenser

Figure A.1: Simulated capture velocity for various detuning and magnetic gradient settings for I=1.25 mW/cm^2 and a beam width of 1 cm.

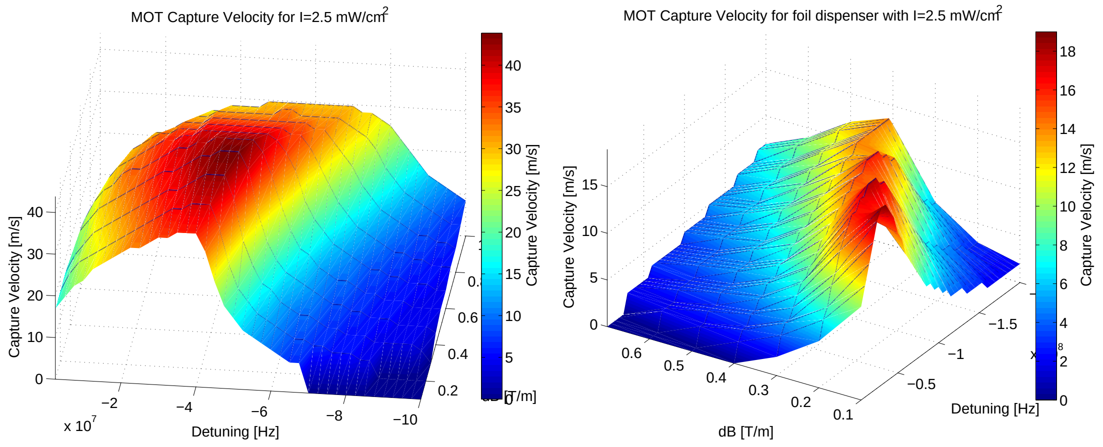

(a) 45° dispenser (b) foil dispenser

FIGURE A.2: Simulated capture velocity for various detuning and magnetic gradient settings for I=2.5 mW/cm^2 and a beam width of 1 cm.

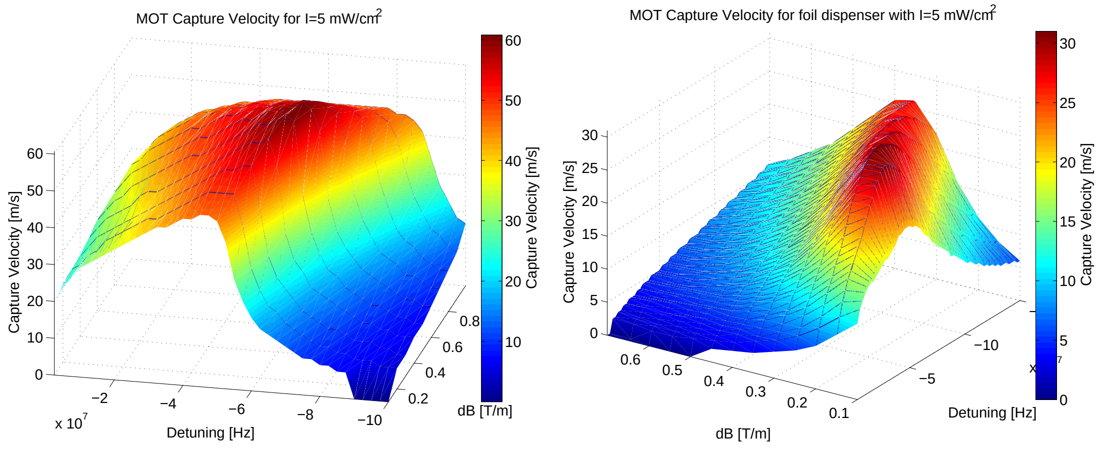

(a) 45° dispenser (b) foil dispenser

FIGURE A.3: Simulated capture velocity for various detuning and magnetic gradient settings for I=5 mW/cm^2 and a beam width of 1 cm.

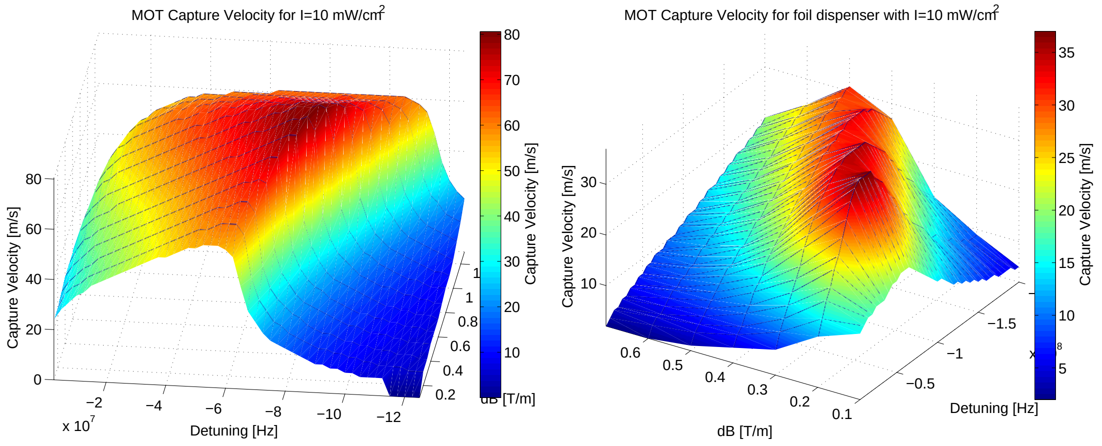

(a) 45° dispenser

(b) foil dispenser

Figure A.4: Simulated capture velocity for various detuning and magnetic gradient settings for I=10 mW/cm^2 and a beam width of 1 cm.

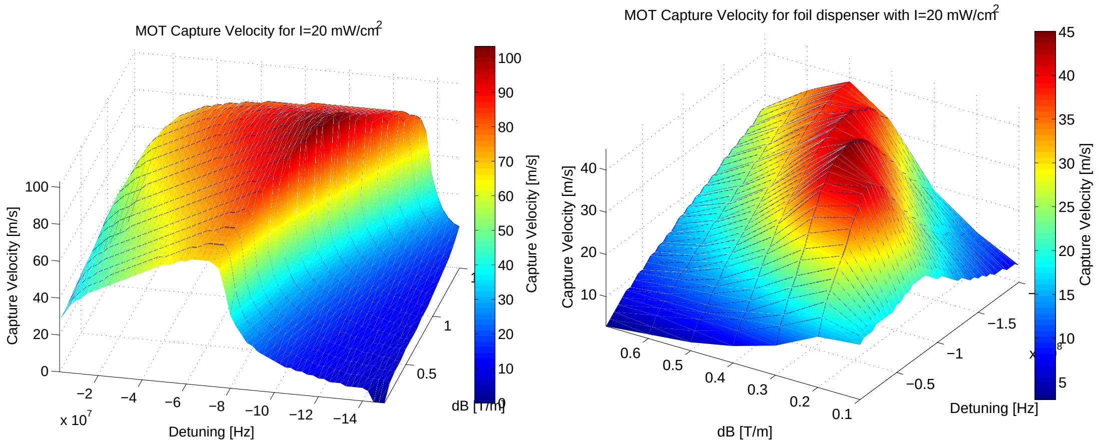

(a) 45° dispenser

(b) foil dispenser

Figure A.5: Simulated capture velocity for various detuning and magnetic gradient settings for I=20 mW/cm^2 and a beam width of 1 cm.

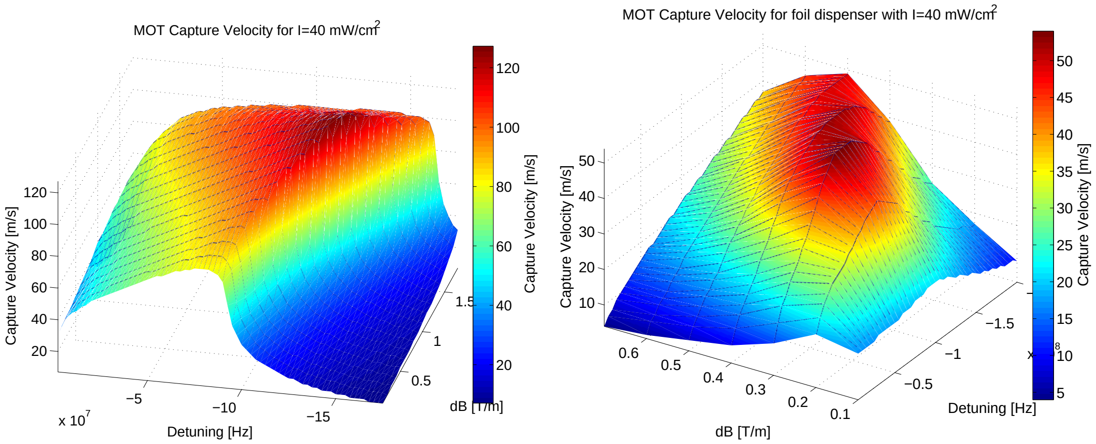

(a) 45° dispenser

(b) foil dispenser

FIGURE A.6: Simulated capture velocity for various detuning and magnetic gradient settings for I=40 mW/cm^2 and a beam width of 1 cm.

Appendix B

Theoretical Fibre Coupling Efficiencies

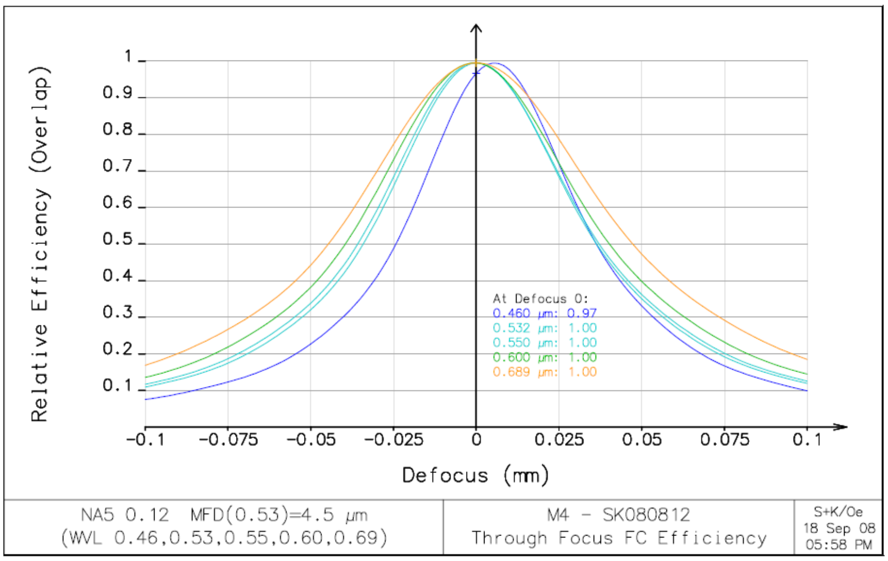

Figure B.1: Theoretical fibre coupling efficiency for Schäfter und Kirchhoff M4 achromatic lens for wavelengths from 461 nm to 689 nm. Defocus donates how much the coupling lens has to be moved to reach this point. The numbers for defocus 0 show the relative coupling efficiencies for different wavelengths. Plot provided by Schäfter und Kirchhoff.

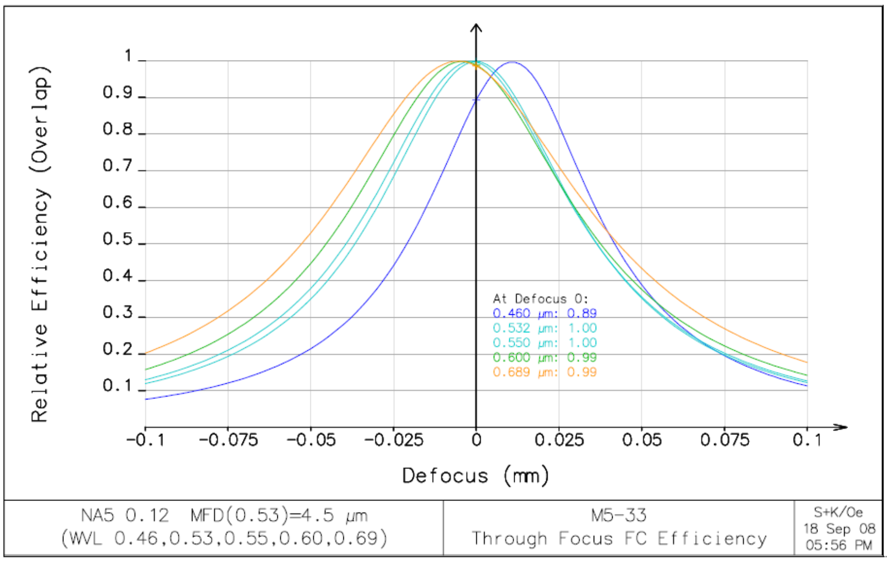

FIGURE B.2: Theoretical fibre coupling efficiency for Schäfter und Kirchhoff M4 achromatic lens for wavelengths from 461 nm to 689 nm. Defocus donates how much the coupling lens has to be moved to reach this point. The numbers for defocus 0 show the relative coupling efficiencies for different wavelengths. Plot provided by Schäfter und Kirchhoff.

Bibliography

[1] C. W. Chou, D. B. Hume, J. C. J. Koelemeij, D. J. Wineland, and T. Rosenband. Frequency Comparison of Two High-Accuracy Al^{+} Optical Clocks. *Physical Review Letters*, 104(7):070802, February 2010. ISSN 0031-9007. doi: 10.1103/PhysRevLett.104.070802. URL `http://link.aps.org/doi/10.1103/PhysRevLett.104.070802`.

[2] MM Boyd. *High precision spectroscopy of strontium in an optical lattice: Towards a new standard for frequency and time.* PhD thesis, University of Colorado at Boulder, 2007.

[3] R Wynands and S Weyers. Atomic fountain clocks. *Metrologia*, 42(3): S64–S79, June 2005. ISSN 0026-1394. doi: 10.1088/0026-1394/42/3/S08. URL `http://stacks.iop.org/0026-1394/42/i=3/a=S08?key=crossref.73cd3d68326b49d8f212d76e5079625d`.

[4] T Rosenband, D B Hume, P O Schmidt, C W Chou, a Brusch, L Lorini, W H Oskay, R E Drullinger, T M Fortier, J E Stalnaker, S a Diddams, W C Swann, N R Newbury, W M Itano, D J Wineland, and J C Bergquist. Frequency ratio of Al+ and Hg+ single-ion optical clocks; metrology at the 17th decimal place. *Science (New York, N.Y.)*, 319(5871):1808–12, March 2008. ISSN 1095-9203. doi: 10.1126/science.1154622. URL `http://www.ncbi.nlm.nih.gov/pubmed/18323415`.

[5] Thomas Middelmann, Stephan Falke, Christian Lisdat, and Uwe Sterr. High Accuracy Correction of Blackbody Radiation Shift in an Optical Lattice Clock. *Physical Review Letters*, 109(26):263004, December 2012. ISSN 0031-9007. doi: 10.1103/PhysRevLett.109.263004. URL `http://link.aps.org/doi/10.1103/PhysRevLett.109.263004`.

[6] H. Lyons. The Atomic Clock, An Atomic Standard of Frequency and Time. *N.B.S. Tech. News Bull.*, 33:17, 1949.

[7] L Essen and J.V.L. Parry. An atomic standard of frequency and time interval: a cæsium resonator. *Nature*, 176:280–285, 1955.

[8] BIPM. The International System of Units (SI). URL `www.bipm.org/utils/common/pdf/si_brochure_8_en.pdf`.

[9] Marco Schioppo. *Development of a Transportable Strontium Optical Clock*. PhD thesis, UNIVERSITÀ DEGLI STUDI DI FIRENZE, 2010.

[10] V Gerginov and N Nemitz. Recent improvements and current uncertainty budget of PTB fountain clock CSF2. *Proc. 24th European ...*, 2010. URL `http://ieeexplore.ieee.org/xpls/abs_all.jsp?arnumber=6533639`.

[11] J.L. Hall. Optical frequency measurement: 40 years of technology revolutions. *IEEE Journal of Selected Topics in Quantum Electronics*, 6(6):1136–1144, November 2000. ISSN 1077-260X. doi: 10.1109/2944.902162. URL `http://ieeexplore.ieee.org/lpdocs/epic03/wrapper.htm?arnumber=902162`.

[12] Carl Otto Weiss, Günter Kramer, Burghard Lipphardt and Harald Schnatz. *Frequency measurement and control : advanced techniques and future trends.*

[13] Long-Sheng Ma, Lennart Robertsson, Susanne Picard, Massimo Zucco, Zhiyi Bi, Shenghai Wu, and Robert S. Windeler. First international comparison of femtosecond laser combs at the International Bureau of Weights and Measures. *Optics Letters*, 29(6):641, 2004. ISSN 0146-9592. doi: 10.1364/OL.29.000641. URL `http://www.opticsinfobase.org/abstract.cfm?URI=OL-29-6-641`.

[14] Y Y Jiang, A D Ludlow, N D Lemke, R W Fox, J A Sherman, L.-S. Ma, and C W Oates. Making optical atomic clocks more stable with 1016-level laser stabilization. *Nature Photonics*, 5(3):158–161, January 2011. ISSN 1749-4885. doi: 10.1038/nphoton.2010.313. URL `http://www.nature.com/doifinder/10.1038/nphoton.2010.313`.

[15] M. G. Tarallo, N. Poli, M. Schioppo, D. Sutyrin, and G. M. Tino. A high-stability semiconductor laser system for a 88Sr-based optical lattice clock. *Applied Physics B*, 103(1):17–25, September 2010. ISSN 0946-2171. doi: 10.1007/s00340-010-4232-2. URL `http://link.springer.com/10.1007/s00340-010-4232-2`.

[16] Masao Takamoto, Tetsushi Takano, and Hidetoshi Katori. Frequency comparison of optical lattice clocks beyond the Dick limit. *Nature Photonics*, (April):1–5, 2011. doi: 10.1038/NPHOTON.2011.34. URL `http://dx.doi.org/10.1038/nphoton.2011.34http://www.nature.com/nphoton/journal/vaop/ncurrent/full/nphoton.2011.34.html`.

[17] Tetsuya Ido and Hidetoshi Katori. Recoil-Free Spectroscopy of Neutral Sr Atoms in the Lamb-Dicke Regime. *Physical Review Letters*, 91(5):053001, July 2003.

ISSN 0031-9007. doi: 10.1103/PhysRevLett.91.053001. URL `http://link.aps.org/doi/10.1103/PhysRevLett.91.053001`.

[18] Hidetoshi Katori. Optical lattice clocks and quantum metrology. *Nature Photonics*, 5(4):203–210, April 2011. ISSN 1749-4885. doi: 10.1038/nphoton.2011.45. URL `http://www.nature.com/doifinder/10.1038/nphoton.2011.45`.

[19] RH Dicke. The effect of collisions upon the Doppler width of spectral lines. *Physical Review*, 1953. URL `http://adsabs.harvard.edu/abs/1953PhRv...89..472D`.

[20] P. G. Westergaard, J. Lodewyck, L. Lorini, a. Lecallier, E. a. Burt, M. Zawada, J. Millo, and P. Lemonde. Lattice-Induced Frequency Shifts in Sr Optical Lattice Clocks at the 10^{-17} Level. *Physical Review Letters*, 106(21):210801, May 2011. ISSN 0031-9007. doi: 10.1103/PhysRevLett.106.210801. URL `http://link.aps.org/doi/10.1103/PhysRevLett.106.210801`.

[21] Matthew D Swallows, Michael Bishof, Yige Lin, Sebastian Blatt, Michael J Martin, Ana Maria Rey, and Jun Ye. Suppression of collisional shifts in a strongly interacting lattice clock. *Science (New York, N.Y.)*, 331(6020):1043–6, February 2011. ISSN 1095-9203. doi: 10.1126/science.1196442. URL `http://www.ncbi.nlm.nih.gov/pubmed/21292940`.

[22] K. Beloy. Lattice-induced nonadiabatic frequency shifts in optical lattice clocks. *Physical Review A*, 82(3):031402, September 2010. ISSN 1050-2947. doi: 10.1103/PhysRevA.82.031402. URL `http://link.aps.org/doi/10.1103/PhysRevA.82.031402`.

[23] Tomoya Akatsuka, Masao Takamoto, and Hidetoshi Katori. Three-dimensional optical lattice clock with bosonic ^{88}Sr atoms. *Physical Review A*, 81(2):023402, February 2010. ISSN 1050-2947. doi: 10.1103/PhysRevA.81.023402. URL `http://link.aps.org/doi/10.1103/PhysRevA.81.023402`.

[24] Ch. Lisdat, J. Winfred, T. Middelmann, F. Riehle, and U. Sterr. Collisional Losses, Decoherence, and Frequency Shifts in Optical Lattice Clocks with Bosons. *Physical Review Letters*, 103(9):090801, August 2009. ISSN 0031-9007. doi: 10.1103/PhysRevLett.103.090801. URL `http://link.aps.org/doi/10.1103/PhysRevLett.103.090801`.

[25] Hidetoshi Katori, Masao Takamoto, V. Palchikov, and V. Ovsiannikov. Ultrastable Optical Clock with Neutral Atoms in an Engineered Light Shift Trap. *Physical Review Letters*, 91(17):173005, October 2003. ISSN 0031-9007. doi: 10.1103/PhysRevLett.91.173005. URL `http://link.aps.org/doi/10.1103/PhysRevLett.91.173005`.

[26] Masao Takamoto and Hidetoshi Katori. Spectroscopy of the S01-P03 Clock Transition of Sr87 in an Optical Lattice. *Physical Review Letters*, 91(22):223001, November 2003. ISSN 0031-9007. doi: 10.1103/PhysRevLett.91.223001. URL `http://link.aps.org/doi/10.1103/PhysRevLett.91.223001`.

[27] Andrew Ludlow, Martin Boyd, Tanya Zelevinsky, Seth Foreman, Sebastian Blatt, Mark Notcutt, Tetsuya Ido, and Jun Ye. Systematic Study of the Sr87 Clock Transition in an Optical Lattice. *Physical Review Letters*, 96(3):033003, January 2006. ISSN 0031-9007. doi: 10.1103/PhysRevLett.96.033003. URL `http://link.aps.org/doi/10.1103/PhysRevLett.96.033003`.

[28] Rodolphe Le Targat, Xavier Baillard, Mathilde Fouché, Anders Brusch, Olivier Tcherbakoff, Giovanni Rovera, and Pierre Lemonde. Accurate Optical Lattice Clock with Sr87 Atoms. *Physical Review Letters*, 97(13):130801, September 2006. ISSN 0031-9007. doi: 10.1103/PhysRevLett.97.130801. URL `http://link.aps.org/doi/10.1103/PhysRevLett.97.130801`.

[29] Masao Takamoto, Feng-Lei Hong, Ryoichi Higashi, Yasuhisa Fujii, Michito Imae, and Hidetoshi Katori. Improved frequency measurement of a one-dimensional optical lattice clock with a spin-polarized fermionic $ˆ{87}$Sr isotope. August 2006. doi: 10.1143/JPSJ.75.104302. URL `http://arxiv.org/abs/physics/0608212`.

[30] CIPM. RECOMMENDED VALUES OF STANDARD FREQUENCIES FOR APPLICATIONS INCLUDING THE PRACTICAL REALIZATION OF THE METRE AND SECONDARY REPRESENTATIONS OF THE DEFINITION OF THE SECOND. URL `www.bipm.org/utils/common/pdf/mep/SRS_87Sr_429.pdf`.

[31] St Falke, H Schnatz, J S R Vellore Winfred, Th Middelmann, St Vogt, S Weyers, B Lipphardt, G Grosche, F Riehle, U Sterr, and Ch Lisdat. The 87 Sr optical frequency standard at PTB. *Metrologia*, 48(5): 399–407, October 2011. ISSN 0026-1394. doi: 10.1088/0026-1394/48/5/022. URL `http://stacks.iop.org/0026-1394/48/i=5/a=022?key=crossref.76cb3a00c4db880b6f81ae2b80b624f6`.

[32] X Baillard and M Fouché. An optical lattice clock with spin-polarized 87Sr atoms. *The European Physical ...*, 2008. URL `http://link.springer.com/article/10.1140/epjd/e2007-00330-3`.

[33] Gretchen K Campbell, Andrew D Ludlow, Sebastian Blatt, Jan W Thomsen, Michael J Martin, Marcio H G de Miranda, Tanya Zelevinsky, Martin M Boyd, Jun Ye, Scott A Diddams, Thomas P Heavner, Thomas E Parker, and Steven R

Jefferts. The absolute frequency of the 87 Sr optical clock transition. *Metrologia*, 45(5):539–548, October 2008. ISSN 0026-1394. doi: 10.1088/0026-1394/45/5/008. URL `http://stacks.iop.org/0026-1394/45/i=5/a=008?key=crossref.617fc9cd2168c86cf4fccd72eac5e09c`.

[34] FL Hong, M Musha, and M Takamoto. Measuring the frequency of a Sr optical lattice clock using a 120 km coherent optical transfer. *Optics . . .*, 2009. URL `http://www.opticsinfobase.org/abstract.cfm?URI=ol-34-5-692`.

[35] N. Lemke, A. Ludlow, Z. Barber, T. Fortier, S. Diddams, Y. Jiang, S. Jefferts, T. Heavner, T. Parker, and C. Oates. Spin-1/2 Optical Lattice Clock. *Physical Review Letters*, 103(6):063001, August 2009. ISSN 0031-9007. doi: 10.1103/PhysRevLett.103.063001. URL `http://link.aps.org/doi/10.1103/PhysRevLett.103.063001`.

[36] N. Poli, Z. Barber, N. Lemke, C. Oates, L. Ma, J. Stalnaker, T. Fortier, S. Diddams, L. Hollberg, J. Bergquist, A. Brusch, S. Jefferts, T. Heavner, and T. Parker. Frequency evaluation of the doubly forbidden ^{1}S_{0}^{3}P_{0} transition in bosonic ^{174}Yb. *Physical Review A*, 77(5):050501, May 2008. ISSN 1050-2947. doi: 10.1103/PhysRevA.77.050501. URL `http://link.aps.org/doi/10.1103/PhysRevA.77.050501`.

[37] Tomoya Akatsuka, Masao Takamoto, and Hidetoshi Katori. Optical lattice clocks with non-interacting bosons and fermions. *Nature Physics*, 4(12):954–959, October 2008. ISSN 1745-2473. doi: 10.1038/nphys1108. URL `http://www.nature.com/doifinder/10.1038/nphys1108`.

[38] G Wilpers, C W Oates, S A Diddams, A Bartels, T M Fortier, W H Oskay, J C Bergquist, S R Jefferts, T P Heavner, T E Parker, and L Hollberg. Absolute frequency measurement of the neutral 40 Ca optical frequency standard at 657 nm based on microkelvin atoms. *Metrologia*, 44 (2):146–151, April 2007. ISSN 0026-1394. doi: 10.1088/0026-1394/44/2/005. URL `http://stacks.iop.org/0026-1394/44/i=2/a=005?key=crossref.958d12d80b9f000b205ae7a22828808c`.

[39] Chris Alber, Randolph Ware, Christian Rocken, and Fredrick Solheim. GPS surveying with 1 mm precision using corrections for atmospheric slant path delay. *Geophysical Research Letters*, 24(15):1859–1862, August 1997. ISSN 00948276. doi: 10.1029/97GL01877. URL `http://doi.wiley.com/10.1029/97GL01877`.

[40] A Ludlow. *The Strontium Optical Lattice Clock: Optical Spectroscopy with Sub-Hertz Accuracy.* PhD thesis, JILA, 2009. URL `http://meetings.aps.org/link/BAPS.2009.DAMOP.C1.2`.

[41] K Predehl and R Holzwarth. Ultra precise frequency dissemination across Germany-Towards a 900 km optical fiber link from PTB to MPQ. *Lasers and Electro- . . .* , 2009. URL `http://ieeexplore.ieee.org/xpls/abs_all.jsp?arnumber=5225582`.

[42] Byron D Tapley, Srinivas Bettadpur, John C Ries, Paul F Thompson, and Michael M Watkins. GRACE measurements of mass variability in the Earth system. *Science (New York, N.Y.)*, 305(5683):503–5, July 2004. ISSN 1095-9203. doi: 10.1126/science.1099192. URL `http://www.ncbi.nlm.nih.gov/pubmed/15273390`.

[43] Judah Levine and O Ibarra-Manzano. Invited review article: The statistical modeling of atomic clocks and the design of time scales. *The Review of scientific instruments*, 83(2):021101, February 2012. ISSN 1089-7623. doi: 10.1063/1.3681448. URL `http://www.ncbi.nlm.nih.gov/pubmed/22380071`.

[44] K. Alder. The measure of all things. *Free Press, New York*, 2002.

[45] Daniel Kleppner. Time too good to be true. *Physics Today*, (March):10–11, 2006. URL `http://www.leapsecond.com/great2005/vol59no3p10_11.pdf`.

[46] S Schiller, A Görlitz, and A Nevsky. Optical clocks in space. *Nuclear Physics B- . . .* , 2007. URL `http://www.sciencedirect.com/science/article/pii/S0920563206010413`.

[47] GM Tino. Cold atoms physics in space. *Nuclear Physics B-Proceedings Supplements*, 2002. URL `http://www.sciencedirect.com/science/article/pii/S0920563202018546`.

[48] L Cacciapuoti and N Dimarcq. Atomic clock ensemble in space: scientific objectives and mission status. *Nuclear Physics B- . . .* , 2007. URL `http://www.sciencedirect.com/science/article/pii/S0920563206010425`.

[49] GM Tino, L Cacciapuoti, and K Bongs. Atom interferometers and optical atomic clocks: New quantum sensors for fundamental physics experiments in space. *Nuclear Physics B- . . .* , 2007. URL `http://www.sciencedirect.com/science/article/pii/S0920563206010152`.

[50] R Beard, W Golding, and J White. Design factors for atomic clocks for space. *Proceedings of the 2002 IEEE International Frequency Control Symposium and PDA Exhibition Cat No02CH37234*, (21641), 2002.

[51] Patrick Gill, Helen Margolis, Anne Curtis, and Hugh Klein. Optical Atomic Clocks for Space. *. . . No. 21641/08/NL/PA, pp . . .* , 2008. URL `http://www.npl.co.uk/upload/pdf/atomic_clocks_space.pdf`.

[52] SG Turyshev, UE Israelsson, and M Shao. Space-based research in fundamental physics and quantum technologies. *... of Modern Physics D*, 2007. URL `http://www.worldscientific.com/doi/pdf/10.1142/S0218271807011760`.

[53] P Wolf, C Salomon, and S Reynaud. Space clocks to test relativiy: ACES and SAGAS. *Proceedings of the ...*, 2009. URL `http://journals.cambridge.org/production/action/cjoGetFulltext?fulltextid=6911536`.

[54] NK Pavlis and MA Weiss. The relativistic redshift with 3 10â 17 uncertainty at NIST, Boulder, Colorado, USA. *Metrologia*, 40:66–73, 2003. URL `http://iopscience.iop.org/0026-1394/40/2/311`.

[55] M Kufner, A Seidel, M P Hess, J Kehrer, and Timetech Gmbh. ACES Microwave Link (MWL) as an Universal Tool for Time Transfer and Ranging from Low Earth Orbit to Deep Space Applications ACES Overview Microwave Link Requirements Link Configuration Flight segment test results (Engineering Model) Phase s. In *Munich*, pages 1–28, 2008.

[56] L Cacciapuoti and C Salomon. Atomic clock ensemble in space. *Journal of Physics: Conference Series*, 327:012049, December 2011. ISSN 1742-6596. doi: 10.1088/1742-6596/327/1/012049. URL `http://stacks.iop.org/1742-6596/327/i=1/a=012049?key=crossref.01fc2a634cfc9439865524ea74c7731a`.

[57] Austin University. Gravity Recovery and Climate Experiment. URL `http://www.csr.utexas.edu/grace/`.

[58] Bundesamt fuer Kartographie. Coordinate Reference Systems (CRS). URL `http://crs.bkg.bund.de`.

[59] Ruxandra Bondarescu, Mihai Bondarescu, György Hetényi, Lapo Boschi, Philippe Jetzer, and Jayashree Balakrishna. Geophysical applicability of atomic clocks: direct continental geoid mapping. *arXiv preprint: 1209.2889*, September 2012. doi: 10.1111/j.1365-246X.2012.05636.x. URL `http://arxiv.org/abs/1209.2889`.

[60] B Linet and P Teyssandier. Time transfer and frequency shift to the order 1/c^{4} in the field of an axisymmetric rotating body. *Physical Review D*, 2002. URL `http://prd.aps.org/abstract/PRD/v66/i2/e024045`.

[61] C W Chou, D B Hume, T Rosenband, and D J Wineland. Optical clocks and relativity. *Science (New York, N.Y.)*, 329(5999):1630–3, September 2010. ISSN 1095-9203. doi: 10.1126/science.1192720. URL `http://www.ncbi.nlm.nih.gov/pubmed/20929843`.

[62] HJ Metcalf and P Van der Straten. *Laser cooling and trapping.* 1999. URL http://books.google.com/books?hl=en&lr=&id=i-40VaXqrj0C&oi=fnd&pg=PR7&dq=Laser+cooling+and+trapping&ots=NOL-_D3G5L&sig=qcmmtasheRH102AGlS6FT-fyf3I.

[63] MH Anderson, JR Ensher, and MR Matthews. Observation of Bose-Einstein condensation in a dilute atomic vapor. *science*, 1995. URL http://www.sciencemag.org/content/269/5221/198.short.

[64] S Giorgini, LP Pitaevskii, and S Stringari. Theory of ultracold Fermi gases. *arXiv preprint arXiv:0706.3360*, 2007. URL http://arxiv.org/abs/0706.3360.

[65] Jason Socrates Bardi. Landmarks: Laser Cooling of Atoms. *Phys. Rev. Focus*, 21: 11, April 2008. doi: 10.1103/PhysRevFocus.21.11. URL http://link.aps.org/doi/10.1103/PhysRevFocus.21.11.

[66] B. DeMarco. Onset of Fermi Degeneracy in a Trapped Atomic Gas. *Science*, 285(5434):1703–1706, September 1999. ISSN 00368075. doi: 10.1126/science.285.5434.1703. URL http://www.sciencemag.org/cgi/doi/10.1126/science.285.5434.1703.

[67] JE Sansonetti. Handbook of basic atomic spectroscopic data. *... Chemical Reference Data*, 2005. doi: 10.106311.1800011. URL http://www.chembbs.com.cn/bbs/File/UserFiles/UpLoad/20090824115102bn.pdf.

[68] Jan Friebe, André Pape, Matthias Riedmann, Karsten Moldenhauer, Tanja Mehlstäubler, Nils Rehbein, Christian Lisdat, Ernst Rasel, Wolfgang Ertmer, Harald Schnatz, Burghard Lipphardt, and Gesine Grosche. Absolute frequency measurement of the magnesium intercombination transition ˆ{1}S_{0}ˆ{3}P_{1}. *Physical Review A*, 78(3):033830, September 2008. ISSN 1050-2947. doi: 10.1103/PhysRevA.78.033830. URL http://link.aps.org/doi/10.1103/PhysRevA.78.033830.

[69] A D Ludlow, T Zelevinsky, G K Campbell, S Blatt, M M Boyd, M H G de Miranda, M J Martin, J W Thomsen, S M Foreman, Jun Ye, T M Fortier, J E Stalnaker, S A Diddams, Y Le Coq, Z W Barber, N Poli, N D Lemke, K M Beck, and C W Oates. Sr lattice clock at 1 x 10(-16) fractional uncertainty by remote optical evaluation with a Ca clock. *Science (New York, N.Y.)*, 319(5871):1805–8, March 2008. ISSN 1095-9203. doi: 10.1126/science.1153341. URL http://www.ncbi.nlm.nih.gov/pubmed/18276849.

[70] S Schiller, GM Tino, and U Sterr. The Space Optical Clock project: status and perspectives. *38th COSPAR ...*, 2010. URL `http://adsabs.harvard.edu/abs/2010cosp...38.3801S`.

[71] Steffen Ruhmann, Matthias Riedmann, Temmo Wubbena, Andre Kulosa, Andre Pape, Dominika Fim, Klaus Zipfel, Birte Lampmann, Jan Friebe, Hrishikesh Kelkar, Wolfgang Ertmer, and Ernst M. Rasel. Towards a magnesium optical lattice clock. In *2011 Conference on Lasers and Electro-Optics Europe and 12th European Quantum Electronics Conference (CLEO EUROPE/EQEC)*, pages 1–1. IEEE, May 2011. ISBN 978-1-4577-0533-5. doi: 10.1109/CLEOE.2011.5943301. URL `http://ieeexplore.ieee.org/lpdocs/epic03/wrapper.htm?arnumber=5943301`.

[72] Takashi Mukaiyama, Hidetoshi Katori, Tetsuya Ido, Ying Li, and Makoto Kuwata-Gonokami. Recoil-Limited Laser Cooling of Sr87 Atoms near the Fermi Temperature. *Physical Review Letters*, 90(11):113002, March 2003. ISSN 0031-9007. doi: 10.1103/PhysRevLett.90.113002. URL `http://link.aps.org/doi/10.1103/PhysRevLett.90.113002`.

[73] GK Woodgate. Elementary atomic structure. 1970. URL `http://www.osti.gov/energycitations/product.biblio.jsp?osti_id=4055778`.

[74] R.L. Kurucz and B. Bell. Atomic line data. *Atomic Line Data (RL Kurucz and B. Bell) ...*, pages Kurucz CD–ROM No. 23. Cambridge, Mass.: Smithsonia, 1995. URL `http://adsabs.harvard.edu/abs/1995KurCD..23.....K`.

[75] P G Mickelson, Y N Martinez de Escobar, P Anzel, B J DeSalvo, S B Nagel, A J Traverso, M Yan, and T C Killian. Repumping and spectroscopy of laser-cooled Sr atoms using the (5s5p) 3 P 2 (5s4d) 3 D 2 transition. *Journal of Physics B: Atomic, Molecular and Optical Physics*, 42 (23):235001, December 2009. ISSN 0953-4075. doi: 10.1088/0953-4075/42/23/235001. URL `http://stacks.iop.org/0953-4075/42/i=23/a=235001?key=crossref.a02d863a5f28acf3834f8be9018d8045`.

[76] AV Taichenachev, VI Yudin, and CW Oates. Magnetic field-induced spectroscopy of forbidden optical transitions with application to lattice-based optical atomic clocks. *Physical review ...*, 2006. URL `http://prl.aps.org/abstract/PRL/v96/i8/e083001`.

[77] David S. Weiss, Erling Riis, Yaakov Shevy, P. Jeffrey Ungar, and Steven Chu. Optical molasses and multilevel atoms: experiment. *Journal of the Optical Society of America B*, 6(11):2072, November 1989. ISSN 0740-3224. doi:

10.1364/JOSAB.6.002072. URL `http://www.opticsinfobase.org/abstract.cfm?URI=josab-6-11-2072`.

[78] J Dalibard and C Cohen-Tannoudji. Laser cooling below the Doppler limit by polarization gradients: simple theoretical models. *J. Opt. Soc. Am. B*, 1989. URL `http://www.kip.uni-heidelberg.de/matterwaveoptics/teaching/archive/ws05-06/view.pdf`.

[79] Xinye Xu, Thomas Loftus, Josh Dunn, Chris Greene, John Hall, Alan Gallagher, and Jun Ye. Single-Stage Sub-Doppler Cooling of Alkaline Earth Atoms. *Physical Review Letters*, 90(19):193002, May 2003. ISSN 0031-9007. doi: 10.1103/PhysRevLett.90.193002. URL `http://link.aps.org/doi/10.1103/PhysRevLett.90.193002`.

[80] Thomas Loftus, Tetsuya Ido, Martin Boyd, Andrew Ludlow, and Jun Ye. Narrow line cooling and momentum-space crystals. *Physical Review A*, 70(6):063413, December 2004. ISSN 1050-2947. doi: 10.1103/PhysRevA.70.063413. URL `http://link.aps.org/doi/10.1103/PhysRevA.70.063413`.

[81] N. Poli, R. Drullinger, G. Ferrari, J. Léonard, F. Sorrentino, and G. Tino. Cooling and trapping of ultracold strontium isotopic mixtures. *Physical Review A*, 71(6):061403, June 2005. ISSN 1050-2947. doi: 10.1103/PhysRevA.71.061403. URL `http://link.aps.org/doi/10.1103/PhysRevA.71.061403`.

[82] Thomas Legero, Joseph Sundar Raaj Vellore Winfred, Fritz Riehle, and Uwe Sterr. Ultracold 88Sr atoms for an optical lattice clock. In *2007 IEEE International Frequency Control Symposium Joint with the 21st European Frequency and Time Forum*, pages 119–122. IEEE, May 2007. ISBN 978-1-4244-0646-3. doi: 10.1109/FREQ.2007.4319045. URL `http://ieeexplore.ieee.org/lpdocs/epic03/wrapper.htm?arnumber=4319045`.

[83] M. Chalony, a. Kastberg, B. Klappauf, and D. Wilkowski. Doppler Cooling to the Quantum Limit. *Physical Review Letters*, 107(24):243002, December 2011. ISSN 0031-9007. doi: 10.1103/PhysRevLett.107.243002. URL `http://link.aps.org/doi/10.1103/PhysRevLett.107.243002`.

[84] Qiang Wang, Bai-Ke Lin, Yang Zhao, Ye Li, Shao-Kai Wang, Min-Ming Wang, Er-Jun Zang, Tian-Chu Li, and Zhan-Jun Fang. Magneto-Optical Trapping of 88 Sr atoms with 689 nm Laser. *Chinese Physics Letters*, 28(3):033201, March 2011. ISSN 0256-307X. doi: 10.1088/0256-307X/28/3/033201. URL `http://stacks.iop.org/0256-307X/28/i=3/a=033201?key=crossref.929868329213ef7f86427dc768751b20`.

[85] K.R. Vogel, T.P. Dinneen, a. Gallagher, and J.L. Hall. Narrow-line Doppler cooling of strontium to the recoil limit. *IEEE Transactions on Instrumentation and Measurement*, 48(2):618–621, April 1999. ISSN 00189456. doi: 10.1109/19.769671. URL `http://ieeexplore.ieee.org/lpdocs/epic03/wrapper.htm?arnumber=769671`.

[86] J. Schoser, a. Batär, R. Löw, V. Schweikhard, a. Grabowski, Yu. Ovchinnikov, and T. Pfau. Intense source of cold Rb atoms from a pure two-dimensional magneto-optical trap. *Physical Review A*, 66(2):023410, August 2002. ISSN 1050-2947. doi: 10.1103/PhysRevA.66.023410. URL `http://link.aps.org/doi/10.1103/PhysRevA.66.023410`.

[87] I Courtillot, a Quessada, R P Kovacich, J J Zondy, a Landragin, a Clairon, and P Lemonde. Efficient cooling and trapping of strontium atoms. *Optics letters*, 28 (6):468–70, March 2003. ISSN 0146-9592. URL `http://www.ncbi.nlm.nih.gov/pubmed/12659282`.

[88] a D Ludlow, T Zelevinsky, G K Campbell, S Blatt, M M Boyd, M H G de Miranda, M J Martin, J W Thomsen, S M Foreman, Jun Ye, T M Fortier, J E Stalnaker, S a Diddams, Y Le Coq, Z W Barber, N Poli, N D Lemke, K M Beck, and C W Oates. Sr lattice clock at 1 x 10(-16) fractional uncertainty by remote optical evaluation with a Ca clock. *Science (New York, N.Y.)*, 319(5871):1805–8, March 2008. ISSN 1095-9203. doi: 10.1126/science.1153341. URL `http://www.ncbi.nlm.nih.gov/pubmed/18276849`.

[89] BO Kock. *Design eines Lasersystems und einer Vakuumapparatur für eine 2D-/3D. MOT mit Strontium.* PhD thesis, Universitaet Hamburg, 2009. URL `http://scholar.google.com/scholar?hl=en&btnG=Search&q=intitle:Design+eines+Lasersystems+und+einer+Vakuumapparatur+f\unhbox\voidb@x\bgroup\let\unhbox\voidb@x\setbox\@tempboxa\hbox{u\global\mathchardef\accent@spacefactor\spacefactor}\accent127u\egroup\spacefactor\accent@spacefactorr+eine+2D-/+3D-MOT+mit+Strontium#0`.

[90] K. B. MacAdam. A narrow-band tunable diode laser system with grating feedback, and a saturated absorption spectrometer for Cs and Rb. *American Journal of Physics*, 60(12):1098, 1992. ISSN 00029505. doi: 10.1119/1.16955. URL `http://link.aip.org/link/?AJP/60/1098/1&Agg=doi`.

[91] T. Könemann, W. Brinkmann, E. Göklü, C. Lämmerzahl, H. Dittus, T. van Zoest, E.M. Rasel, W. Ertmer, W. Lewoczko-Adamczyk, M. Schiemangk, A. Peters, A. Vogel, G. Johannsen, S. Wildfang, K. Bongs, K. Sengstock, E. Kajari, G. Nandi, R. Walser, and W.P. Schleich. A freely falling magneto-optical

trap drop tower experiment. *Applied Physics B*, 89:431, 2007. URL `http://link.springer.com/article/10.1007/s00340-007-2863-8`.

[92] H Loh, YJ Lin, I Teper, and M Cetina. Influence of grating parameters on the linewidths of external-cavity diode lasers. *Applied ...*, 2006. URL `http://www.opticsinfobase.org/abstract.cfm?id=119722`.

[93] Xinye Xu, Thomas H. Loftus, John L. Hall, Alan Gallagher, and Jun Ye. Cooling and trapping of atomic strontium. *Journal of the Optical Society of America B*, 20(5):968, 2003. ISSN 0740-3224. doi: 10.1364/JOSAB.20.000968. URL `http://www.opticsinfobase.org/abstract.cfm?URI=JOSAB-20-5-968`.

[94] S. Nagel, C. Simien, S. Laha, P. Gupta, V. Ashoka, and T. Killian. Magnetic trapping of metastable ^{3}P_{2} atomic strontium. *Physical Review A*, 67(1): 011401, January 2003. ISSN 1050-2947. doi: 10.1103/PhysRevA.67.011401. URL `http://link.aps.org/doi/10.1103/PhysRevA.67.011401`.

[95] RW Boyd. *Nonlinear optics.* 1992. ISBN 978-0-12-369470-6. URL `http://www.osti.gov/energycitations/product.biblio.jsp?osti_id=5321594`.

[96] B. Boulanger and J. Zyss. Nonlinear optical properties. *International Tables for Crystallography*, pages 178–219, 2006.

[97] Rodolphe Le Targat, Jean-Jacques Zondy, and Pierre Lemonde. 75%-efficiency blue generation from an intracavity PPKTP frequency doubler. *Optics Communications*, 247(4-6):471–481, August 2004. doi: 10.1016/j.optcom.2004.11.081. URL `http://arxiv.org/abs/physics/0408031`.

[98] G. D. Boyd. Parametric Interaction of Focused Gaussian Light Beams. *Journal of Applied Physics*, 39(8):3597, 1968. ISSN 00218979. doi: 10.1063/1.1656831. URL `http://link.aip.org/link/?JAP/39/3597/1&Agg=doi`.

[99] Firuz Torabi-Goudarzi and Erling Riis. Efficient cw high-power frequency doubling in periodically poled KTP. *Optics Communications*, 227(4-6):389–403, November 2003. ISSN 00304018. doi: 10.1016/j.optcom.2003.09.056. URL `http://linkinghub.elsevier.com/retrieve/pii/S0030401803020133`.

[100] A. Douillet, J.-J. Zondy, A. Yelisseyev, S. Lobanov, and L. Isaenko. Stability and frequency tuning of thermally loaded continuous-wave AgGaS_2 optical parametric oscillators. *Journal of the Optical Society of America B*, 16(9): 1481, September 1999. ISSN 0740-3224. doi: 10.1364/JOSAB.16.001481. URL `http://www.opticsinfobase.org/abstract.cfm?URI=josab-16-9-1481`.

[101] W.J. Kozlovsky, C.D. Nabors, and R.L. Byer. Efficient second harmonic generation of a diode-laser-pumped CW Nd:YAG laser using monolithic MgO:LiNbO/sub 3/ external resonant cavities. *IEEE Journal of Quantum Electronics*, 24(6):913–919, June 1988. ISSN 0018-9197. doi: 10.1109/3.211. URL `http://ieeexplore.ieee.org/lpdocs/epic03/wrapper.htm?arnumber=211`.

[102] J.-J. Zondy, D. Touahri, and O. Acef. Absolute value of the d_36 nonlinear coefficient of AgGaS_2: prospect for a low-threshold doubly resonant oscillator-based 3:1 frequency divider. *Journal of the Optical Society of America B*, 14 (10):2481, October 1997. ISSN 0740-3224. doi: 10.1364/JOSAB.14.002481. URL `http://www.opticsinfobase.org/abstract.cfm?URI=josab-14-10-2481`.

[103] Eric Black. Notes on pound-drever-hall technique. *LIGO Technical notes*, (617), 1998. URL `http://www.citeulike.org/group/1530/article/2002053`.

[104] M. Bode, I. Freitag, A. Tünnermann, and H. Welling. Frequency-tunable 500-mW continuous-wave all-solid-state single-frequency source in the blue spectral region. *Optics Letters*, 22(16):1220, August 1997. ISSN 0146-9592. doi: 10.1364/OL.22.001220. URL `http://www.opticsinfobase.org/abstract.cfm?URI=ol-22-16-1220`.

[105] Y Li, Y Zhao, Y Peng, and T Yang. More than 200 mW blue light source from an integrative ring cavity. *...Digest, 2008. CPEM ...*, 2008. URL `http://ieeexplore.ieee.org/xpls/abs_all.jsp?arnumber=4574717`.

[106] Bruce G Klappauf, Yannick Bidel, David Wilkowski, Thierry Chanelière, and Robin Kaiser. Detailed study of an efficient blue laser source by second-harmonic generation in a semimonolithic cavity for the cooling of strontium atoms. *Applied optics*, 43(12):2510–27, April 2004. ISSN 0003-6935. URL `http://www.ncbi.nlm.nih.gov/pubmed/15119621`.

[107] G. C. Bjorklund, M. D. Levenson, W. Lenth, and C. Ortiz. Frequency modulation (FM) spectroscopy. *Applied Physics B Photophysics and Laser Chemistry*, 32 (3):145–152, November 1983. ISSN 0721-7269. doi: 10.1007/BF00688820. URL `http://link.springer.com/10.1007/BF00688820`.

[108] Wolfgang Demtröder. *Laserspektroskopie*. Springer, 2007. ISBN ISBN 978-3-540-33792-8.

[109] E M Bridge, J Millen, C S Adams, and M P a Jones. A vapor cell based on dispensers for laser spectroscopy. *The Review of scientific instruments*, 80(1): 013101, January 2009. ISSN 1089-7623. doi: 10.1063/1.3036980. URL `http://www.ncbi.nlm.nih.gov/pubmed/19191423`.

[110] K Odaka, Y Ishikawa, and M Furuse. Effect of baking temperature and air exposure on the outgassing rate of type 316L stainless steel. *Journal of Vacuum Science & . . .*, 1987. URL `http://ieeexplore.ieee.org/xpls/abs_all.jsp?arnumber=4933983`.

[111] Kenji Odaka and Shinjiro Ueda. Outgassing reduction of type 304 stainless steel by surface oxidation in air. *Journal of Vacuum Science & Technology A . . .*, 13(September 1994):520–523, 1995. URL `http://ieeexplore.ieee.org/xpls/abs_all.jsp?arnumber=4929916`.

[112] M Bober, J Zachorowski, and W Gawlik. Designing Zeeman slower for strontium atoms-towards optical atomic clock. *arXiv preprint arXiv:1006.1554*, XL(3), 2010. URL `http://arxiv.org/abs/1006.1554`.

[113] Pfeiffer Vacuum. Working with turbo pumps - Introduction to high and ultra high vacuum production. URL `http://www.pfeiffer-vacuum.com/know-how/container.action`.

[114] K J Weatherill, J D Pritchard, C S Adams, P F Griffin, U Dammalapati, and E Riis. A versatile and reliably re-usable ultrahigh vacuum viewport. *arXiv preprint:0812.1019*, December 2008. doi: 10.1063/1.3075547. URL `http://arxiv.org/abs/0812.1019`.

[115] S. G. Cox, P. F. Griffin, C. S. Adams, D. DeMille, and E. Riis. Reusable ultrahigh vacuum viewport bakeable to 240C. *Review of Scientific Instruments*, 74(6):3185, 2003. ISSN 00346748. doi: 10.1063/1.1574604. URL `http://link.aip.org/link/RSINAK/v74/i6/p3185/s1&Agg=doi`.

[116] K. Dieckmann, R. Spreeuw, M. Weidemüller, and J. Walraven. Two-dimensional magneto-optical trap as a source of slow atoms. *Physical Review A*, 58(5):3891–3895, November 1998. ISSN 1050-2947. doi: 10.1103/PhysRevA.58.3891. URL `http://link.aps.org/doi/10.1103/PhysRevA.58.3891`.

[117] T. Tiecke, S. Gensemer, a. Ludewig, and J. Walraven. High-flux two-dimensional magneto-optical-trap source for cold lithium atoms. *Physical Review A*, 80(1): 013409, July 2009. ISSN 1050-2947. doi: 10.1103/PhysRevA.80.013409. URL `http://link.aps.org/doi/10.1103/PhysRevA.80.013409`.

[118] M Baumert. *Dipole traps and optical lattices for quantum simulations.* PhD thesis, University of Birmingham, 2013. URL `http://etheses.bham.ac.uk/3679/`.

[119] F Sorrentino, G Ferrari, and N Poli. Laser cooling and trapping of atomic Strontium for ultracold atoms physics, high-precision spectroscopy and quantum sensors. *Modern Physics ...*, 2006. URL `http://www.worldscientific.com/doi/pdf/10.1142/S0217984906011682`.

[120] S Wang, Q Wang, Y Lin, and M Wang. Cooling and Trapping 88Sr Atoms with 461 nm Laser. *Chinese Physics ...*, 26(9):3–5, 2009. URL `http://cpl.iphy.ac.cn/EN/article/downloadArticleFile.do?attachType=PDF&id=41672`.

[121] T.D. Dinnen, K.R. Vogel, E. Arimondo, J.L. Hall, and A. Gallagher. No Title. *Physical Review A*, 59:1216, 1999.

[122] Steven Johnson. *Narrow Linewidth Lasers for use with Neutral Strontium as a Frequency Standard by.* PhD thesis, University of Birmingham, 2012.

[123] Simon Stellmer, MK Tey, Bo Huang, Rudolf Grimm, and Florian Schreck. Bose-Einstein condensation of strontium. *Physical review letters*, pages 1–4, 2009. URL `http://link.aps.org/doi/10.1103/PhysRevLett.103.200401`.

[124] CP Koch. Perspectives for coherent optical formation of strontium molecules in their electronic ground state. *Physical Review A*, 2008. URL `http://pra.aps.org/abstract/PRA/v78/i6/e063411`.

[125] D. Maxwell, D. J. Szwer, D. P. Barato, H. Busche, J. D. Pritchard, A. Gauguet, K. J. Weatherill, M. P. A. Jones, and C. S. Adams. Storage and control of optical photons using Rydberg polaritons. page 7, July 2012. URL `http://arxiv.org/abs/1207.6007`.

[126] G A Kazakov, A N Litvinov, V I Romanenko, L P Yatsenko, A V Romanenko, M Schreitl, G Winkler, and T Schumm. Performance of a 229 Thorium solid-state nuclear clock. *New Journal of Physics*, 14 (8):083019, August 2012. ISSN 1367-2630. doi: 10.1088/1367-2630/14/8/083019. URL `http://stacks.iop.org/1367-2630/14/i=8/a=083019?key=crossref.bb4739ae1f3b672c6289490e3f371a0d`.